AVC-VTN-18-G01

The Effect of Topographic Shape and Shot Depth on Seismic Waveform Generation at Local and Regional Distances

Jeffry L. Stevens
Michael O'Brien

Leidos
10260 Campus Point Drive
San Diego, CA 92121

Final Report under DOS SAQM-MA-17M1724

11 September 2018

APPROVED FOR PUBLIC RELEASE; DISTRIBUTION IS UNLIMITED.

The views and conclusions in this report are those of the authors and should not be interpreted as representing the official policies, either expressed or implied, of the Department of State or the whole U.S. Government. Additional requests for the report can be directed to the authors, the United States Department of States (Attn: DOS/AVC/OAS (Rongsong Jih), Washington DC, 20520), or the Defense Technical Information Center.

REPORT DOCUMENTATION PAGE

Form Approved
OMB No. 0704-0188

Public reporting burden for this collection of information is estimated to average 1 hour per response, including the time for reviewing instructions, searching existing data sources, gathering and maintaining the data needed, and completing and reviewing this collection of information. Send comments regarding this burden estimate or any other aspect of this collection of information, including suggestions for reducing this burden to Department of Defense, Washington Headquarters Services, Directorate for Information Operations and Reports (0704-0188), 1215 Jefferson Davis Highway, Suite 1204, Arlington, VA 22202-4302. Respondents should be aware that notwithstanding any other provision of law, no person shall be subject to any penalty for failing to comply with a collection of information if it does not display a currently valid OMB control number. **PLEASE DO NOT RETURN YOUR FORM TO THE ABOVE ADDRESS.**

1. REPORT DATE *(DD-MM-YYYY)*
11 September 2018

2. REPORT TYPE
Final Report

3. DATES COVERED *(From - To)*
12 September 2017 to 11 September 2018

4. TITLE AND SUBTITLE
The Effect of Topographic Shape and Shot Depth on Seismic Waveform Generation at Local and Regional Distances

5a. CONTRACT NUMBER
SAQMMA17M1724

5b. GRANT NUMBER

5c. PROGRAM ELEMENT NUMBER

6. AUTHOR(S)
Jeffry L. Stevens, Michael O’Brien

5d. PROJECT NUMBER

5e. TASK NUMBER

5f. WORK UNIT NUMBER

7. PERFORMING ORGANIZATION NAME(S) AND ADDRESS(ES)
Leidos
10260 Campus Point Drive
San Diego, CA 92121

8. PERFORMING ORGANIZATION REPORT NUMBER

9. SPONSORING / MONITORING AGENCY NAME(S) AND ADDRESS(ES)
U.S. Department of State
Bureau of Arms Control, Verification, & Compliance
Office of Assistance Secretary (DOS/AVC/OAS)
2201 C Street, NW
Washington, DC 20520

10. SPONSOR/MONITOR’S ACRONYM(S)
DOS/AVC

11. SPONSOR/MONITOR’S REPORT NUMBER(S)

12. DISTRIBUTION / AVAILABILITY STATEMENT
Approved for Public Release; Distribution Unlimited.

13. SUPPLEMENTARY NOTES

14. ABSTRACT
We use three-dimensional nonlinear calculations of explosions at the North Korean test site, together with the representation theorem, to determine the effect of topography and depth on local and regional phases, and on long period surface waves and far-field body waves. We completed 5 three-dimensional nonlinear finite difference calculations using the topography of the North Korean test site at the estimated location and depth of the September 2017 nuclear test. The new calculations have yields of 12.5, 20 and 180 kilotons, plus two additional calculations at 180 kilotons that include tectonic stresses. We calculate large displacements of 2-4 meters on the mountain surfaces near the explosion, but very little displacement on the surface directly above the explosion which is very close to the mountain peak. This is most likely due to the topography with gravity increasing displacement on downhill slopes. We find that the topography increases the amplitude of the surface reflected pP phase for all events at this test site, however the effect is reduced for the 2017 explosion because of strong nonlinear interaction with the free surface. The North Korean explosions appear to be anomalous in generating much larger surface waves than are expected based on surface waves observed from buried explosions in other areas, however surface waves derived from the 3D calculations are a very good match to the observed surface waves. Calculations show that explosions at the base of a mountain have amplified surface waves, which explains part of the anomaly. The mountain reduces horizontal stresses, which has an effect similar to tensile tectonic stresses, so added tensile stresses cause only a small additional amplification. The remaining difference is attributed to low Ms bias in the global data set due to free surface interaction and compressive tectonic release.

15. SUBJECT TERMS
Nonlinear finite element calculations. Nuclear explosion monitoring. Topography. North Korea

16. SECURITY CLASSIFICATION OF:			**17. LIMITATION OF ABSTRACT**	**18. NUMBER OF PAGES**	**19a. NAME OF RESPONSIBLE PERSON** Rongsong Jih
a. REPORT UNC	**b. ABSTRACT** UNC	**c. THIS PAGE** UNC	SAR	84	**19b. TELEPHONE NUMBER** *(include area code)* 202-647-8126

Standard Form 298 (Rev. 8-98)
Prescribed by ANSI Std. Z39.18

Table of Contents

Figures

Tables

1. Summary

We use three-dimensional nonlinear calculations of explosions at the North Korean test site, together with the representation theorem, to determine the effect of topography and depth on local and regional phases as well as long period surface waves and far-field body waves. We completed 5 three-dimensional nonlinear finite difference calculations using the topography of the North Korean test site (Figure 1). The new calculations have yields of 12.5, 20 and 180 kilotons and are at a location 400 meters north of the earlier calculations. This corresponds to the inferred locations and yields of the January and September 2016 and September 2017 explosions, respectively. These new calculations are compared with earlier calculations which were all performed at 12.5 kilotons, and at depths of 100, 200, 540 and 800 meters. The new calculations were performed at a depth of 730 meters, which corresponds to the same elevation as the earlier 540m calculation. Two additional calculations were performed at 180 kilotons that included tensile and compressive tectonic prestress.

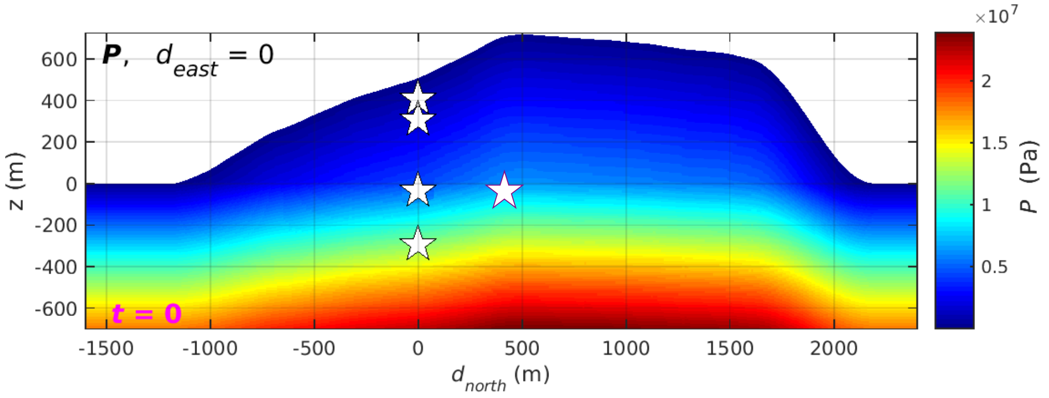

Figure 1. Topography and subsurface pressure showing the location of three-dimensional nonlinear calculations. The five new calculations were performed at the X=400 location, close to the inferred locations of the 2016 and 2017 explosions.

We calculate large displacements of 2-4 meters on the mountain surfaces near the explosion, but very little displacement on the surface directly above the explosion which is very close to the mountain peak (Figure 2). This is most likely due to the topography, with gravity increasing displacement on downhill slopes.

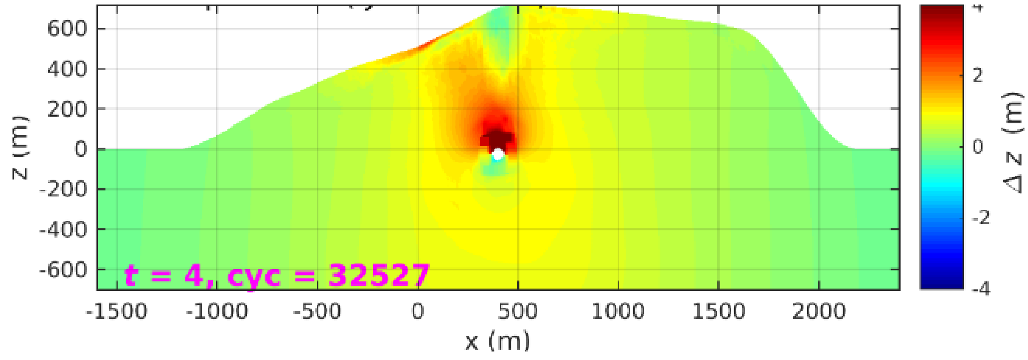

Figure 2. Vertical displacement from the NK2017 calculation along a south-north profile.

The North Korean explosions appear to be anomalous in generating much larger surface waves than are expected based on surface waves observed from buried explosions in other areas. Calculations show that explosions at the base of a mountain have amplified surface waves, which explains a substantial part of the anomaly. The mountain reduces horizontal stresses, which has an effect similar to tensile tectonic stresses, so added tensile stresses cause only a small additional amplification. Surface waves from the three-dimensional nonlinear calculations match the surface waves from the 2017 event (Figure 3) remarkably well, and also match the 2016 events. The remaining difference is attributed to reduced Ms in the global data set caused by the free surface interaction and compressive tectonic release.

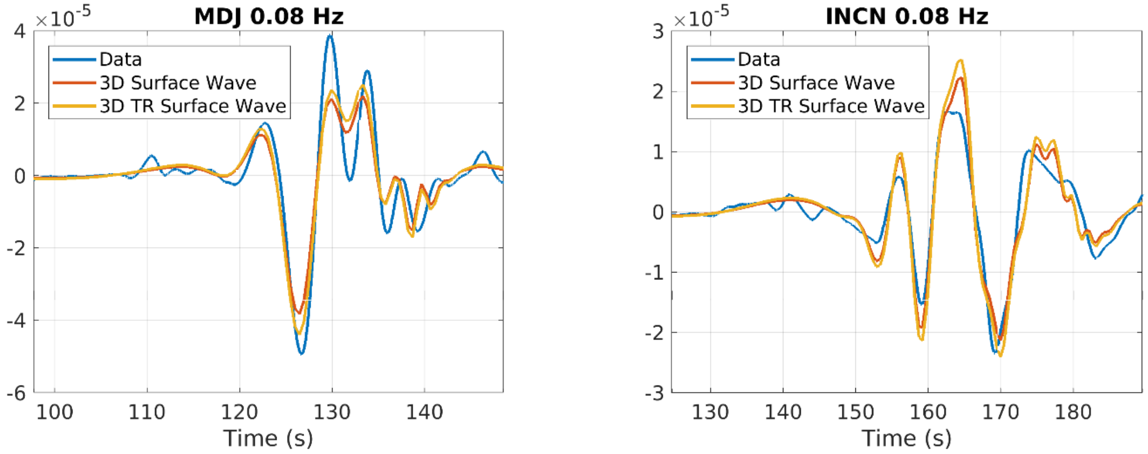

Figure 3. Calculated surface waves from the 2017 event with and without tectonic release, together with observed surface waves at two stations. With tectonic release (TR), surface waves are slightly larger in the direction of extension, at MDJ and INCN.

We find that the topography increases the amplitude of the surface reflected pP phase for all events at this test site, however the effect is reduced for the 2017 explosion because of strong nonlinear interaction with the free surface (Figure 4).

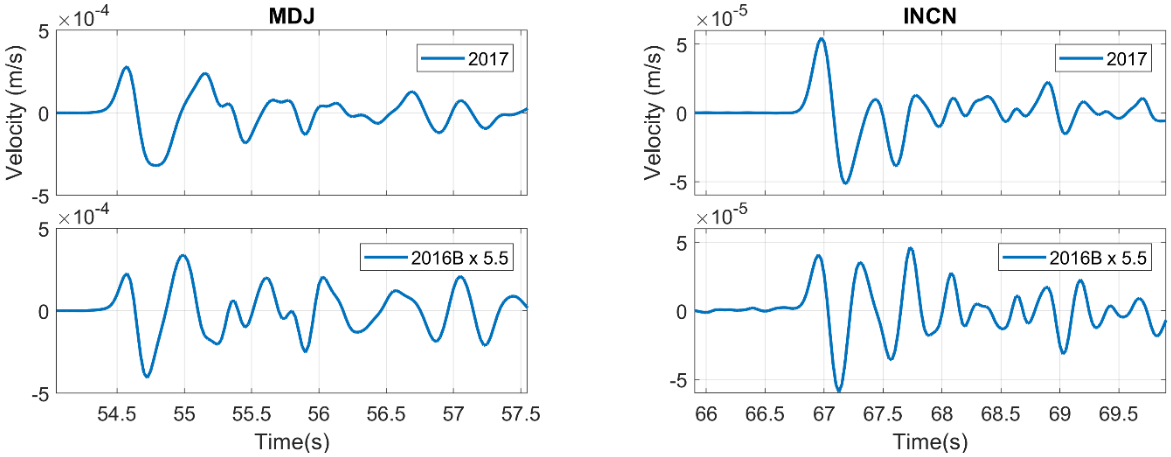

Figure 4. The pP phase is smaller in the 2017 explosion that in the 2016B explosion. The top figure in each plot above is the first arriving P-wave from the 2016 explosion and bottom is from 2016B. Left waveforms are from MDJ and right from INCN. All lowpass filtered at 5 Hz.

2. Introduction

2.1 The North Korean Nuclear Explosions

On September 3, 2017, the Democratic People's Republic of Korea (DPRK) conducted its sixth announced nuclear test. The seismic signals from this test were much larger than the signals from the previous 5 tests. The last 5 explosions were all conducted in Mt. Mantap. A map provided by NORSAR[1] derived from Gibbons et al. (2017) showing the estimated locations for all of the explosions is shown in Figure 5.

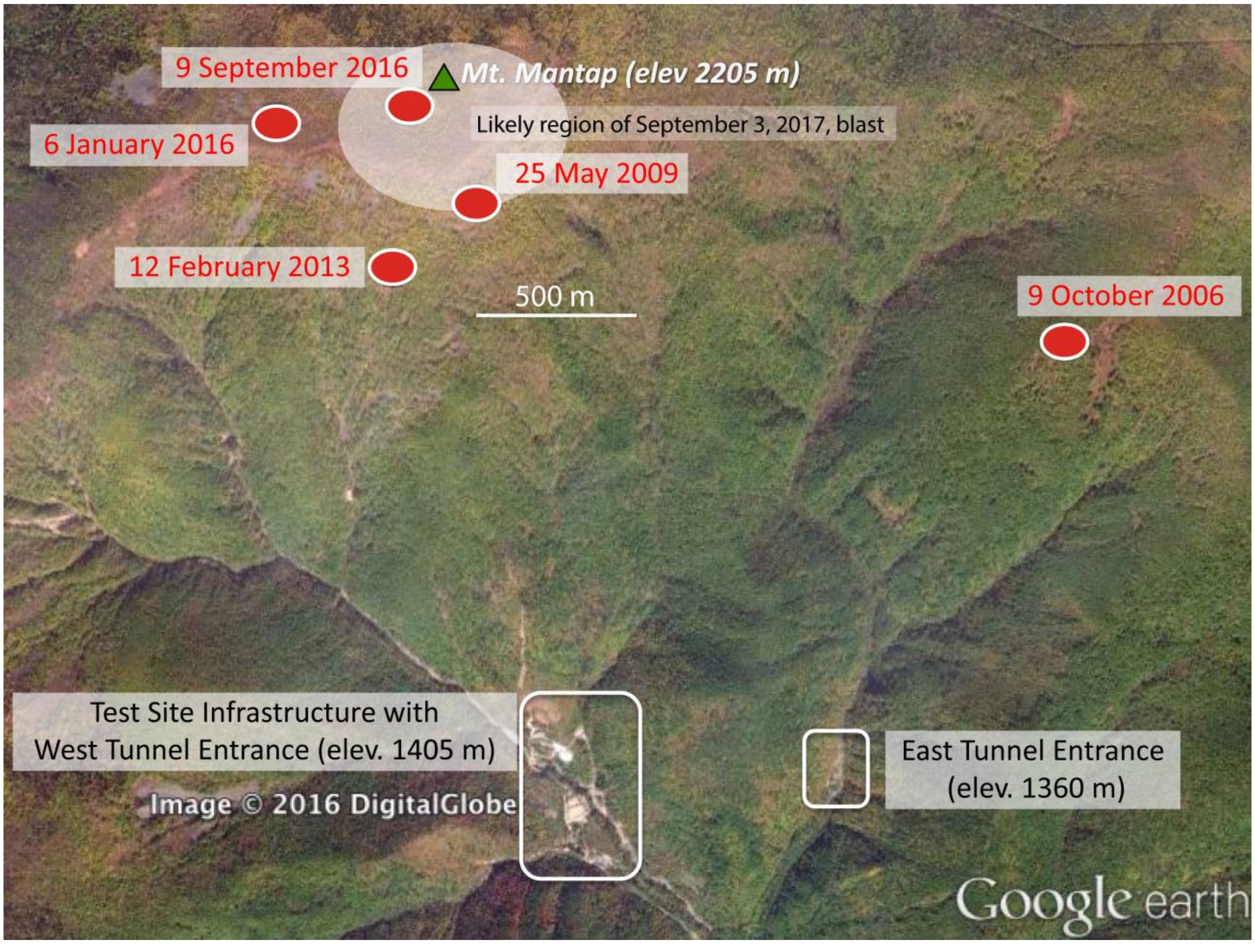

Figure 5. Estimated locations of the six North Korean nuclear explosions.

Figure 6 shows the surface wave magnitude Ms and its standard deviation calculated from the 5 closest stations, using Russell's formula for Ms (Russell, 2006; Bonner et al, 2006). The surface wave signals are remarkably consistent from event to event and the standard deviation for each event is very small. Because of this consistency, we can use the surface wave amplitude as a scaling factor to estimate the relative yields for each event. Murphy et al (2013) estimated a yield of 4.60 kilotons for the 2009 event. We use this together with the surface wave amplitudes to estimate a yield for all 6 explosions. The Ms and yield points are shown in Figure 7 together with the global Ms:Yield curve from Stevens and Murphy (2001), and the estimated yields are listed

---

[1] https://ds.iris.edu/ds/nodes/dmc/specialevents/2017/09/03/2017-north-korean-nuclear-test/

in Table 1. As can be seen in the figure, the surface waves from all of these explosions were quite large compared to the global average for events of the same yield.

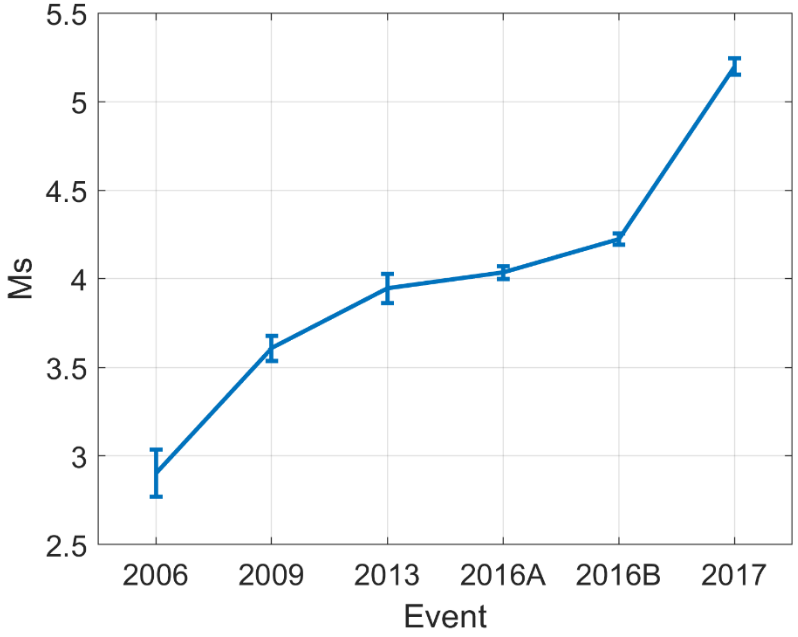

Figure 6. Ms average and standard deviation for each of the 6 North Korean explosions.

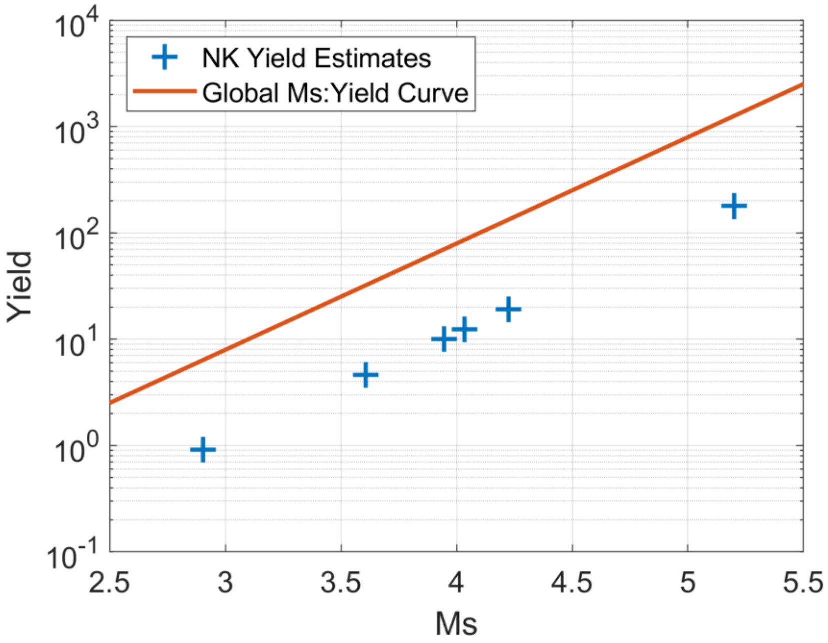

Figure 7. Estimated yield in kilotons vs. Ms for the six North Korean explosions. The line is the global Ms:Yield curve from Stevens and Murphy (2001).

Table 1. Measured Ms and estimated yield from the six announced North Korean nuclear tests

Event	Ms	Estimated Yield (kt)
2006 10 09	2.90 ± 0.14	0.91
2009 05 25	3.61 ± 0.07	4.60
2013 02 12	3.95 ± 0.08	10.0
2016 01 06	4.04 ± 0.04	12.3
2016 09 09	4.23 ± 0.03	19.0
2017 09 03	5.20 ± 0.05	180

The estimated yield of 180 kilotons for the 2017 event is consistent with other yield estimates for this event. J. R. Murphy estimated 200 kilotons from his analysis of the observed network-averaged teleseismic P wave spectrum for that explosion in which he assumed a source depth of 800 meters (personal communication, October, 2017). Several other yield estimates are referenced on the Iris special event page: NORSAR estimated 120 kt, and later revised the yield estimate to 250 kt , The University of Science and Technology of China estimated 108.3±48.1 kt. The Comprehensive Nuclear Test Ban Treaty Organization estimated a range of 140 to 450 kt.

3. Technical Approach

3.1 The CRAM3D Code

CRAM 3D is an explicit three-dimensional Lagrangian finite element code designed to run on multiple processors (Stevens et al, 2011, 2017, 2017a). For an explosion simulation, the cavity is placed near the center of the grid and is enclosed by a spider grid which facilitates applying the pressure boundary condition and rezoning elements (Figure 8). The code includes gravity and so includes the important effects that result from variation of overburden pressure with depth. Gravitational equilibrium is established by running an initial calculation with no source, which is followed by a second calculation including the explosion source. CRAM3D also has the capability to include tectonic prestress in the calculations.

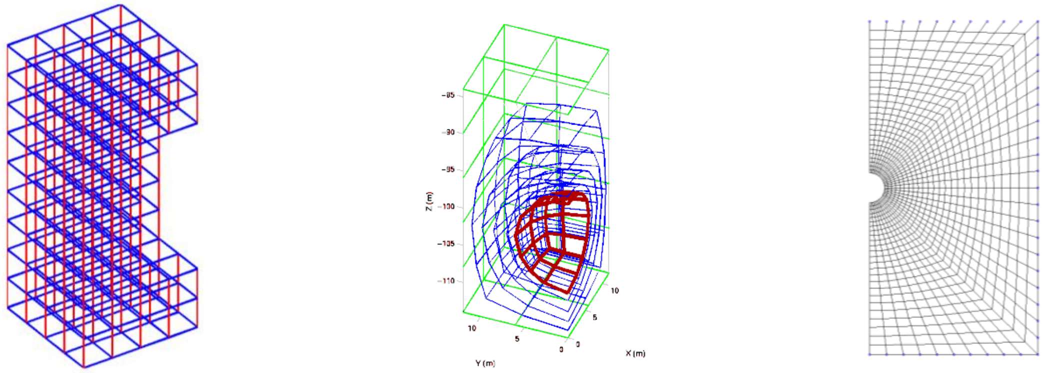

Figure 8. The CRAM 3D finite element outer grid (left) is rectangular. The inner grid (center) is shaped to match the shape of the explosion shock wave. CRAM2D uses a similar axisymmetric spider grid (right) in the region around the explosion.

3.2 Propagation with the Elastodynamic Representation Theorem

The representation theorem allows us to perform arbitrarily complex nonlinear calculations in the source region, and then propagate them with an appropriate Green's function. The representation theorem is exact. That is, no matter how complex the 3D motion is on the source region boundary, it will be correctly propagated by the representation theorem. The only exception is that it will not calculate the interaction of backscattered waves reflected from outside the source region with complexities of the source region.

In the three-dimensional numerical calculations, we save displacements and stresses on a monitoring surface on the boundary of a rectangle (5 planar surfaces, excluding the upper surface), and calculate Green's functions from each point on the monitoring surface to the receiver and so the synthetic seismogram at the receiver point *X* outside of the monitoring surface is obtained by integrating over the monitoring surface S_M

$$u_i(X) = \int_{S_M} \left\{ G^i_j(\xi; X) * T^M_j(\xi) - u^M_j(\xi) * S^i_{jk}(\xi; X) n_k \right\} dA$$

in the frequency domain, where $G_j^i(\xi;X)$ and $S_{jk}^i(\xi;X)$ are the Green's function and the stress tensor on the monitoring surface due to a unit impulsive force at X in direction i, T_j^M is the traction on the monitoring surface due to the seismic source, u is the displacement on the monitoring surface, and n is the normal to the monitoring surface. The operator * denotes convolution and the summation convention is assumed.

We use a plane-layered Green's function outside the source region. The Green's functions for the complete seismograms are derived from an algorithm based on the work of Luco and Apsel (1983) and Apsel and Luco (1983). The technique used for surface waves is similar to the method of Bache et al. (1982). The Green's functions for body waves are generated by a procedure similar to that described by Bache and Harkrider (1976) using a saddle point approximation to calculate a far-field plane wave for a given takeoff angle from a source in a plane-layered medium. Although the full waveform Green's functions generate the complete waveform, the other Green's functions provide additional insight into the source and waveform generation.

3.3 Numerical Modeling of the North Korean Nuclear Explosions

We have performed several three-dimensional nonlinear explosion calculations using the topography of the North Korean test site (NASA et al, 2009). Four calculations were performed at different depths at the estimated location of the 2009 explosion, all with yields of 12.5 kilotons. Four calculations were performed at the estimated location of the 2017 explosion, which was also very close to the location of the two 2016 explosions, with yields of 12.5, 20 and 180 kilotons, close to the yields of those three events. Two additional calculations were performed at 180 kilotons with tensile tectonic stresses included. The location of the 2009 event is from Zhang and Wen (2013), the 2016 event locations are from Gibbons et al (2017), and the 2017 location is provided by NORSAR on the IRIS special event page. Murphy et al (2013) estimated the depth of the 2009 event as 540 meters, which is also consistent with the observed adit location. The depth of the 2016-2017 explosion calculations is 730 meters below the surface and close to the peak of Mt. Mantap, at the same elevation as the 540 meter calculation. The locations of the explosion calculations are shown in Figure 9, and the depths and yields of the calculations are listed in Table 2.

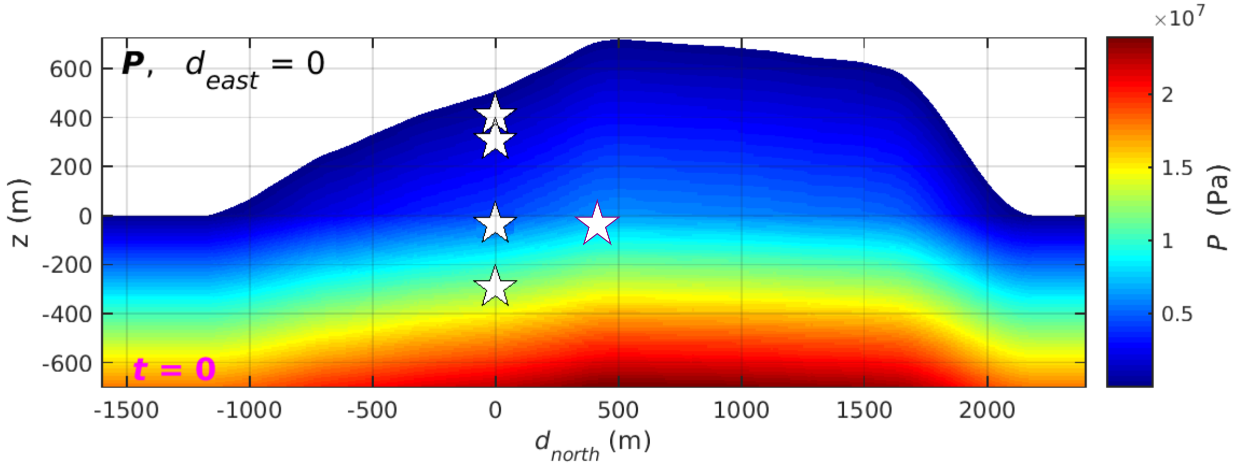

Figure 9. Four 3D calculations were performed at depths 100, 200, 540, 800 meters, at location zero in south-north distance in the figure, all at 12.5 kt. Four additional calculations were performed 400 meters north, at 730m depth, which is the same elevation as the 540m calculation, with yields of 12.5, 20 and 180 kilotons and at 180 kt with tectonic stresses added. The topography used in the calculation corresponds to the actual test site topography. Colors show the pressure in the initial equilibrium state.

Table 2. North Korea Calculations

Calculation	Source Depth (m)	Yield (kt)
NK-100	100	12.5
NK-200	200	12.5
NK-540	540	12.5
NK-800	800	12.5
NK2016A	730	12.5
NK2016B	730	20
NK2017	730	180
NK2017TR/TH	730	180

The calculations are performed using the CRAM3D code discussed earlier. For the North Korean calculations we use a uniform material model with granite properties previously used for a calculation of the Shoal nuclear explosion (Stevens and Thompson, 2015). The grid contains zone dimensions 400x340x140 in the X, Y and Z directions, which correspond to North, West, and Up. Grid nodes were spaced 10 m horizontally ranging from 1600 m south to 1400 m north and 1700 m west to 1700 m east, and vertically every 5 m at the grid edges. The smaller nodes in the vertical direction are necessary because the calculation expands the nodes under the mountain to develop a smooth grid with the topography.

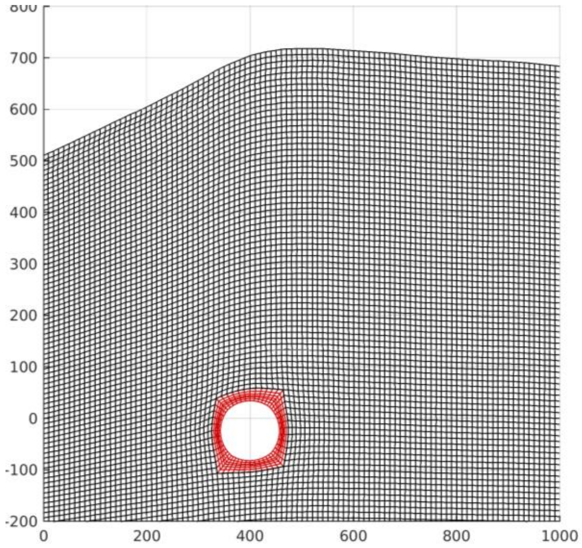

Figure 10. Final grid near the cavity at the end of the NK2017 calculation (4 seconds). Depth and location units are meters.

The initial cavity size at the start of the calculation corresponds to the vaporization radius of the explosion, which is calculated using the approximate relation that a nuclear explosion vaporizes 70 tons of rock per kiloton of explosion. For 180 kilotons yield in a rock with density 2600 kg/m^3, the vaporization radius is 10.5 meters. The cavity expands to a final radius of 58.5 meters (Figure 10).

Figure 11 shows the pressure field at 0.1 and 0.2 seconds. At 0.1 seconds the pressure is a nearly perfect spherical wave embedded in the initial hydrostatic pressure field. By 0.2 seconds, the pressure wave is strongly interacting with the free surface with a tensile wave propagating downward from the surface reflection. Figure 12 shows the regions of nonlinear deformation and tensile cracking at the end of the calculation.

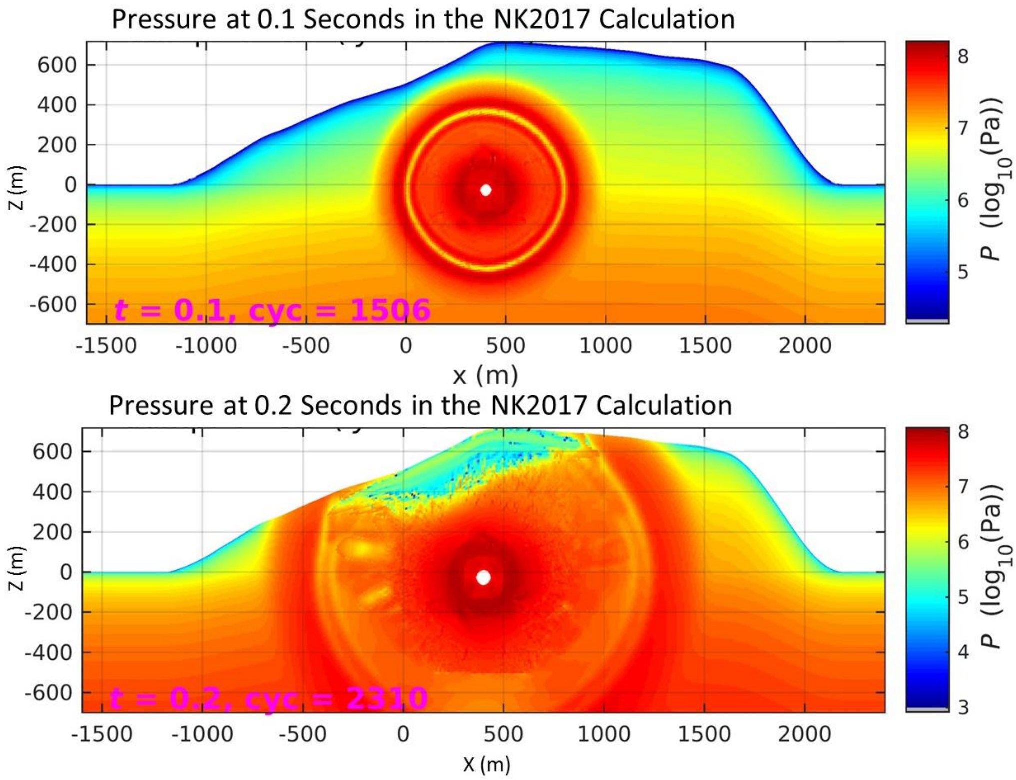
Pressure at 0.1 Seconds in the NK2017 Calculation

Pressure at 0.2 Seconds in the NK2017 Calculation

Figure 11. Pressure at 0.1 seconds (top) and 0.2 seconds (bottom) from the NK2017 calculation.

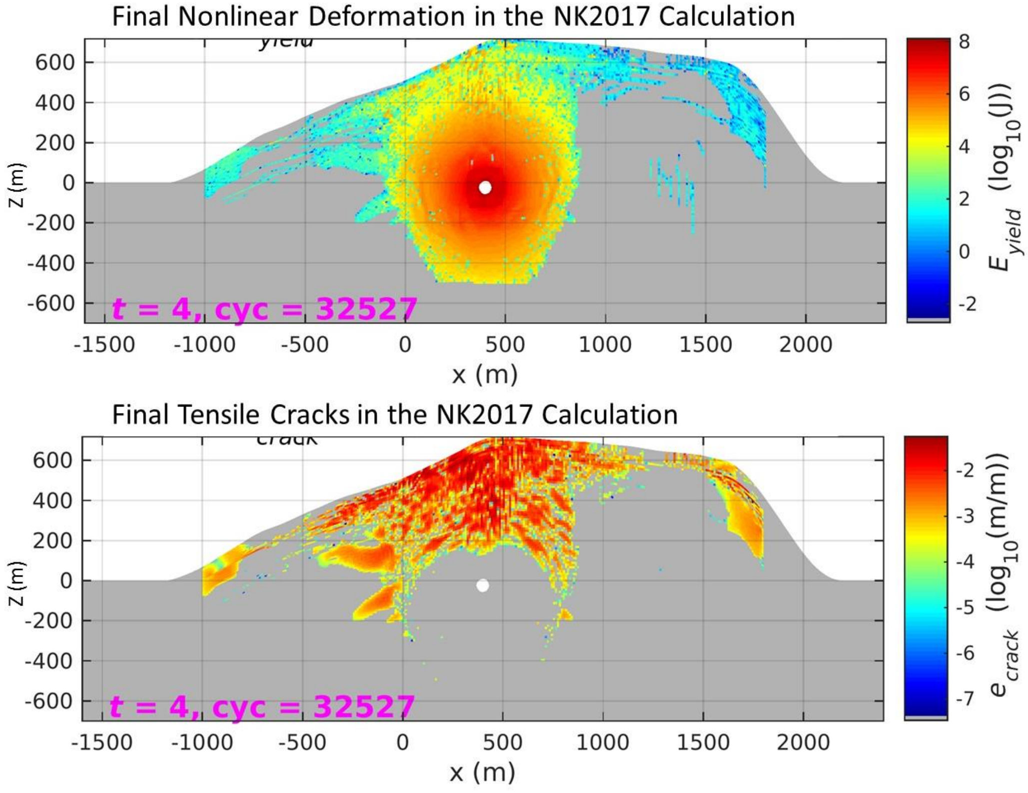
Final Nonlinear Deformation in the NK2017 Calculation

Final Tensile Cracks in the NK2017 Calculation

Figure 12. Final nonlinear deformation (plastic work, top) from the NK2017 calculation. Regions of tensile cracking (crack strain, bottom).

4. Results and Discussion

4.1 Surface deformation and spall from the NK2017 explosion

The 2017 explosion was large enough to generate observable surface deformation (Pabian, 2017). The calculations also generated large deformations which are strongly affected by the topography. Figure 13 shows cross sections of the final displacements along north-south profile and Figure 14 along an east-west profile. The calculations show vertical displacement of up to 4 meters and horizontal displacement of up to 2 meters, with the largest displacements occurring on the slope south of the explosion. The effect of gravity is strong, moving deformation away from the mountain top and down the southern slope. While there are large displacements on the slope, there is minimal displacement on the top of the mountain immediately above the explosion. Both of these effects – large displacements on the slope and minimal displacement near the peak, have been observed using radar data acquired by the German TerraSAR-X satellite (Wang et al, 2017).

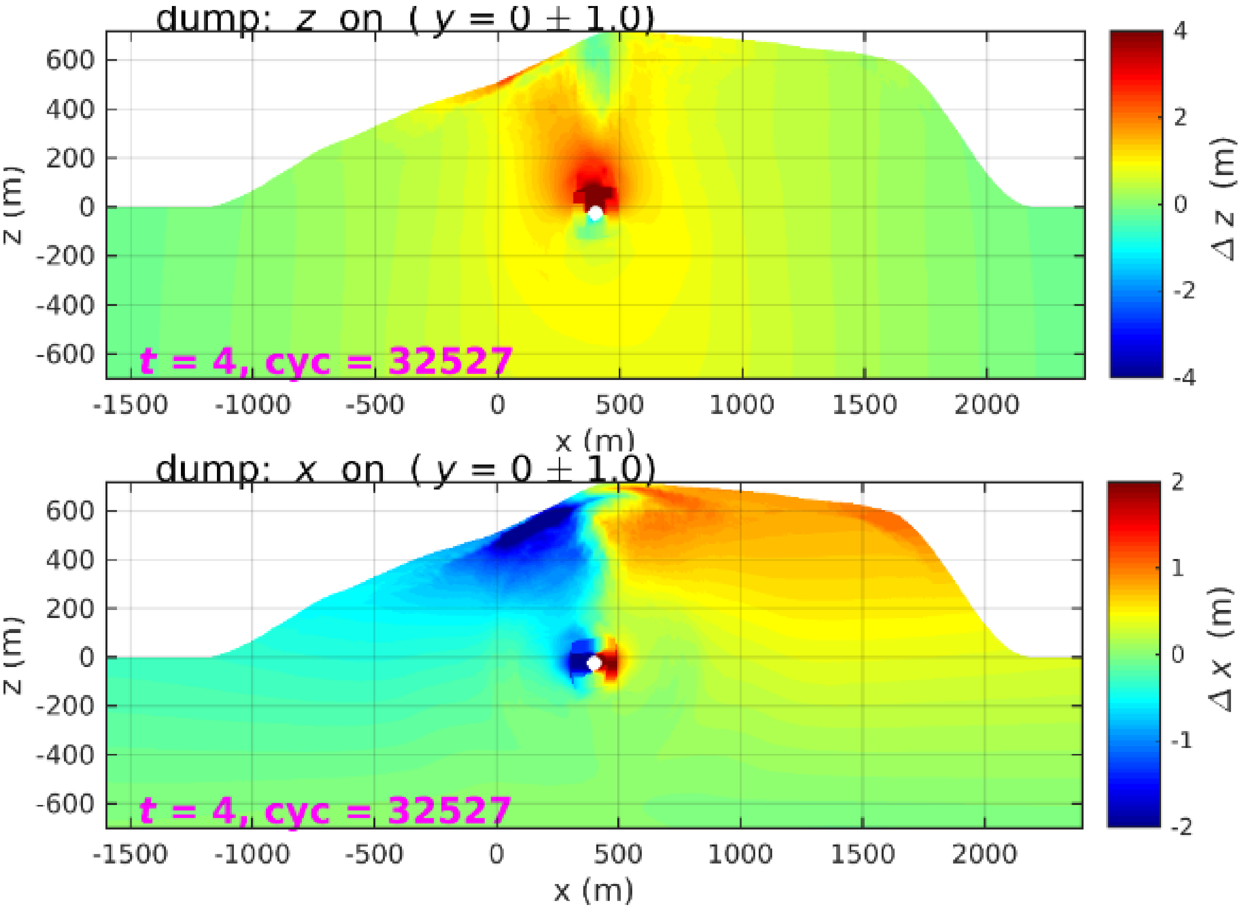

dump: z on (y = 0 ± 1.0)

dump: x on (y = 0 ± 1.0)

Figure 13. Displacement from the NK2017 calculation along a south-north profile. Top: vertical displacement. Bottom: horizontal displacement.

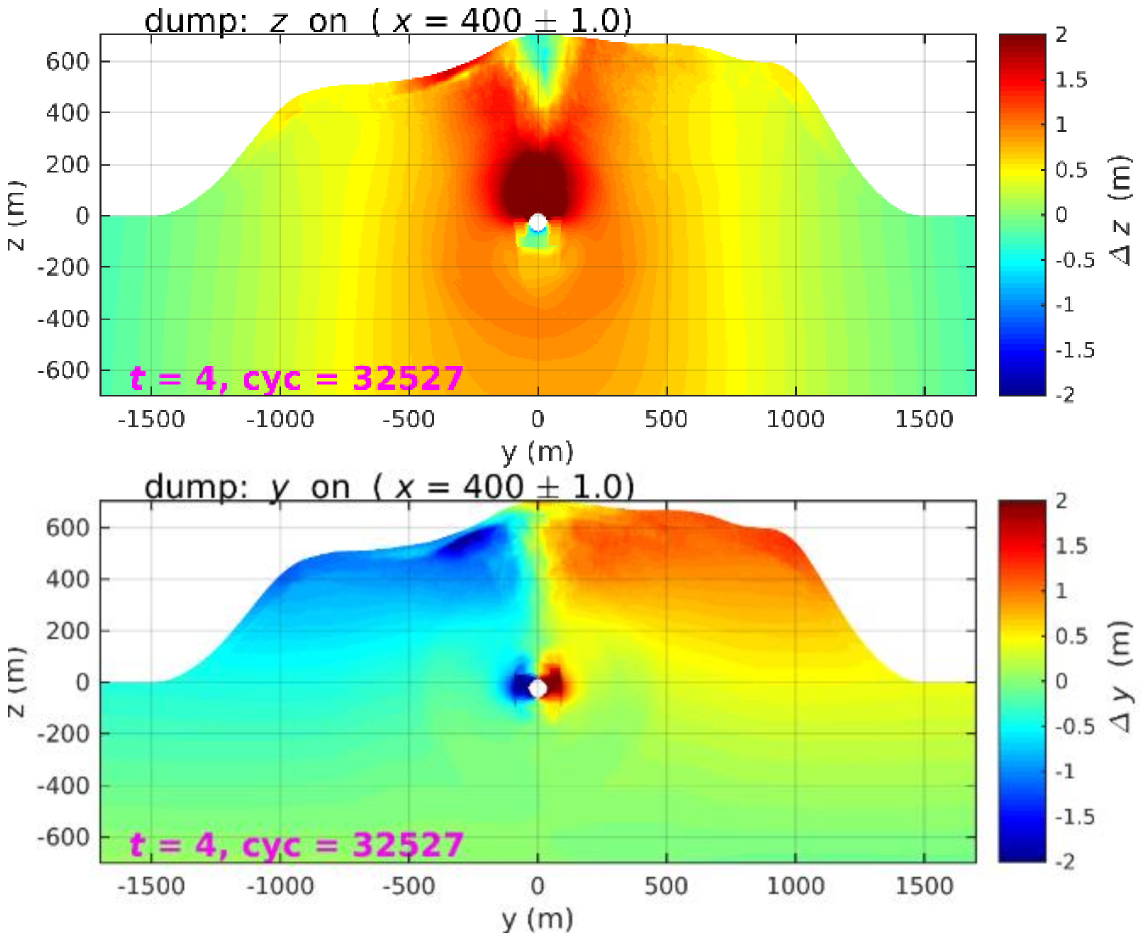

Figure 14. Displacement from the NK2017 calculation along a west-east profile. Top: vertical displacement. Bottom: horizontal displacement.

Figure 15 shows the vertical and horizontal displacement on the surface above the explosion. The arrows show the magnitude and direction of the horizontal displacement and the colors show the vertical (top picture) and horizontal (bottom picture) displacement. The blue spot in each show the minimal displacement immediately above the explosion. In fact the vertical displacement is slightly negative (subsidence). The horizontal displacement, however, is as large as two meters downslope to the south of the peak. Vertical displacement is also large in this area. The effect of gravity on the steep slopes is strong here, causing displacement to shift from the peak to the southern slope.

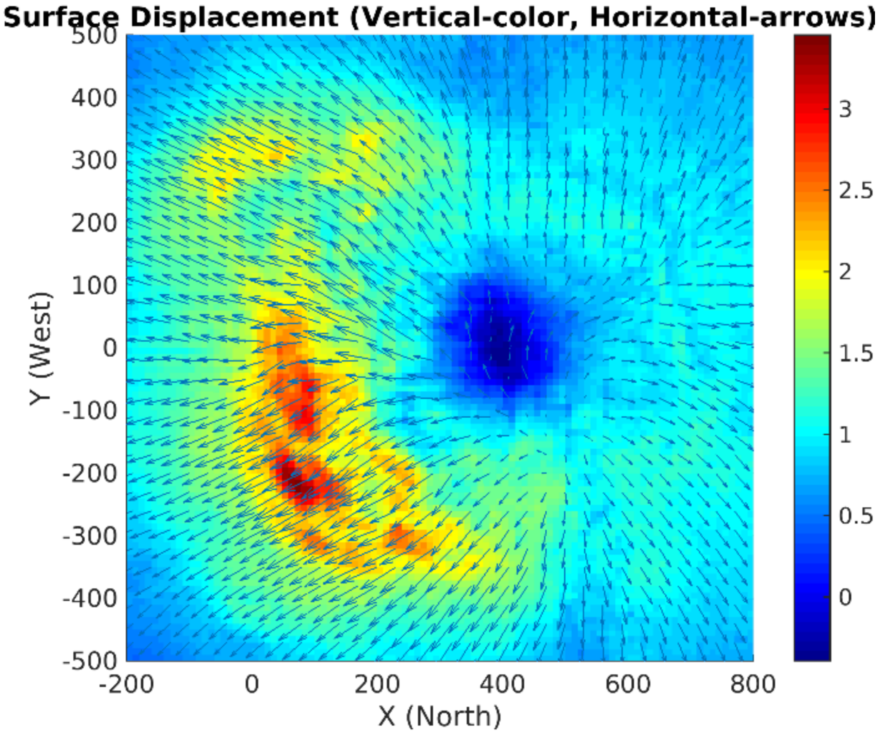

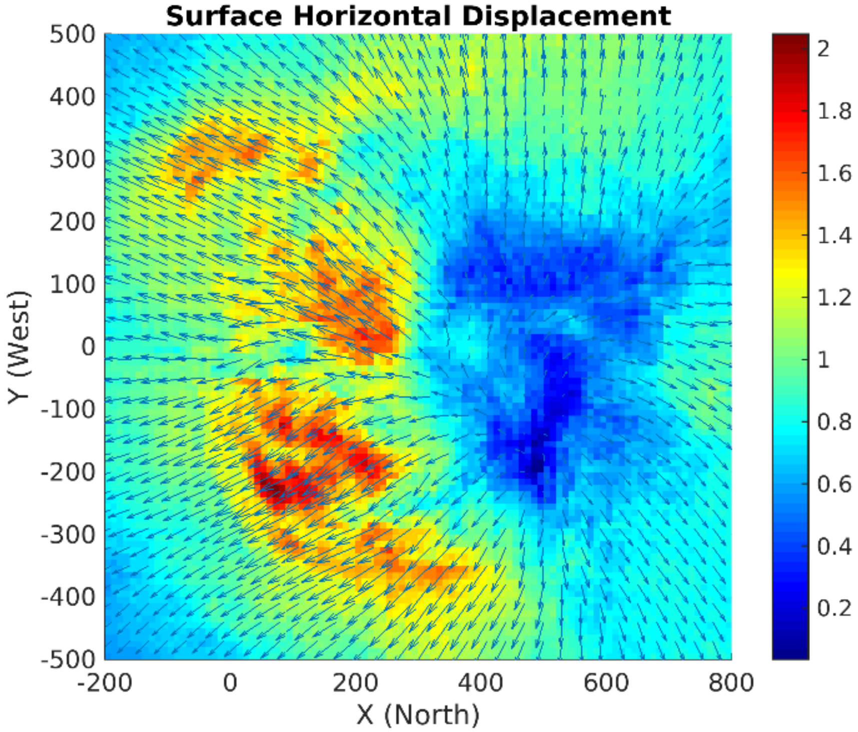

Figure 15. Overhead view of surface displacement near the explosion. The explosion is at X=400, Y=0. Top: Vertical displacement shown in color, horizontal displacement magnitude and direction shown by arrows. Bottom: Horizontal displacement magnitude shown by colors, magnitude and direction by arrows.

4.2 Spall from the NK2017 explosion.

The calculations also show substantial spall on the surface. Spall occurs when the interaction of the upgoing wave and the reversed polarity downgoing wave interact to cause the upper layers of the earth to detach and travel on a ballistic path. That is, they are thrown up in the air, and then come down under the acceleration of gravity. This is visible in seismic records as a slope in the vertical velocity corresponding to the acceleration of gravity (Figure 16).

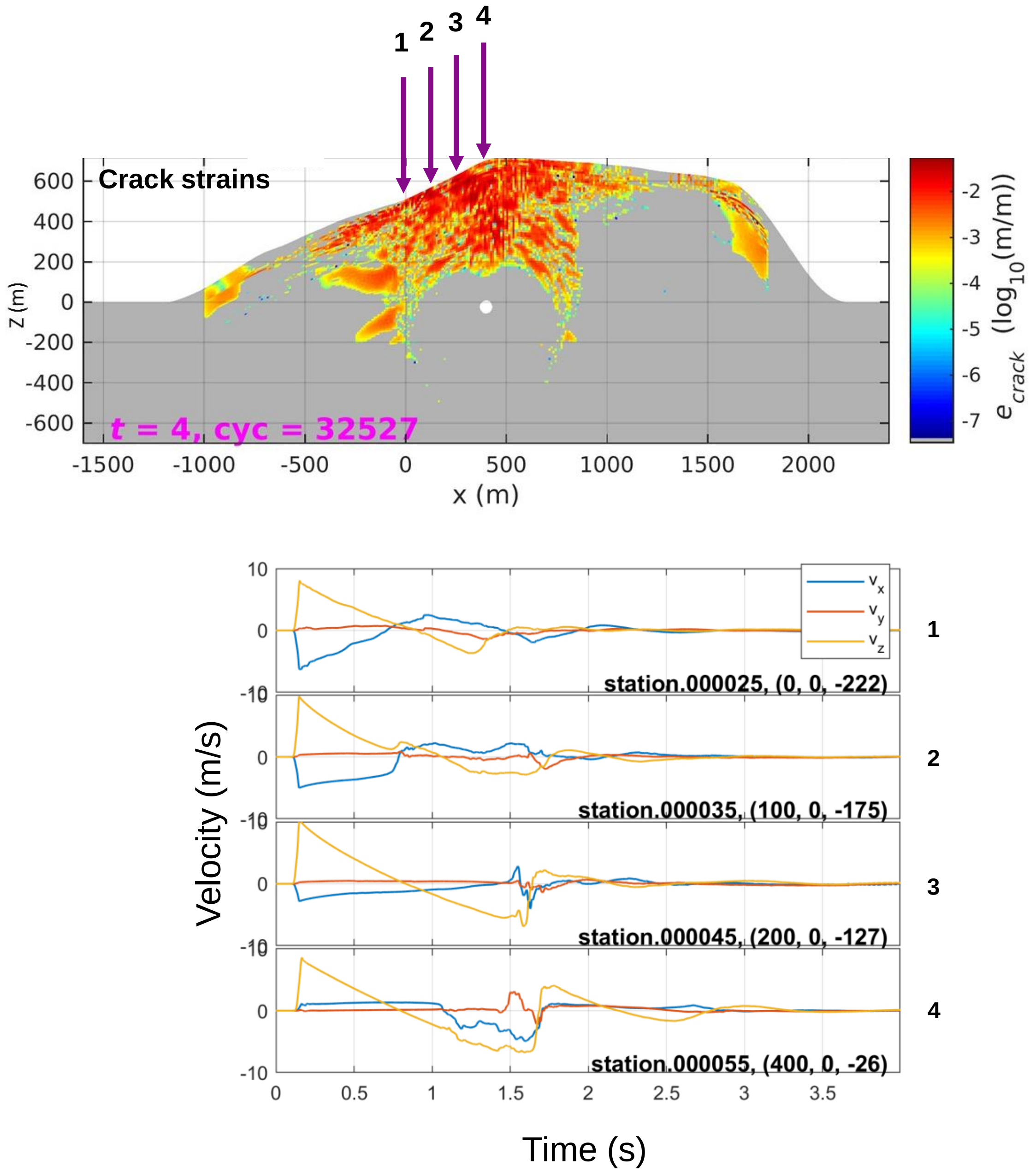

Figure 16. Cracking and spall from the 2017 calculation. Top: regions of tensile cracking shown as crack strains, together with the locations of the seismic records shown on the bottom. Bottom: vertical, radial and tangential velocity records at the four locations shown on the top. The constant slope in the first 1.5 seconds indicates spall.

4.3 Comparison of nonlinear deformation for all calculations

Figure 17 shows the regions of nonlinear deformation and cracking for all of the earlier calculations, including Shoal, and Figure 18 shows the regions of nonlinear deformation and cracking for the new calculations. Note that the new calculations are close to the peak of Mt. Mantap, while the earlier calculations were 400 meters downslope to the south. The Shoal calculation was at 370m depth in the same material, but with a flat surface. The new calculations are shown at a different scale since the area of nonlinear deformation is so much larger for the 2017 explosion. All of the calculations have substantial nonlinear interaction with the free surface, however, including the calculation at 800 meters depth.

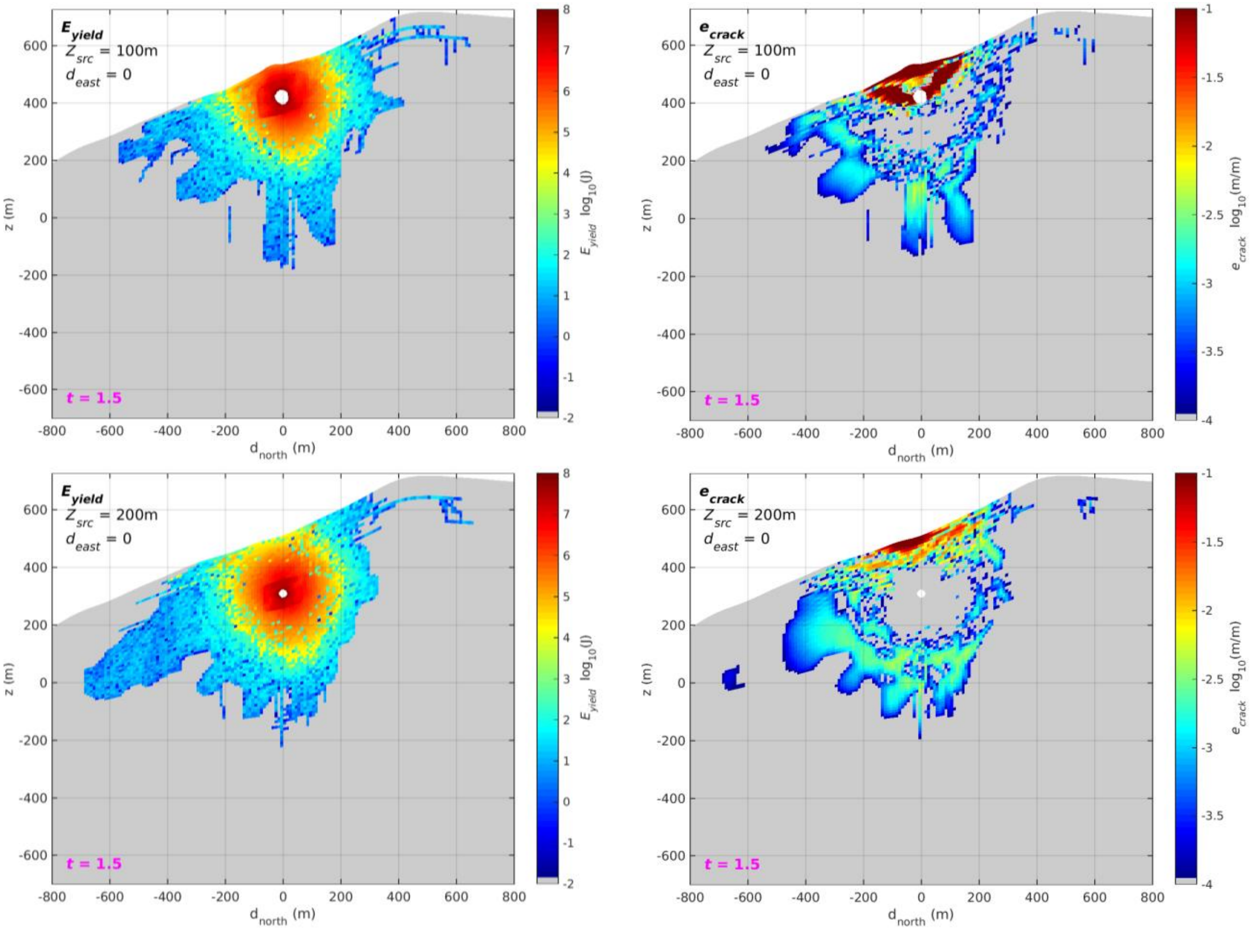

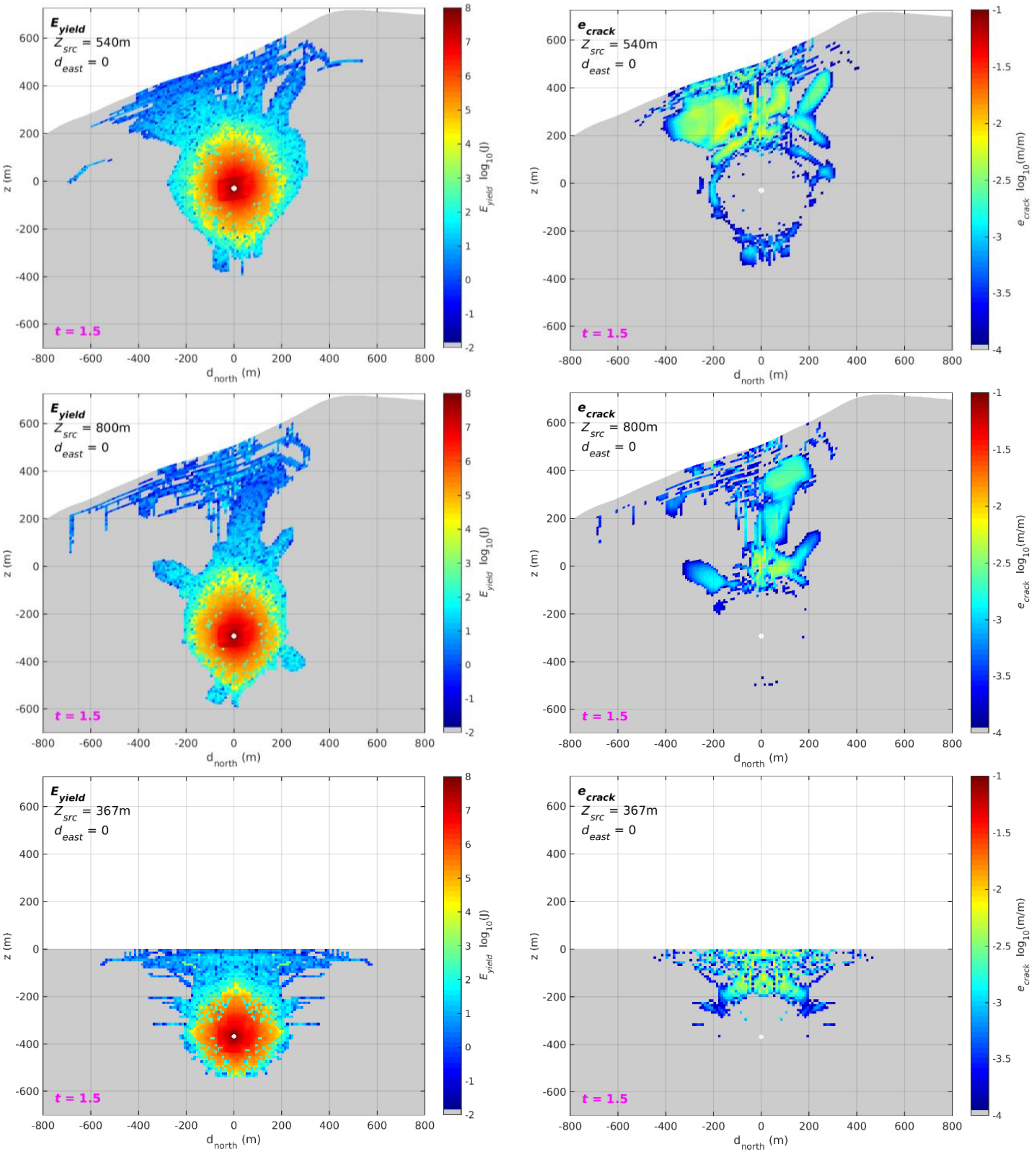

Figure 17. Left: nonlinear deformation (plastic work). Right: tensile crack strains. From top to bottom: NK-100, NK-200, NK-540,NK-800, Shoal. All calculations were at 12.5 kiloton yield.

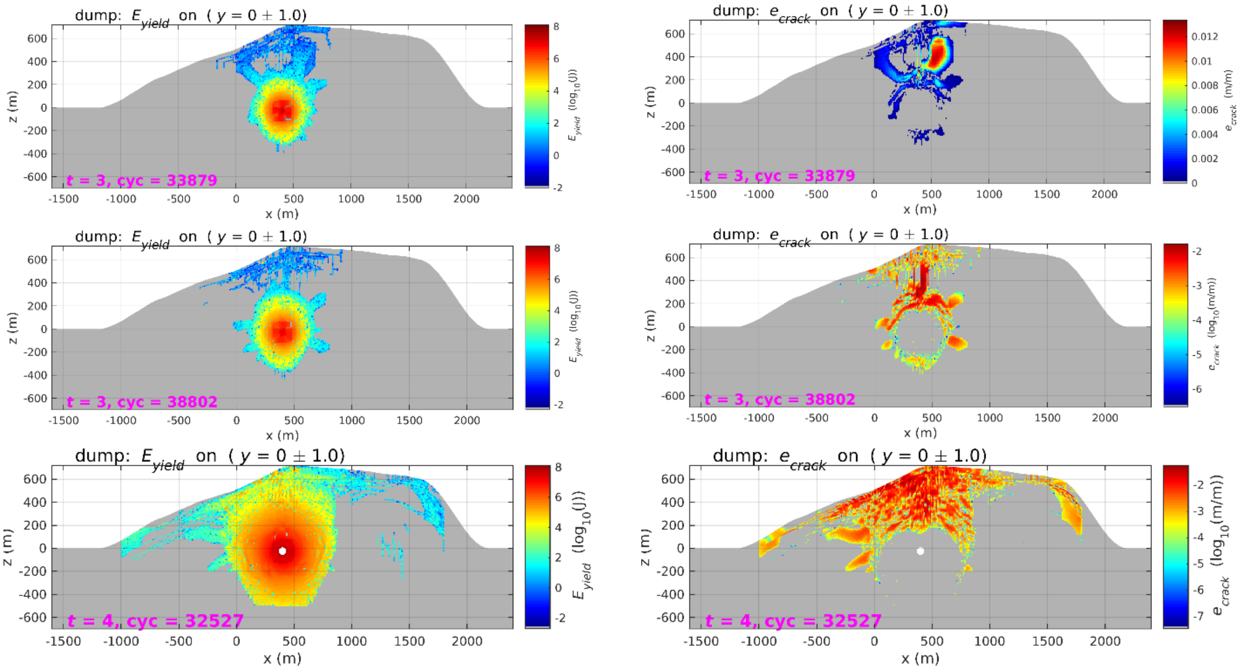

Figure 18. Left: nonlinear deformation (plastic work). Right: tensile crack strains. From top to bottom: NK2016A (12.5 kt), NK2016B (20 kt), NK2017 (180 kt).

4.4 Calculation of seismic waves using the representation theorem

We use the representation theorem to propagate the calculation from the near field to regional and teleseismic distances as discussed earlier. The finite element grid is tapered to have the same surface elevation at all points on the monitoring surface, and we embed this in an external model with the same material properties on the monitoring surface. We use Green's functions for surface waves, full waveform regional seismograms and far-field body waves calculated from a plane-layered earth model outside the source region.

4.4.1 Earth models used for propagation

We use two types of models for propagation: 1) a regional model corresponding to the structure at the North Korean Test Site; and 2) path specific models derived from observed surface waves. The regional model, listed in Table 3, is the earth model at the location of the North Korean test site from Stevens et al (2005), with the 2 km surface layer replaced with the properties of the granite model used in the nonlinear calculations. Q was set to a uniform value of 400 in the crust and upper mantle from 4 to 80 km depth. We use this structure for the common set of distance and azimuth calculations.

Table 3. Regional material model for the North Korea test site

Depth km	Thickness km	Vp km/s	Vs km/s	Density g/cm^3	Q
2.0	2.0	5.175	3.025	2.600	200
4.0	2.0	5.356	3.100	2.625	300
6.0	2.0	5.538	3.170	2.650	400
8.0	2.0	5.719	3.240	2.675	400
11.0	3.0	5.900	3.312	2.700	400
22.0	11.0	6.402	3.593	2.736	400
32.0	10.0	7.016	3.938	2.960	400
48.0	16.0	8.031	4.508	3.330	400
64.0	16.0	7.736	4.343	3.223	400
80.0	16.0	7.431	4.171	3.111	400
100.0	20.0	7.434	4.173	3.112	75
120.0	20.0	7.587	4.259	3.168	75
142.5	22.5	7.733	4.341	3.221	76
165.0	22.5	7.828	4.394	3.256	76
187.5	22.5	7.929	4.450	3.293	77
210.0	22.5	8.110	4.553	3.359	78
235.0	25.0	8.366	4.696	3.453	134
260.0	25.0	8.586	4.820	3.533	135
∞	∞	8.742	4.832	3.541	137

For the 5 closest stations, we derive path structures by inversion of the observed fundamental mode surface waves at each station. These stations are shown in Figure 19 and listed with the distance and azimuth from the test site in Table 4.

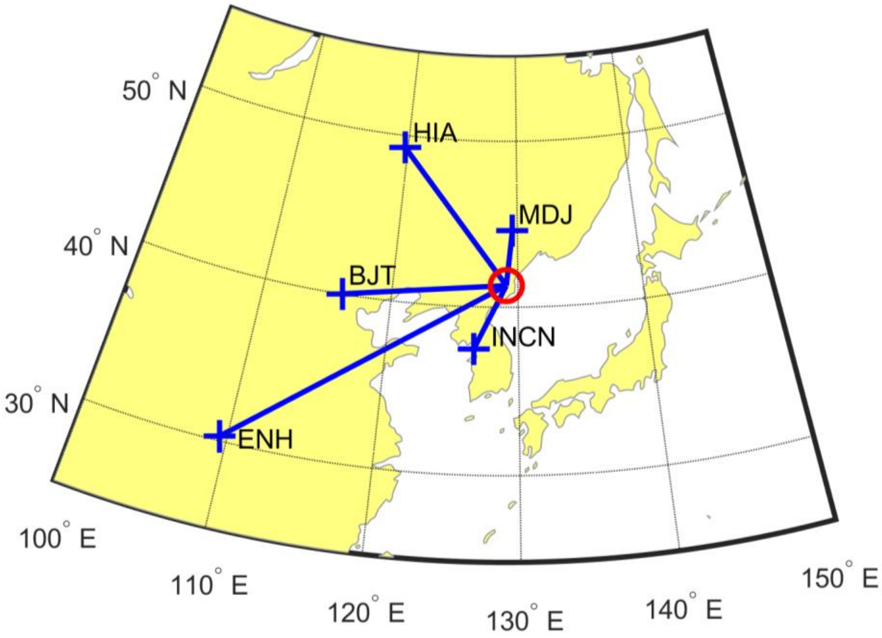

Figure 19. Map showing the 5 GSN stations (blue crosses) closest to the North Korean test site (red circle). Blue lines are great circle paths.

Table 4. 5 GSN stations closest to the North Korean Test Site

Station	Distance (km)	Azimuth (degrees)
BJT	1097	267
ENH	2142	241
HIA	1147	324
MDJ	371	6
INCN	478	207

The procedure for measuring phase and group velocity dispersion curves and inverting for earth structure is described by Stevens (1986), Stevens and McLaughlin (2001) and Stevens et al (2005, 2008). Dispersion curves were obtained for the three largest explosions and then averaged for each station. Amplitudes were averaged using a scaling factor for each event so that they each had a common mean. The phase and group velocities and amplitudes together with their standard deviations are shown in Figure 20. These were derived from the surface waves from the largest three explosions (refer to Table 1). Both the dispersion curves and spectral amplitudes are very consistent at each station. Standard deviations are quite small.

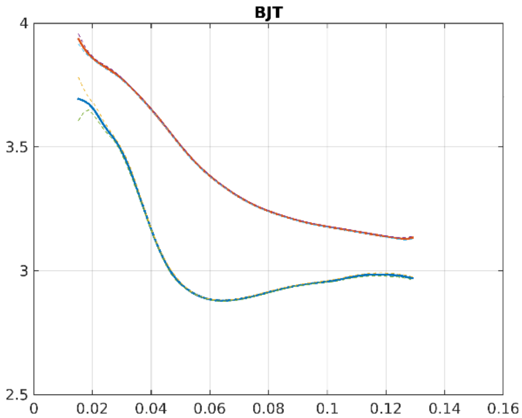
BJT
4
3.5
3
2.5
0
0.02
0.04
0.06
0.08
0.1
0.12
0.14
0.16

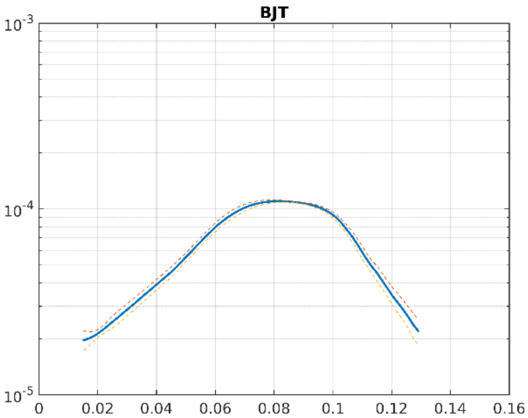
BJT
10^-3
10^-4
10^-5
0
0.02
0.04
0.06
0.08
0.1
0.12
0.14
0.16

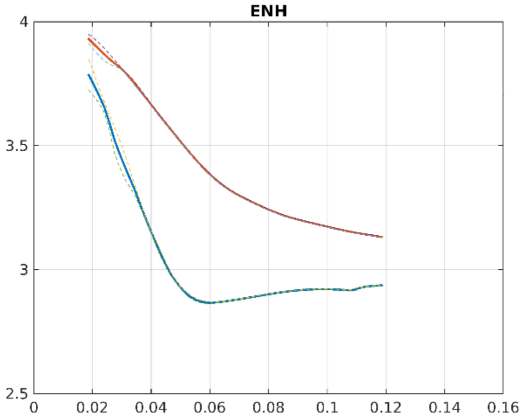
ENH
4
3.5
3
2.5
0
0.02
0.04
0.06
0.08
0.1
0.12
0.14
0.16

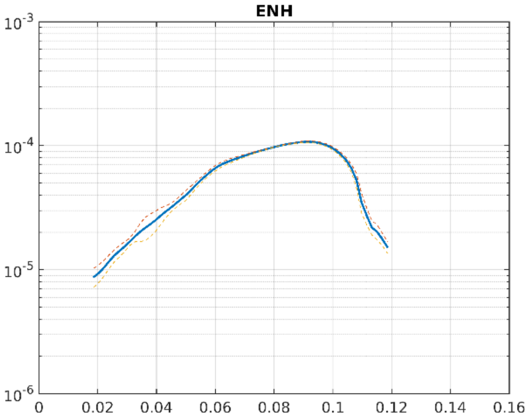
ENH
10^-3
10^-4
10^-5
10^-6
0
0.02
0.04
0.06
0.08
0.1
0.12
0.14
0.16

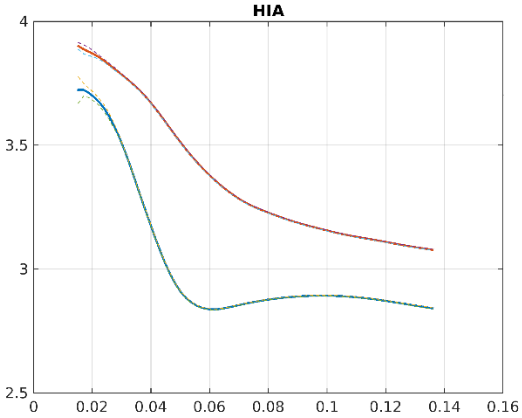
HIA
4
3.5
3
2.5
0
0.02
0.04
0.06
0.08
0.1
0.12
0.14
0.16

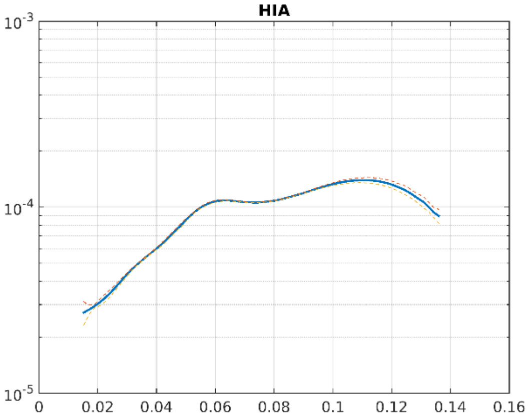
HIA
10^-3
10^-4
10^-5
0
0.02
0.04
0.06
0.08
0.1
0.12
0.14
0.16

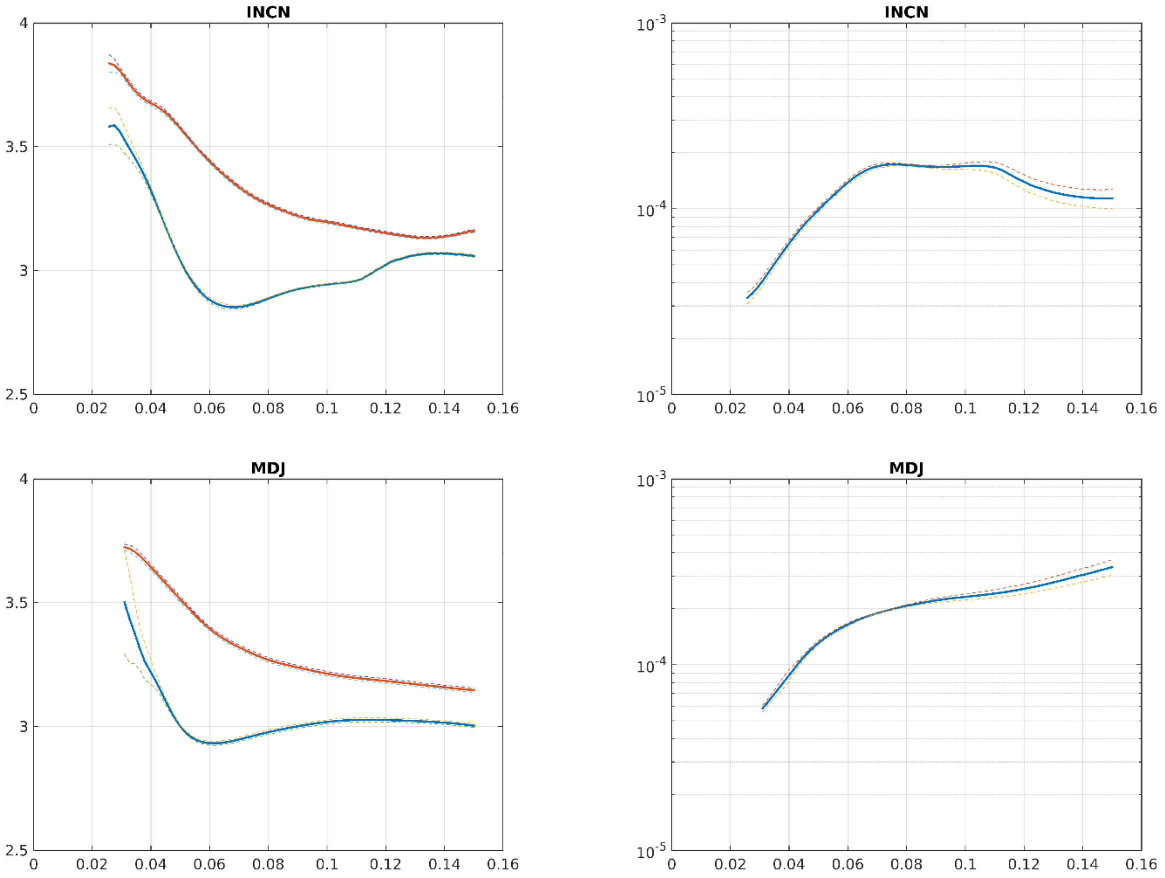

Figure 20. Phase velocity (red) and group velocity (blue) on the left and spectral amplitude (right) for each of the 5 closest GSN stations. From top to bottom: BJT, ENH, HIA, INCN and MDJ. Dashed curves are the standard deviations in the measurements for 3 events.

Phase and group velocity dispersion curves were inverted for shear velocity structure, while compressional velocity and density were constrained by a Poisson's ratio of 0.2405 and Birch's law of $\rho = 0.65\beta + 634$ where ρ is density in kg/m^3 and β is shear velocity in meters/second. The top 2 km of the structure were constrained to have a shear velocity of 3025 m/s corresponding to the shear velocity of the calculation, and the Poisson's ratio and Birch's law given above ensured that the top two km had the same compressional velocity (5175 m/s) and density (2600 kg/m^3) as the calculation. The amplitudes were also inverted for Q structure, but that was less successful as the distances are short and amplitude variations due to earth structure that are not captured by the plane layered models dominate over attenuation variations. Figure 21 shows the earth models from surface wave inversion and the corresponding dispersion curve data fits. The low velocities at ~15 km depth for the INCN path are probably due to slight underdamping of the inversion.

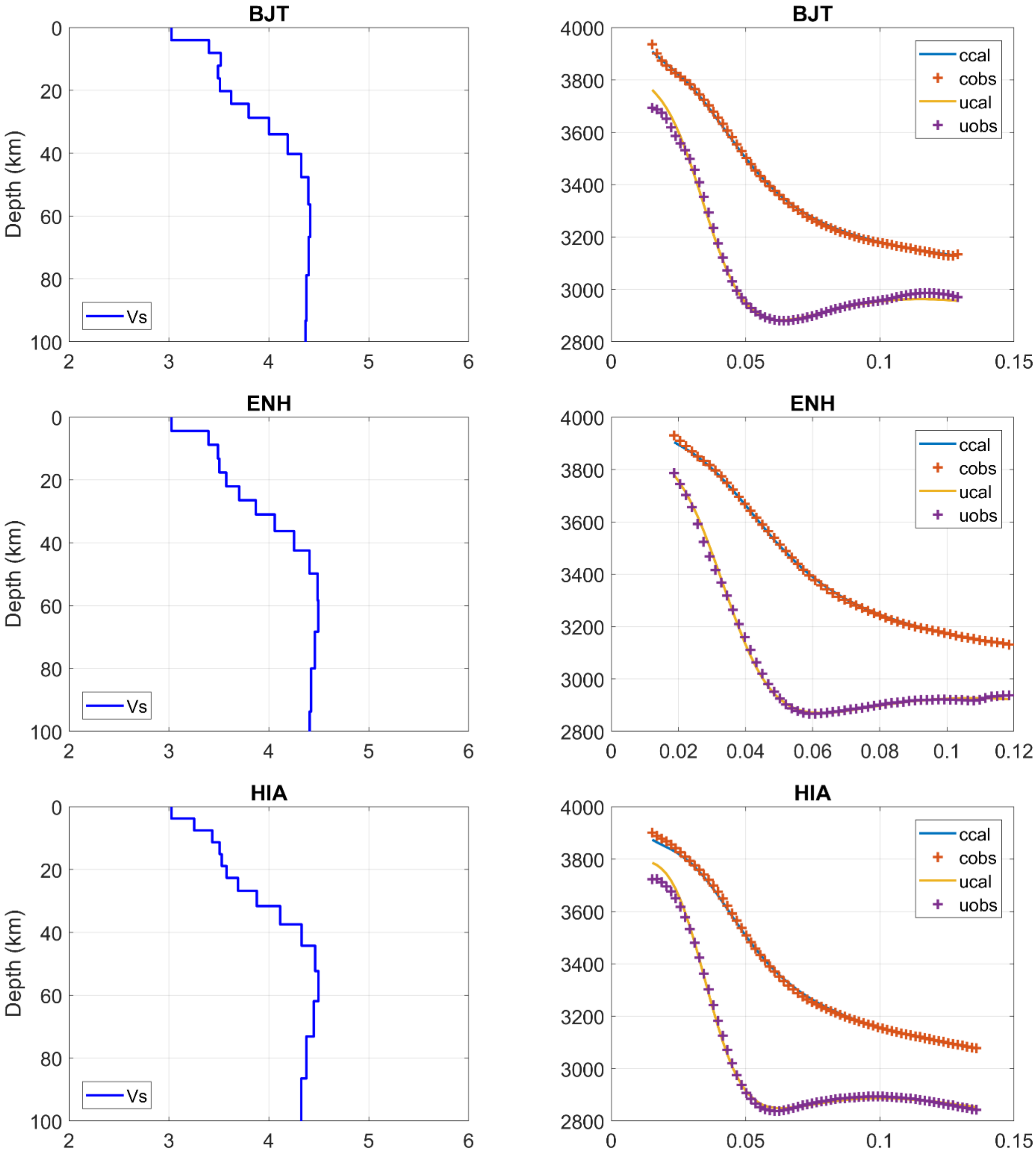
BJT
ENH
HIA
Depth (km)
0
20
40
60
80
100
2
3
4
5
6
Vs
4000
3800
3600
3400
3200
3000
2800
0
0.02
0.04
0.05
0.06
0.08
0.1
0.12
0.15
ccal
cobs
ucal
uobs

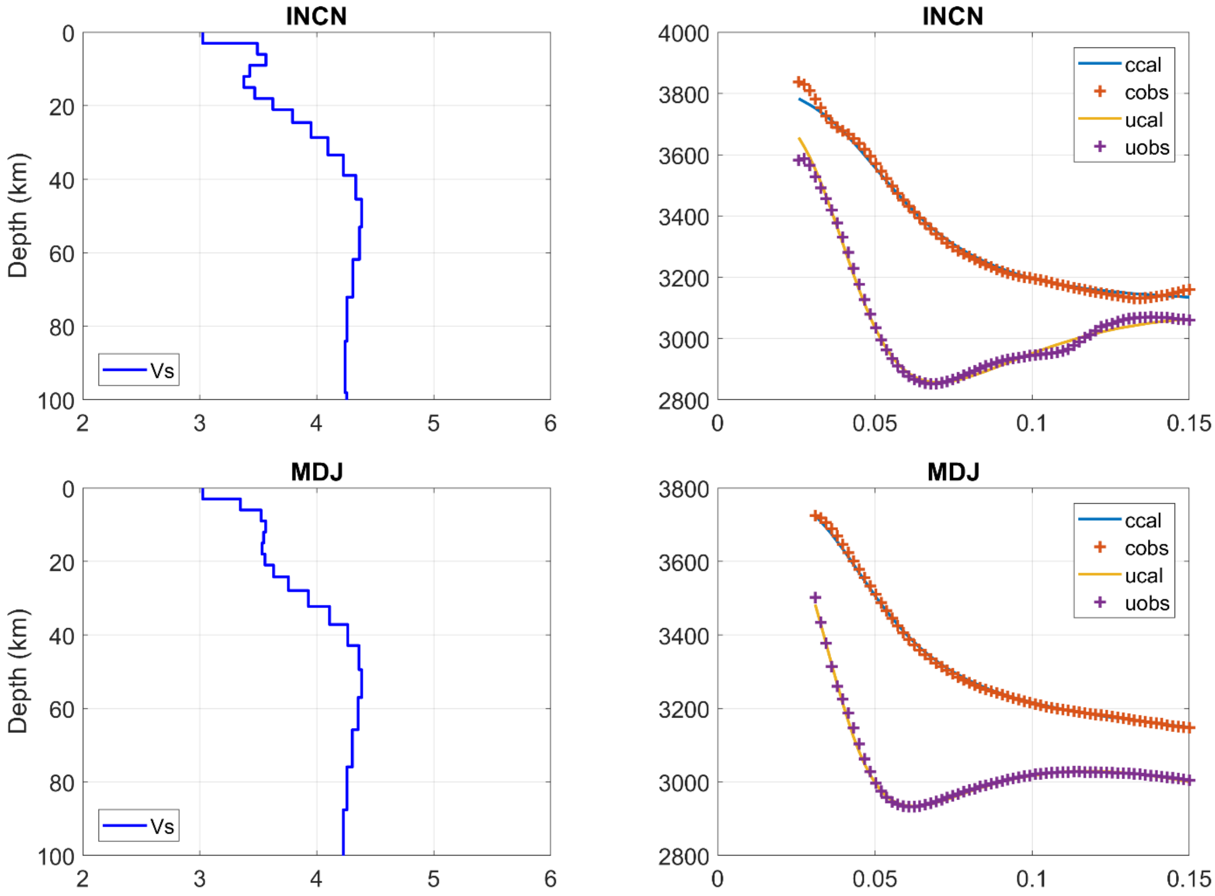

Figure 21. Earth models from surface wave inversion (left) and phase (ccal, cobs) and group velocity (ucal, uobs) data fits (right).

Figure 22 shows a comparison of point source fundamental mode surface waves calculated from the structures shown above with the data for each station, plotted as waveforms and spectra. All have been low pass filtered at 0.08 Hz. The waveforms and spectra generally agree quite well. The worst fit is at ENH which has an odd spectral shape (also noticeable in Figure 20) exhibiting some spectral enhancement at frequencies near 0.1 Hz and a deficiency at lower frequencies. Moments were allowed to vary in the calculations shown in this figure. The moments were 7.37x10^{16}, 6.14x10^{16}, 6.76x10^{16}, 8.29x10^{16}, 9.21x10^{16} Nt-m for MDJ, INCN, BJT, HIA and ENH, respectively. Mean value is 7.55x10^{16} Nt-m. As noted earlier, the surface waves for these events are quite large. Stevens and Murphy give the global scalar moment/yield relation as $\log M_0' = \log Y + 13.91$ which would predict a moment of 1.46x10^{16} for a 180 kt explosion, so the apparent moment of the 2017 explosion is 5 times larger than expected. The scalar moment is $M_0' = \left(3\beta^2/\alpha^2\right) M_0$ where M_0 is the isotropic moment of the explosion in the absence of tectonic release and α and β are the compressional and shear velocities at the source, respectively. The factor $3\beta^2/\alpha^2$ is very close to one in this case (1.025).

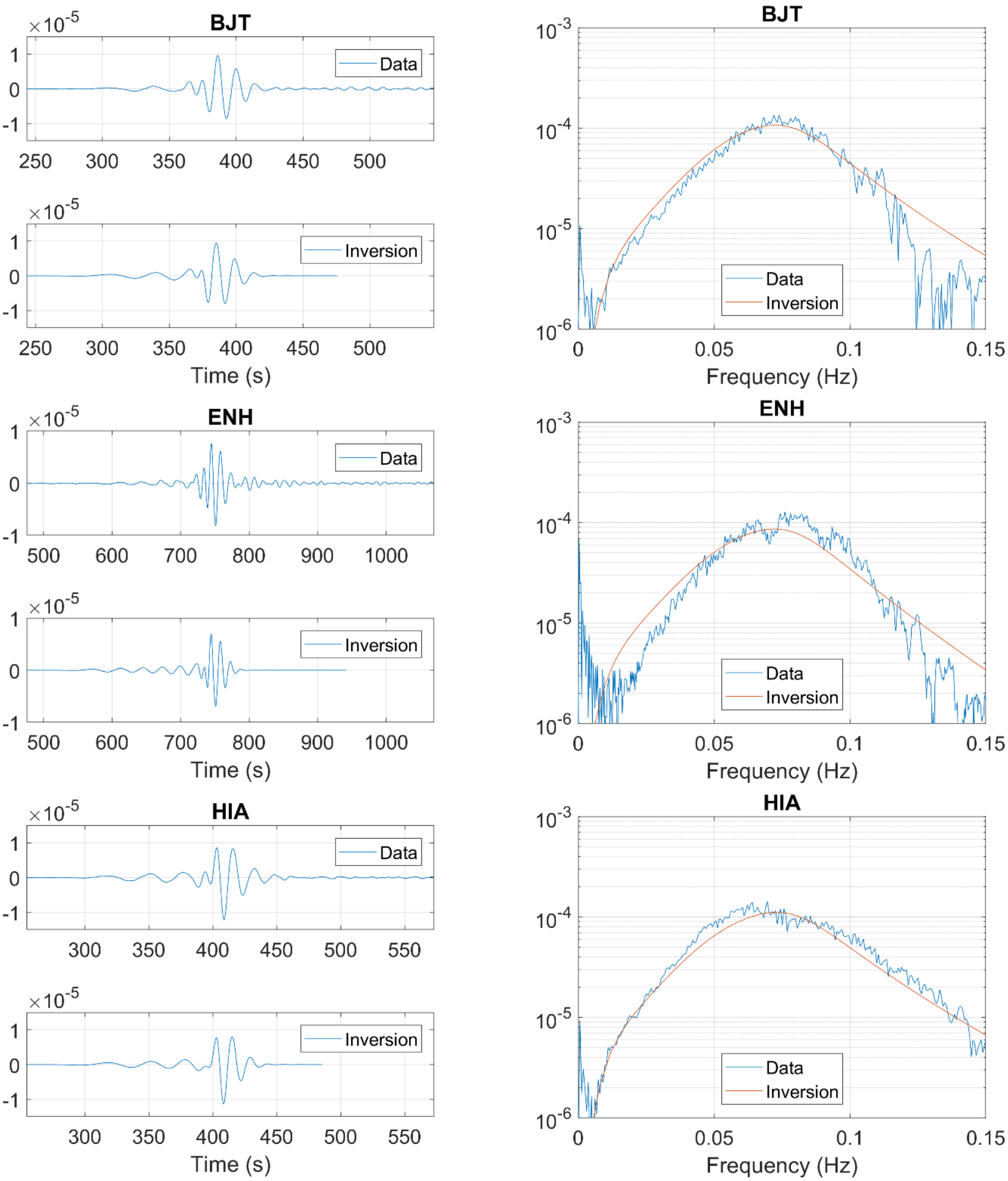
BJT
ENH
HIA
Data
Inversion
×10^-5
1
0
-1
250
300
350
400
450
500
500
600
700
800
900
1000
550
Time (s)
10^-3
10^-4
10^-5
10^-6
0
0.05
0.1
0.15
Frequency (Hz)

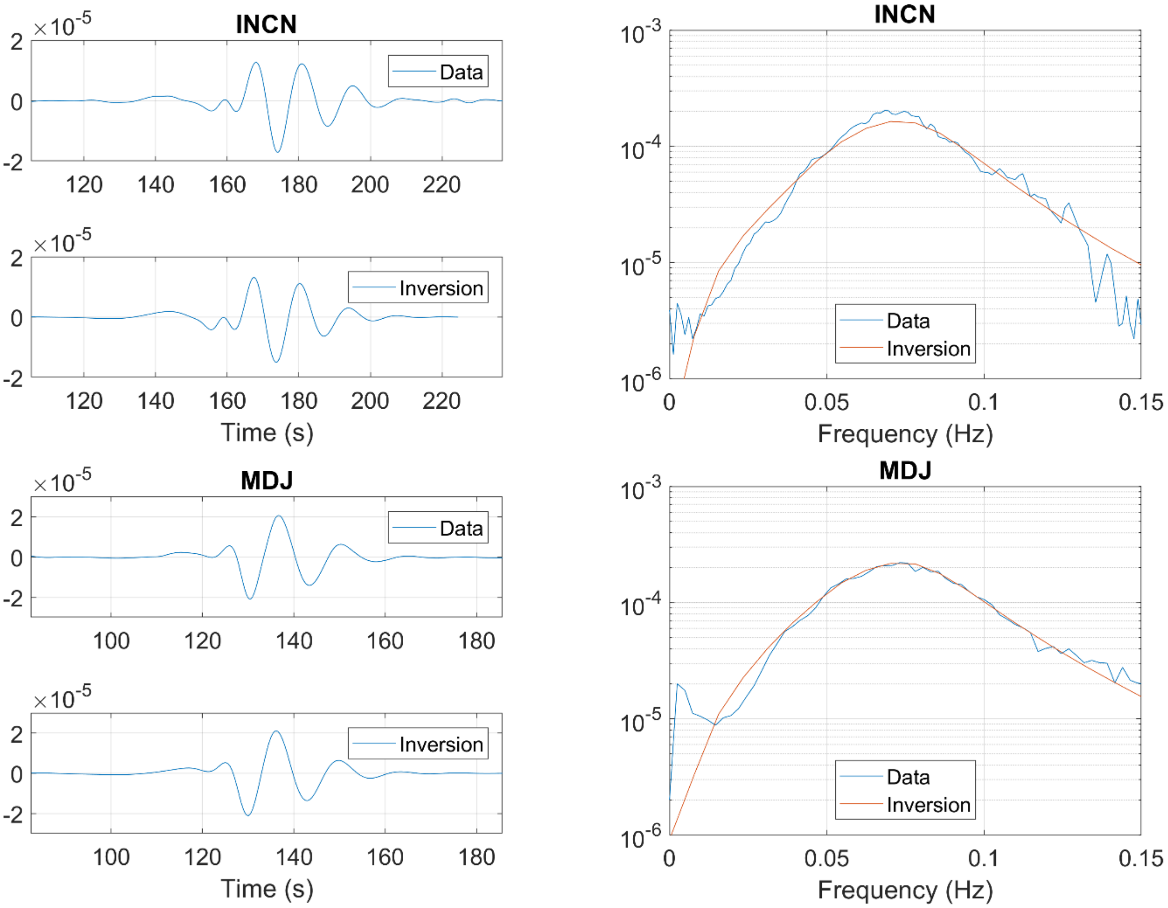

Figure 22. Waveform (left) and spectral (right) data fits comparing the fundamental mode surface wave velocity calculated from the inversion and the data from the 2017 explosion. Both data and calculations have been low pass filtered at 0.08 Hz.

4.4.2 Seismic waves at the 5 closest stations

We calculated both fundamental mode and full waveform Green's functions for the path structures to the closest 5 stations derived in the previous section. We then convolved these Green's functions with each of the CRAM3D calculations to generate waveforms at each station. We can then compare these results with the 1D point explosion plane layered waveforms calculated for the same paths.

Figure 23 shows fundamental mode surface waves for the two 2016 and the 2017 explosions at the 5 closest GSN stations. The top waveform in each figure is the data low pass filtered at 0.08 Hz, which removes most of the phases other than the fundamental mode surface wave. The bottom waveform is the fundamental mode surface wave calculated from the three CRAM3D calculations. The agreement is quite remarkable, particularly considering as noted earlier that the observed surface wave amplitudes are 5 times the global average. The CRAM3D calculations reproduce the surface wave data almost exactly.

Figure 24 shows spectra from the 2016 and 2017 explosions at the 5 closest GSN stations. Each plot contains five curves: 1) the observed waveform spectra, which is a fast Fourier transform (FFT) of the full time series from 20 km/s to 1 km/s, 2) full waveform 3D and 1D spectra and 3) fundamental mode surface wave 3D and 1D spectra. The 1D spectra are point spherical explosion source calculations at 700m depth in a flat, plane-layered structure, scaled by the moments inferred during surface wave inversion of $5.24\text{x}10^{15}$, $8.39\text{x}10^{15}$, and $7.55\text{x}10^{16}$ Nt-m, respectively. The 3D spectra are calculated directly from the CRAM3D calculations without any scaling. In the frequency band from 0.01 to 0.1 Hz, which is dominated by the fundamental mode surface wave, all spectra are in very good agreement, consistent with the surface wave results noted above.

In the 0.1 to 1 Hz frequency band, the 3D calculations have larger amplitudes than the 1D calculations, which is almost certainly due to the nonlinear interaction with the free surface, including spall, which is not present in the 1D calculations. The data have peaks that are suggestive of a similar effect, but the peak in the data occurs at lower frequency than the calculation.

Above 1 Hz, the calculations do not agree with the data very well. Waveforms arriving prior to the fundamental mode surface wave (cut off at 3.1 km/s) are shown in Figure 25, for the data, 1D and 3D full waveform calculations. Although phase arrival times are similar in each of the waveforms, amplitudes are quite different. This is most likely because the earth models derived from long period surface waves do not have the detail needed to reproduce the higher frequency amplitudes.

More interesting are the far-field P-waves shown in Figure 26. These are calculated from each CRAM3D calculation in the direction of each station and at the approximate takeoff angle (from down) for each. The takeoff angles used were 31 degrees for ENH and 40 degrees for each of the other stations. Azimuths were listed in Table 4. Amplitudes are inversely proportional to distance and are calculated for the surface distance to the station divided by the sine of the takeoff angle (this is just an implementation artifact and does not correspond to the actual distance travelled). Note the strong pP reflected phase in the 2016 calculations that is nearly absent in the 2017 calculation due to nonlinear interaction with the free surface.

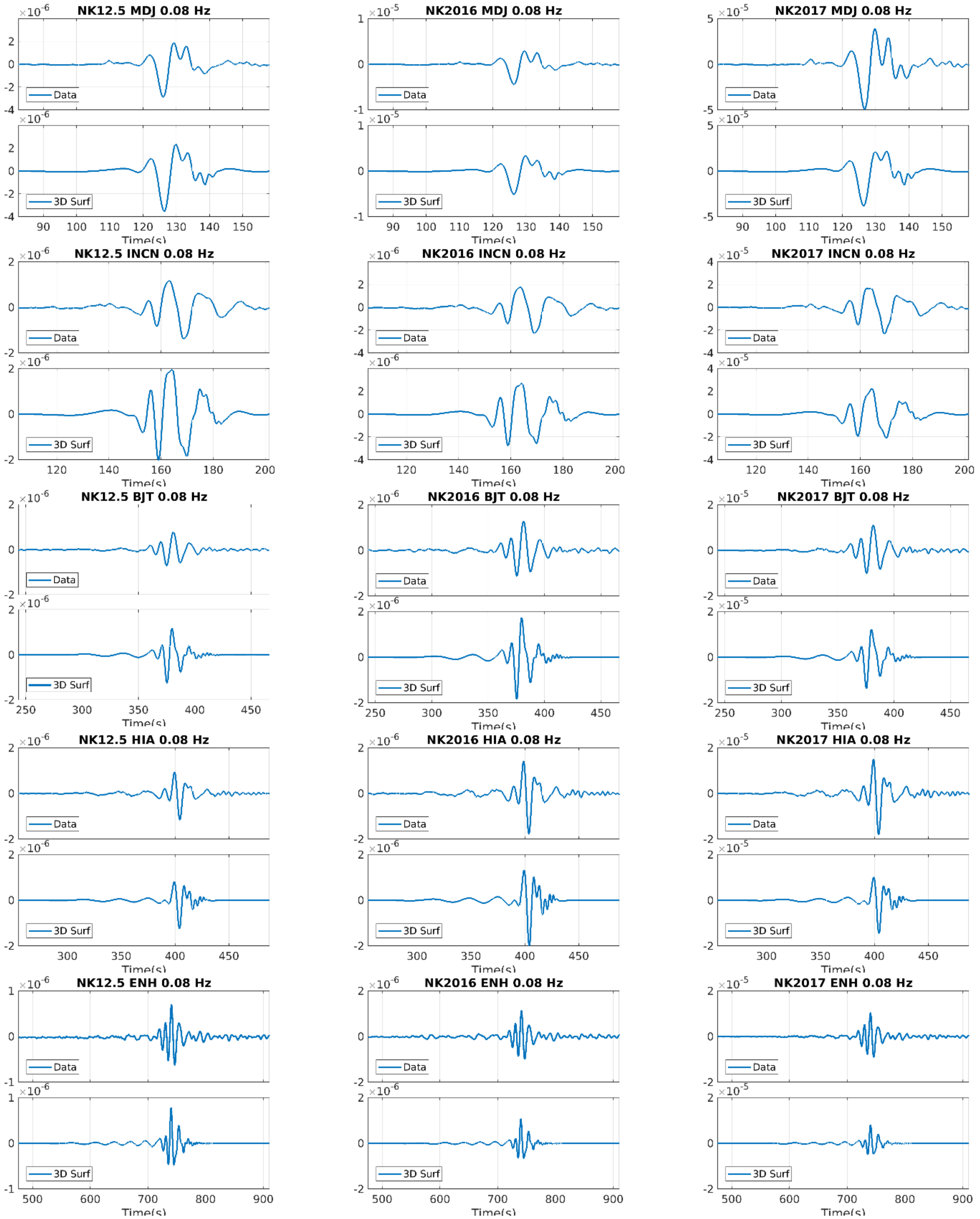

Figure 23. Calculated and observed fundamental mode waveforms. From left to right: NK2016A (12.5 kt), NK2016B (20 kt) and NK2017 (180 kt). From top to bottom, stations MDJ, INCN, BJT, HIA and ENH. Top waveform in each is data, bottom is the surface wave from the 3D calculation. All are lowpass filtered at 0.08 Hz.

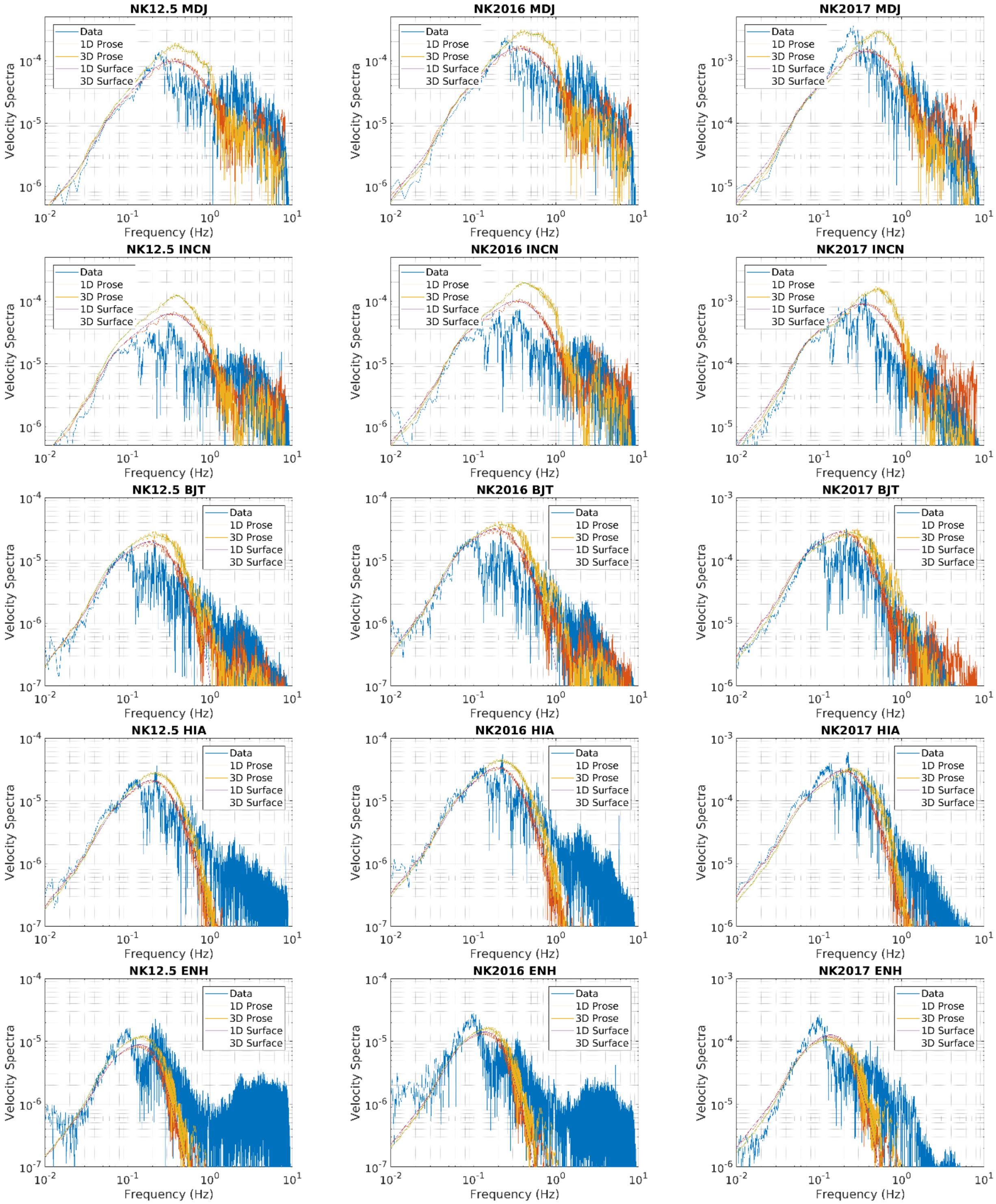

Figure 24. Spectra from waveform calculations. From left to right: NK2016A (12.5 kt), NK2016B (20 kt) and NK2017 (180 kt). From top to bottom, stations MDJ, INCN, BJT, HIA and ENH. Each plot contains the observed waveform spectra, full waveform 3D and 1D spectra and fundamental mode surface wave 3D and 1D spectra.

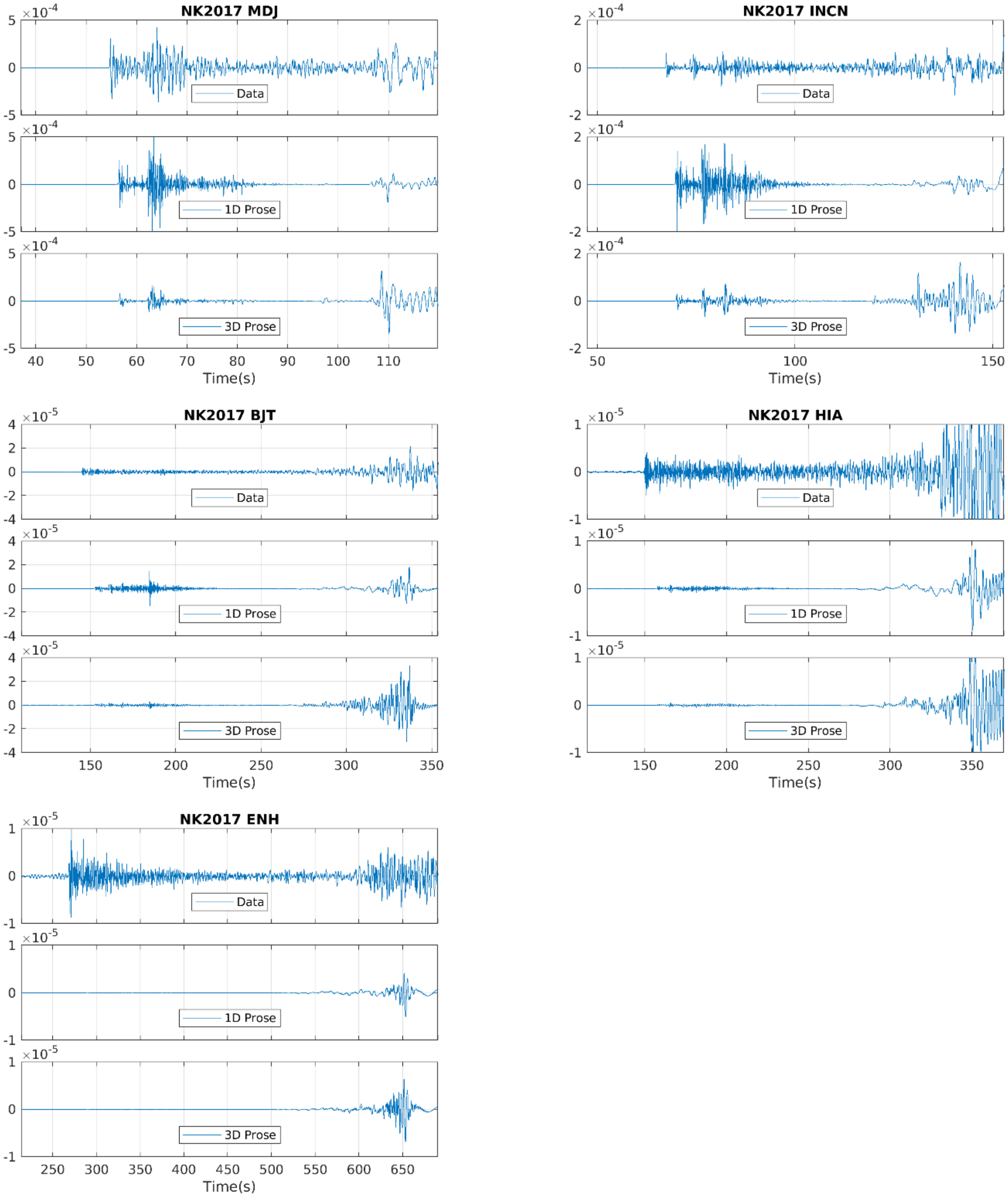

Figure 25. Data (top), 1D (middle) full waveform and 3D (bottom) full waveforms generated from the NK2017 CRAM3D runs at five stations.

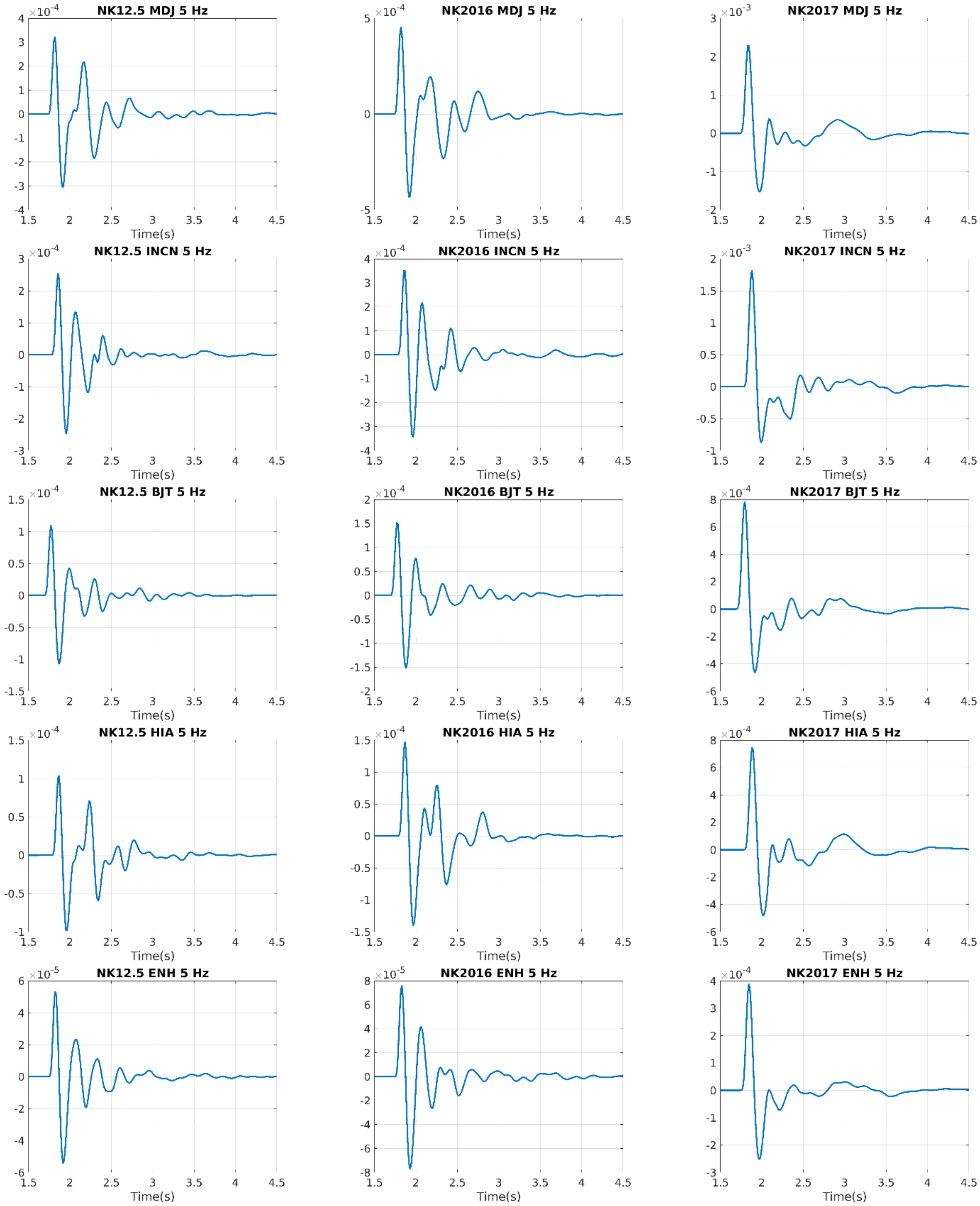

Figure 26. Far field P-waves 1000 km below the source at the azimuth and takeoff angle of each of the 5 closest GSN stations. From left to right: NK2016A (12.5 kt), NK2016B (20 kt) and NK2017 (180 kt). From top to bottom, stations MDJ, INCN, BJT, HIA and ENH. All are lowpass filtered at 5 Hz.

The pP reduction effect is also apparent in the data. Figure 27 shows the data from the 2017 and 2016B explosions recorded at the two closest stations MDJ and INCN. The reflected pP phase is clearly reduced in amplitude at both stations for the 2017 explosion relative to 2016B.

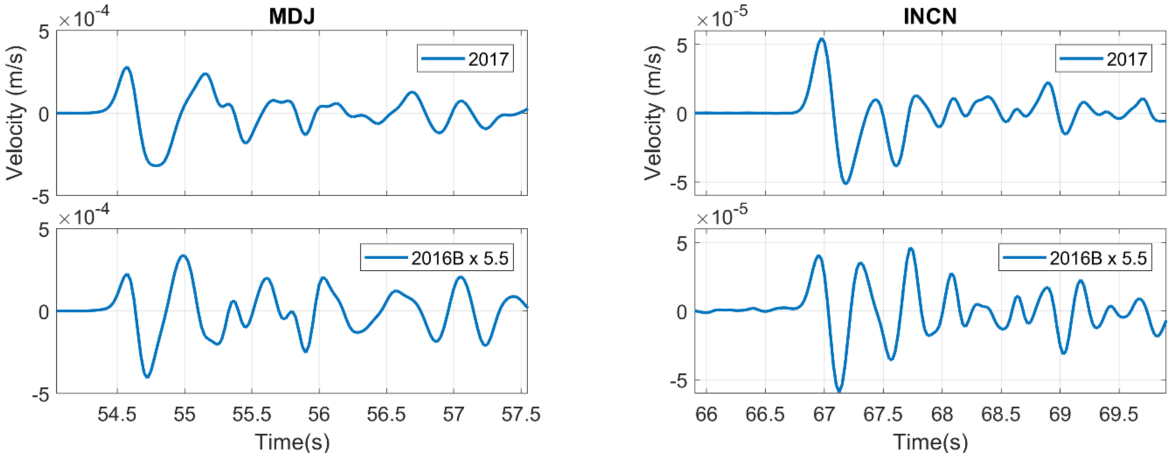

Figure 27. The pP phase is smaller in the 2017 explosion that in the 2016B explosion. The top figure in each plot above is the first arriving P-wave from the 2016 explosion and bottom is from 2016B. Left waveforms are from MDJ and right from INCN. All lowpass filtered at 5 Hz.

4.4.3 Comparison with Weston Geophysical Results

Yoo and Reiter (2017)[2], from Weston Geophysical Corporation, presented an analysis of body waves from the 2006-2016 North Korean explosions. In the following two figures we have plotted data from four events and the equivalent four calculations, using the same color scheme for ease of comparison. Figure 28 shows calculated P-waves to the North and South for 4 events and Figure 29 shows the corresponding P-wave data for MDJ and INCN. As in the Yoo and Reiter study and in the data, we find a substantial increase in the pP phase to the north, caused by reflection off of a (nearly) optimally placed mountain slope. The 2017 event is different, as the nonlinear interaction with the free surface reduces the pP phase, which is observable in both the data and the calculations.

---

[2] Yoo, S. and D. Reiter, “The Influence of Topography on Regional P-Wave Observations from the North Korean Underground Nuclear Tests,” presentation at April 2017 Seismological Society of America meeting.

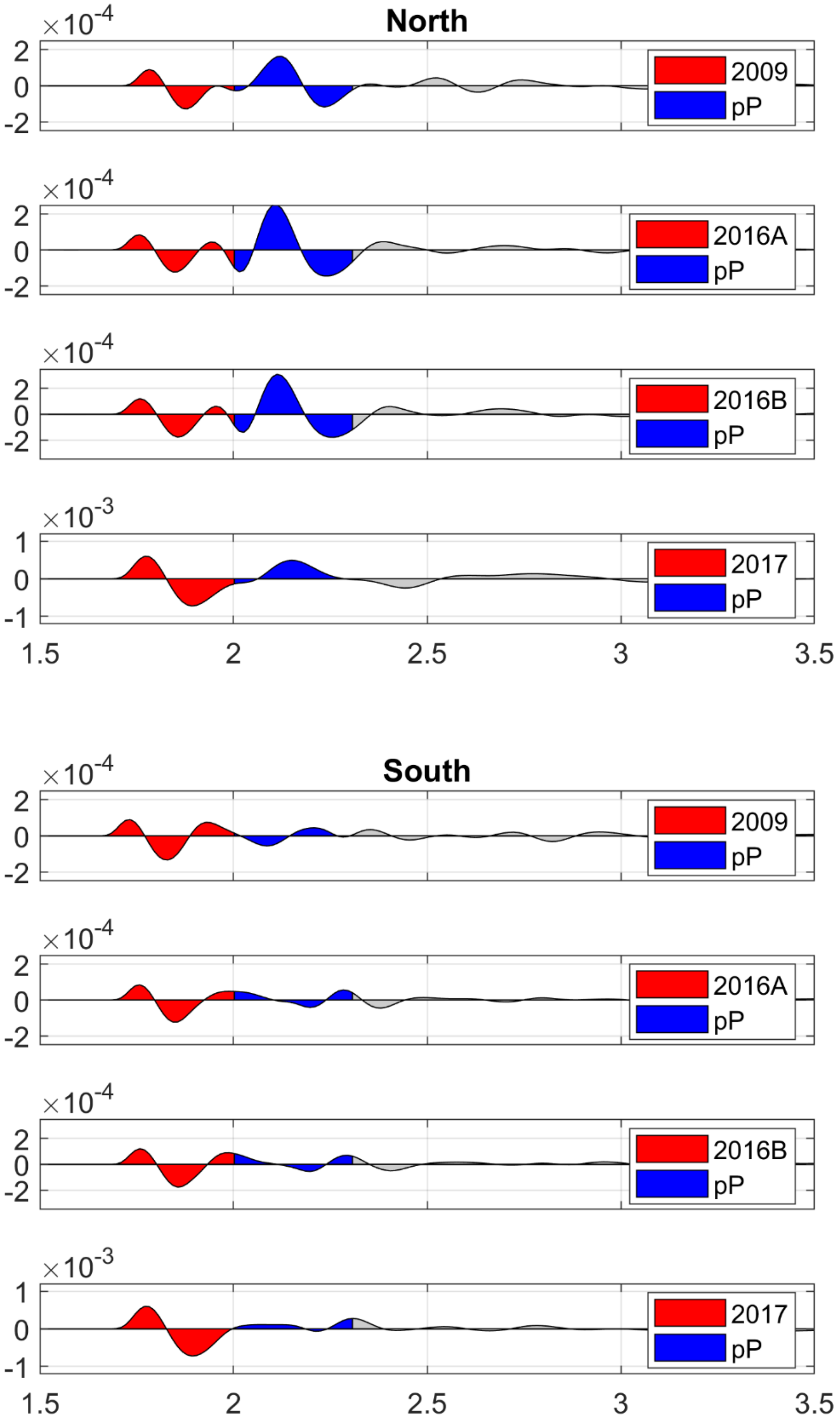

Figure 28. Calculated P-waves to the north (top) and south (bottom) for four events (calculations NK_540, NK2016A, NK2016B and NK2017). Bandpass filtered 0.5 to 5 Hz.

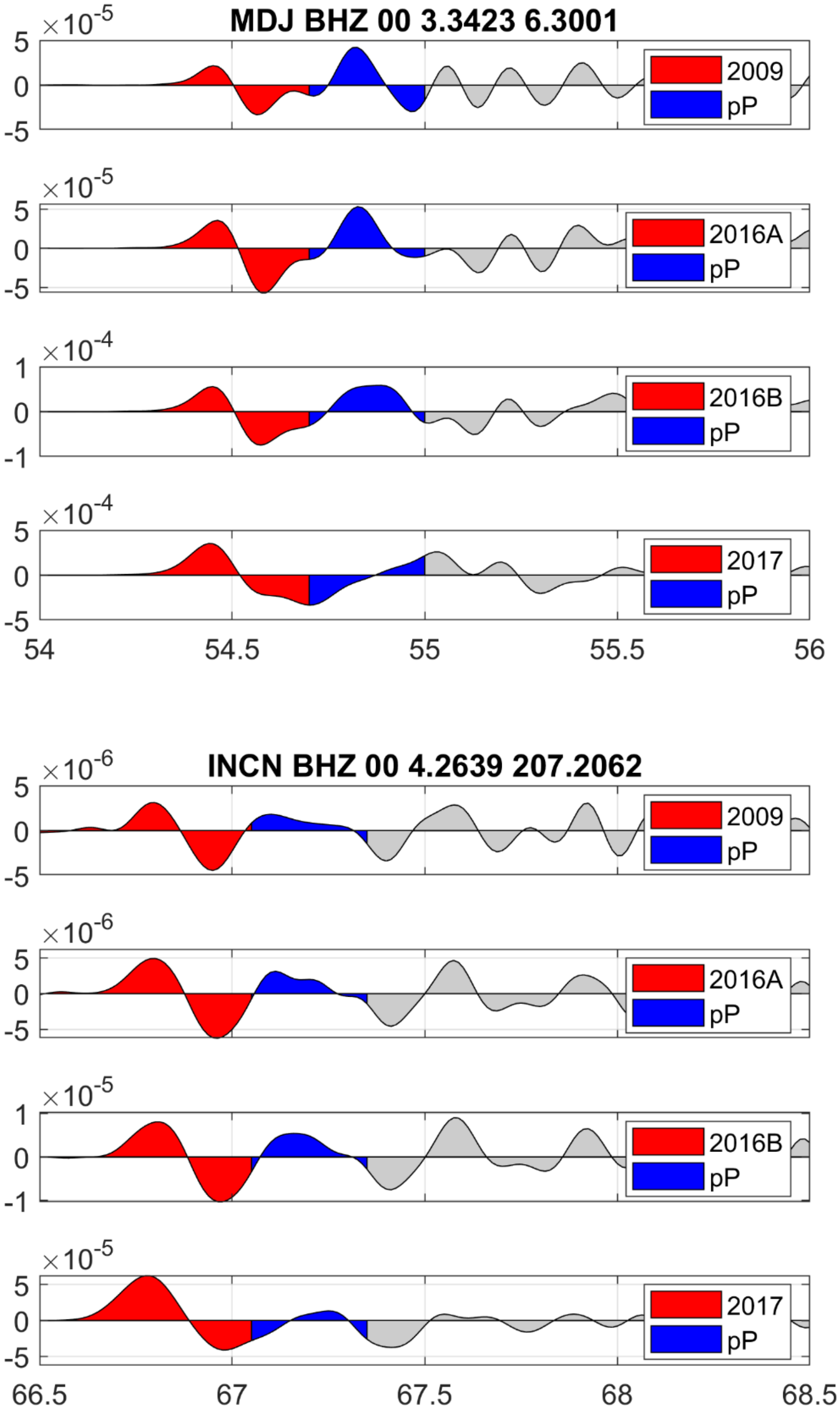

Figure 29. P-wave data at MDJ to the north (top) and INCN to the south (bottom) for NK tests 2009, 2016A, 2016B and 2017. Bandpass filtered 0.5 to 5 Hz.

4.4.4 Tectonic Release

We performed two additional calculations with tectonic strain release. Earlier studies (Murphy et al, 2013; Stevens and Thompson, 2015; Stevens et al, 2017a) have shown that tensile tectonic stresses increase surface wave amplitudes, while compressive stresses decrease and in some cases invert them. The North Korea test site is in a region of north-south extension (Murphy et al, 2013), which would tend to increase surface waves in that direction. The stress state in the east-west direction is unknown. The earlier studies all used a flat surface without topography. While the equilibrium stress state is not unique, we usually make the assumption that the horizontal stresses are released completely where there is topography. This gives a very stable equilibrium solution and has an effect similar to tensile tectonic release. That is, the effect of topography is to reduce the horizontal stresses around the explosion. However, tectonic stresses cannot reduce the horizontal stresses within the mountain any further, so they only apply beneath the mountain.

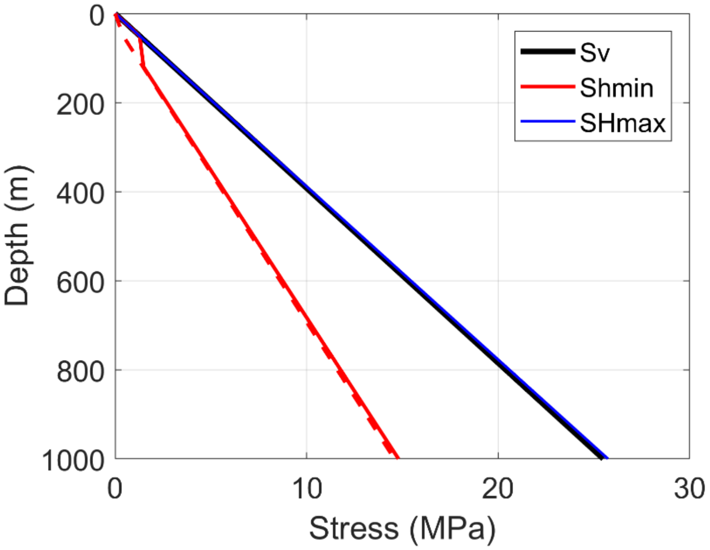

Figure 30. Prestress used in the NK2017TR calculation. Dashed line shows limiting prestress with a coefficient of friction of 0.6.

Figure 30 shows the stress state in the region outside the mountain. Shmin is in the northerly direction (X direction in the CRAM3D calculation). Below 100 meters the tectonic stress is tensile (horizontal stress in the X direction is reduced), consistent with equilibrium with frictional sliding with a coefficient of friction of 0.6. We use no prestress for the upper 50 meters, and then an increase to frictional equilibrium in the next 50 meters. Under the mountain, we use the same prestress, applied as a reduction in horizontal stress in the X direction, at a constant elevation throughout the grid. No prestress is applied within the mountain. In the Y direction, we apply a small (1%) compressive prestress. The initial pressure and change in X stress state are shown in Figure 31.

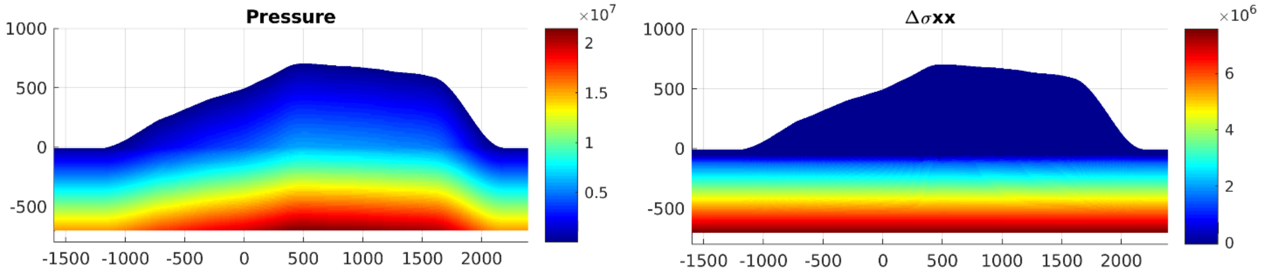

Figure 31. Left: initial pressure state with prestress. Right: Change in initial horizontal stress state due to prestress. Note that pressure is positive in compression and stress is positive in extension.

Because the change in stress state due to prestress is primarily below the explosion, the effect on seismic waves is reduced compared to earlier calculations without topography, however it still has some effect, as shown in Figure 32. Surface waves are increased in amplitude noticeably at MDJ and INCN, and slightly at HIA. The calculated surface waves fit the data remarkably well with or without tectonic strain release.

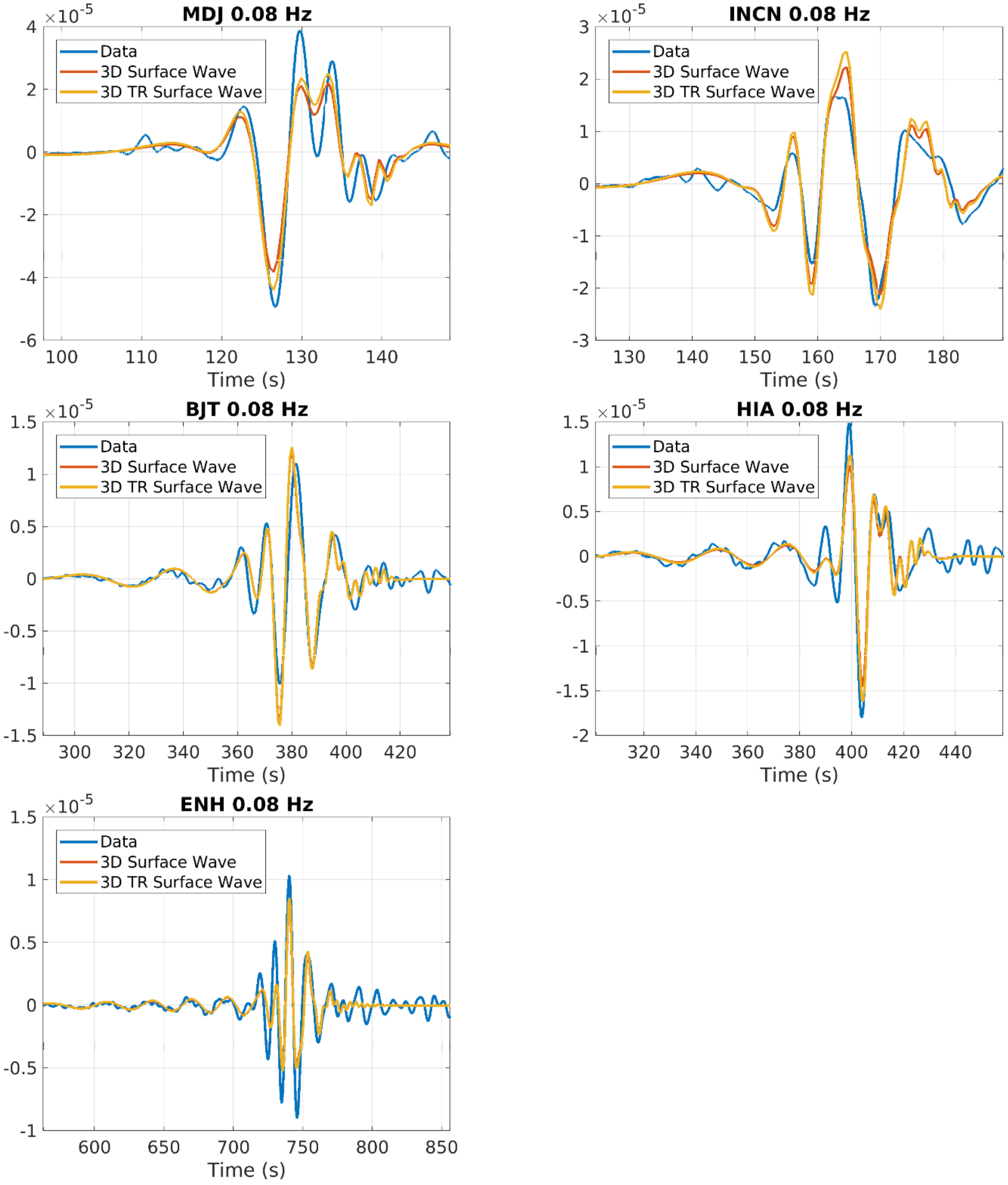

Figure 32. Calculated surface waves with and without tectonic release. With tectonic release (TR), surface waves are larger in the direction of extension, at MDJ and INCN.

We did one final calculation with compressive tectonic stresses. The prestress field is shown in Figure 33. Compressive prestress close to the limiting stress for a coefficient of 0.6 was applied in the N-S direction, and a small compressive stress was applied in the E-W direction. As with the tensile prestress calculation, the prestress was only applied beneath the mountain and the mountain remained in a state where horizontal prestress was released by the sides of the mountain.

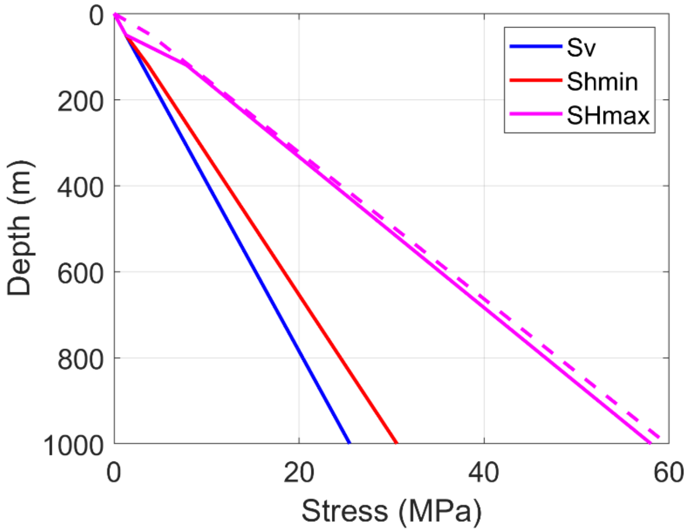

Figure 33. Prestress used in the NK2017TH calculation with compressive prestress. Dashed line shows limiting prestress with a coefficient of friction of 0.6.

As expected, surface wave amplitudes were reduced by the compressive prestress, but only by a small amount for a source at the base of the mountain (Figure 34). Ms from calculated surface waves are close to the observed Ms of 5.2 (See Figure 6 and Table 1).

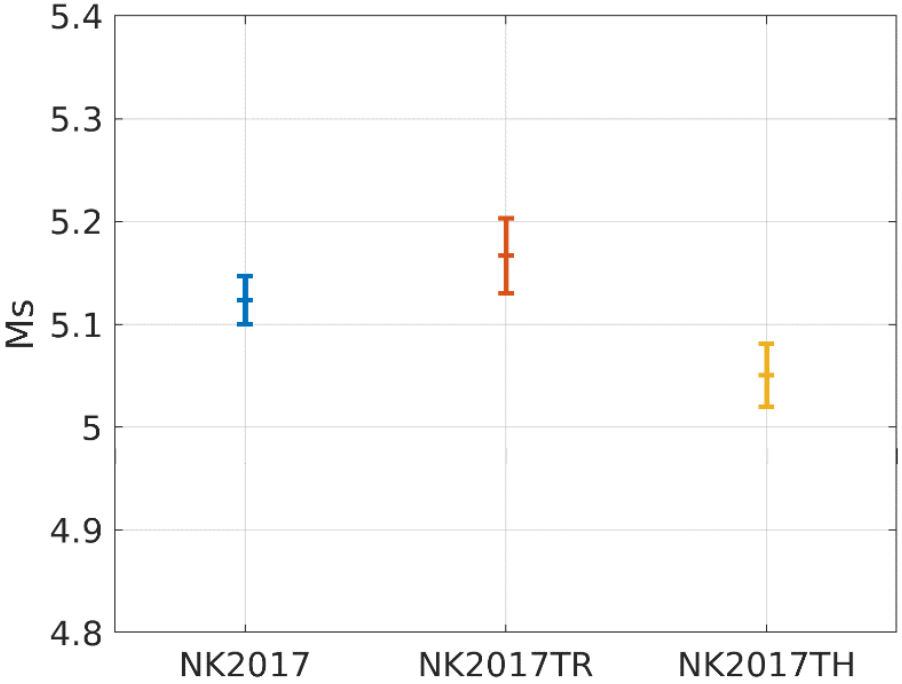

Figure 34. Mean±standard deviation of Ms from surface waves calculated at the locations of the five closest stations without tectonic release (NK2017), with tensile tectonic release (NK2017TR) and with compressive tectonic release (NK2017TH).

4.4.5 Ms from all calculations and an explanation of the North Korean Ms anomaly

Ms was calculated for all waveforms derived using both the North Korean earth structure at a common distance of 2000 km and 8 uniformly spaced azimuths, and the specific structures to each of the 5 closest stations. Ms was calculated using Russell's procedure for evaluating Ms at 20 seconds, and these are listed in Table 5. The average 5 station Ms values are about 0.08 magnitude units higher than the uniformly distributed 8 station Ms values.

Table 5. Ms measured from calculated surface waves

Calculation	Yield (kt)	Depth (m)	Ms (5 Station)	Ms (8 Station)
NK2017	180	730	5.124±0.023	5.037±0.007
NK2017TR	180	730	5.167±0.037	5.078±0.028
NK2017TH	180	730	5.051±0.031	4.966±0.018
NK2016B	20	730	4.209±0.022	4.120±0.007
NK2016A	12.5	730	4.049±0.040	3.955±0.025
NK-100	12.5	100	3.333±0.072	3.244±0.054
NK-200	12.5	200	3.652±0.045	3.561±0.039
NK-540	12.5	540	3.851±0.028	3.762±0.019
NK-800	12.5	800	3.694±0.026	3.605±0.014

Ms measured from the surface waves derived from the calculations at four depths (NK-100 to 800) at the 8 azimuths in the North Korean structure are shown in Figure 35. There are several interesting observations to be made from this plot. First, there is a maximum in the surface wave magnitude at the 540 meter depth. There are two reasons for this: 1) at the 800 meter depth, the pressure is higher and that reduces the surface wave amplitudes; 2) at 100 and 200 meters, the horizontal displacement caused by the explosion moves the sides of the mountain into the air causing less of the surface wave to propagate. This effect was discussed by Stevens et al (1993). The long period surface waves from a shallow explosion are generated almost entirely by the horizontal displacement outside the source, so when the displacement is relieved by the side of the mountain, long period surface waves are reduced. One other effect that increases the size of the surface wave at 540 meters is that both the pressure and horizontal stress under a mountain are lower than the pressure and horizontal stress at the same depth in a flat-layered structure. In addition to the amplitude reduction within the mountain, there is also more azimuthal variability, especially at the 100 meter depth, due to asymmetry caused by differences in the distance to the slope in different directions.

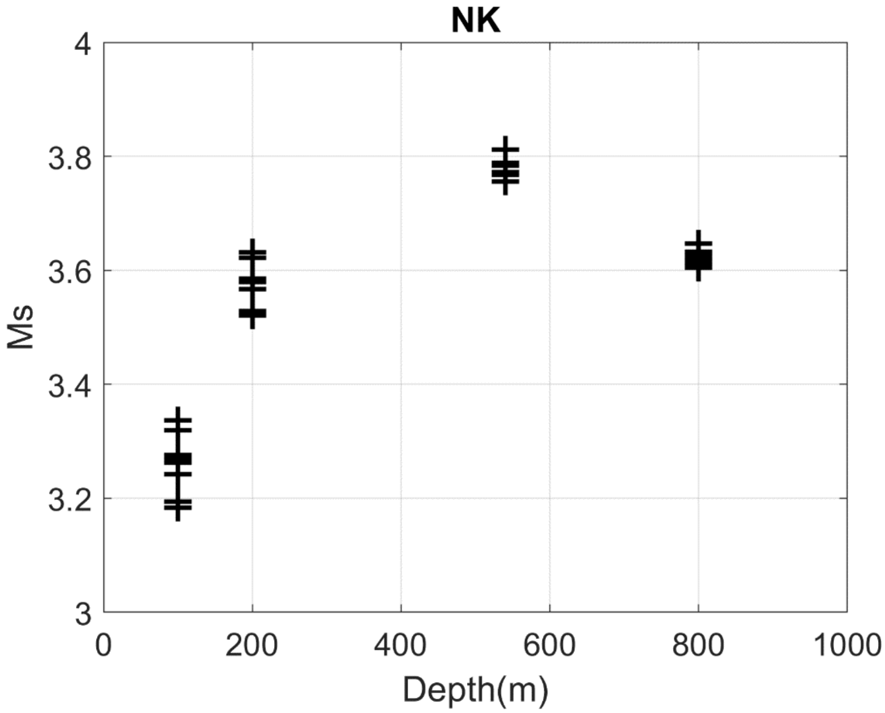

Figure 35. Long period surface wave magnitudes calculated from the four CRAM3D calculations at depths from 100-800 meters. These are 20 second magnitudes measured from fundamental mode surface waves low-pass filtered at 0.1 Hz. Each point corresponds to a different azimuth.

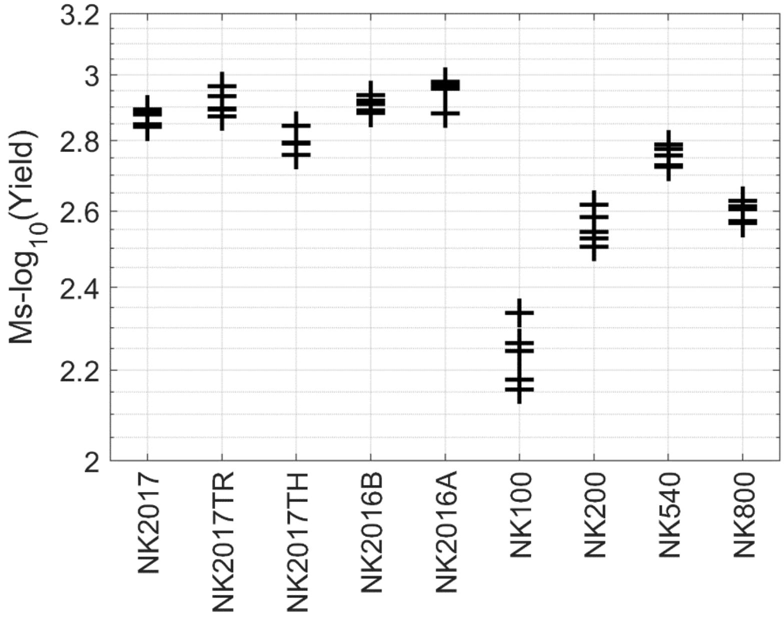

Figure 36. Ms-log(yield) for all calculations using the paths to the five closest stations.

Figure 36 shows Ms-log(yield) for all calculations performed, using the paths to the 5 closest stations. The global average value for Ms-log(yield) from all nuclear explosions is 2.1 (Stevens and Murphy, 2001), so these values are consistent with the high Ms observed for the North Korean explosions.

Figure 37 compares the observed and calculated Ms for the 2016 and 2017 events. Agreement is very good.

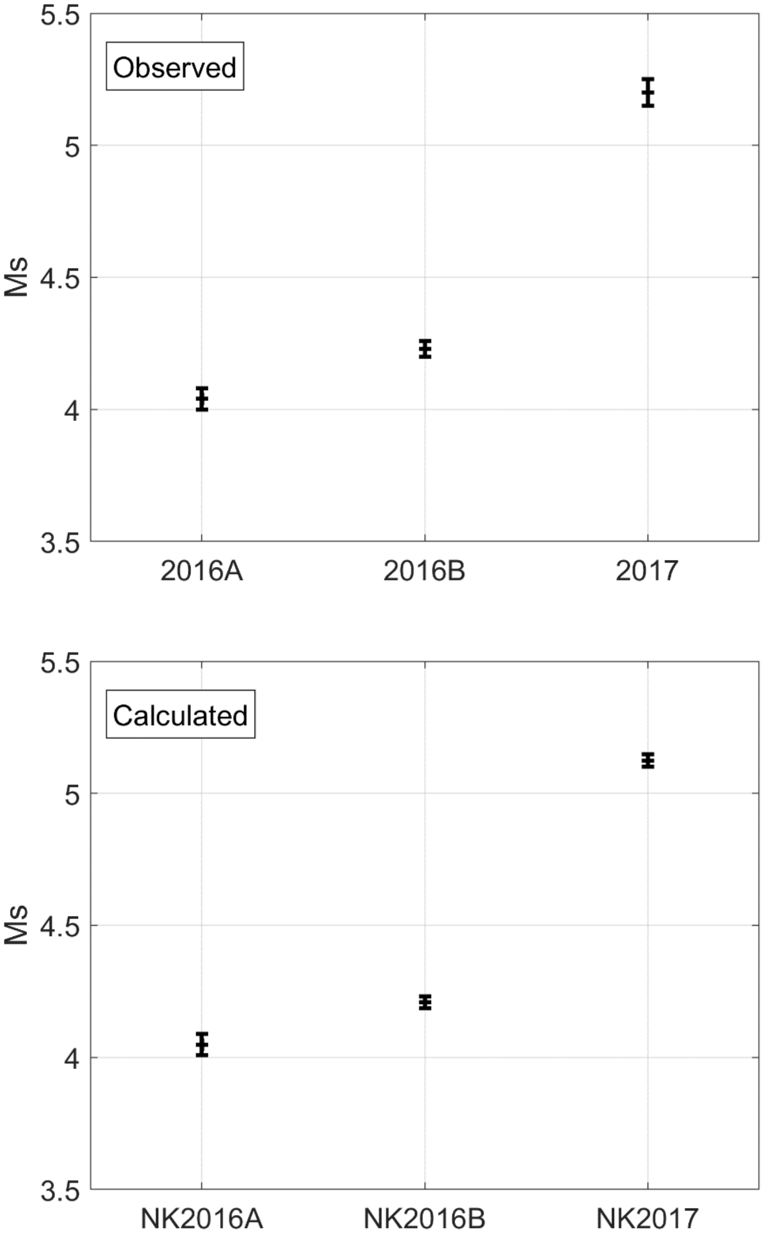

Figure 37. Top: Ms and standard deviation measured from the observed surface waves at the five closest stations for the 2016 and 2017 explosions. Bottom: Ms and standard deviation measured from the calculated surface waves at the five closest stations for the 2016 and 2017 explosions.

Given the excellent agreement between observed and calculated surface waves from the North Korean explosions, why are they so anomalous compared to the global data set? As noted above, there is an amplification effect for an explosion at the base of a mountain, but this only explains part of the difference. To understand where the rest of the difference likely comes from, we need to look at Ms vs. depth for explosions in a flat structure. Stevens et al (2017) did a series of axisymmetric finite difference calculations covering a range of depths from 150 to 1000 meters for a 12.5 kiloton explosion using the same material model used in our 3D North Korean calculations. They did the calculations with no prestress and with compressive and tensile prestress, and then calculated surface waves and measured Ms for all of the calculations. The results are shown in Figure 38.

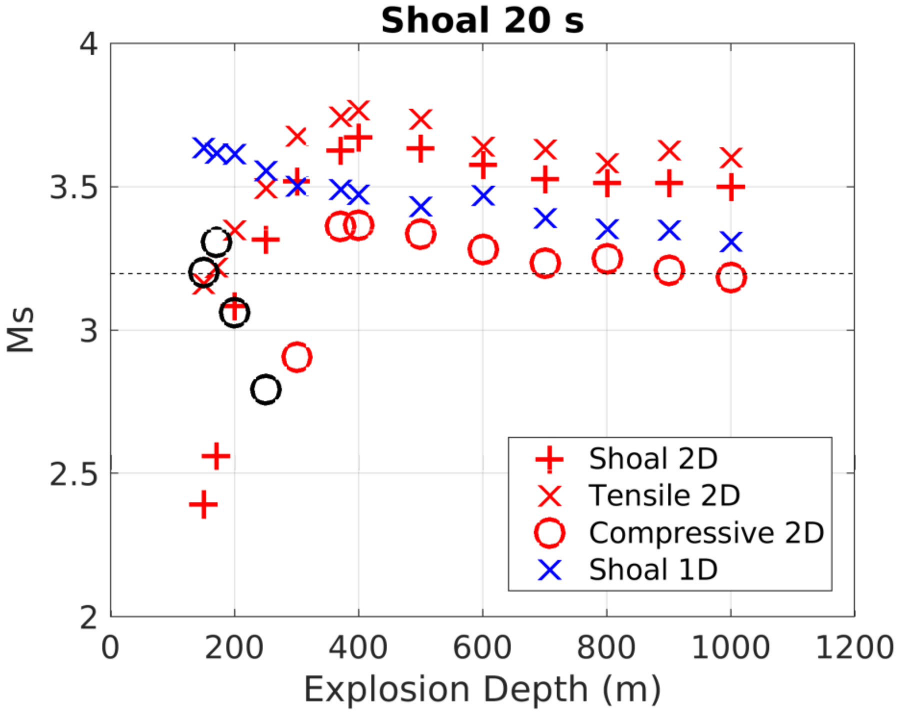

Figure 38. Ms vs. depth from axisymmetric calculations in a flat layered structure from Stevens et al (2017). Blue crosses are for a point explosion source calculated using a 1D spherically symmetric finite difference code. The dashed line is the expected Ms from the global data set (Stevens and Murphy, 2001). Black symbols indicate phase reversals.

There are several observations to be made from this plot:

1. The spherically symmetric calculations show the effect of changes in pressure with depth, without the surface nonlinear interaction. There is a gradual decrease in Ms with increasing depth.
2. The free surface interaction strongly affects the surface waves, decreasing Ms substantially at shallow depths as the nonlinear interaction with the free surface decreases. This is similar to the effect described by Patton and Taylor (2008) and Patton (2016). There is a more surprising increase in Ms relative to the 1D calculations for deeper events that is caused by increased horizontal motion near the spall depth.
3. Tectonic release strongly affect the surface waves, particularly compressive tectonic release, which reduces Ms by 0.3 magnitude units or more. Compressive tectonic release

combined with the free surface interaction causes phase-reversed Rayleigh waves for depths less than about 275 meters (scaled depth 120 meters/kt$^{1/3}$).

Both explosion depths shallow enough to have a strong free-surface interaction and compressive tectonic stresses are common conditions for the historical database of nuclear tests, and even with tensile tectonic stresses, for shallower events the free surface effect is stronger, causing a reduction in Ms. This causes a negative bias in the historical Ms data set.

The presence of strong topography such as the North Korean test site changes this in three ways:

1. Stress release by the sides of the mountain cause both the pressure and horizontal stresses to be reduced at the base of the mountain relative to an explosion at the same depth in a flat-layered structure, causing an amplification of the surface wave.
2. Since tectonic stresses in general will not extend up into the mountain (because the sides of the mountain would release them), the effect of tectonic stresses on the surface waves is reduced relative to a flat-layered structure.
3. Because the nonlinear effects occur near the top of the mountain, their effect on surface waves are reduced for the same reason that surface waves are reduced for an explosion inside the mountain. That is, the horizontal deformation caused by the nonlinear interaction with the free surface displaces the sides of the mountain instead of generating a long period surface wave.

Figure 39 shows a comparison of scaled Ms vs. scaled yield for four hard rock sites. Note the similarity between the Balapan test site and the axisymmetric calculations, with a distinct decrease with decreasing scaled depth and Ms comparable to the Ms calculated for a region with tectonic compression. Degelen similarly shows low values at shallow depths, but more of a range, with the largest scaled Ms approaching that of the North Korean events. This is very likely due to the effects of topography at the Degelen test site, which is in a larger, broader mountain than North Korea, so it appears that the Degelen Ms values range from the low values expected for an explosion in a flat-layered structure to the high values expected in a region with strong topography.

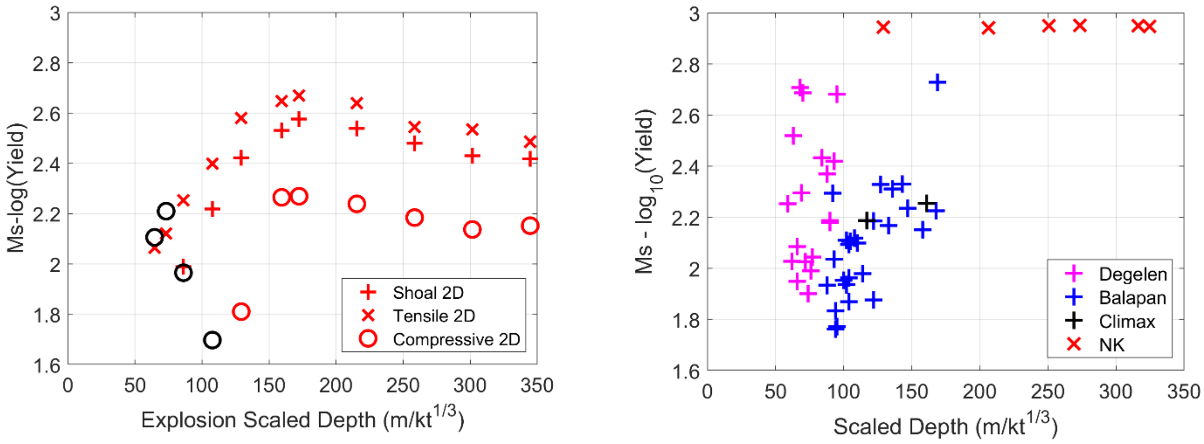

Figure 39. Left: Ms-Log(Yield) vs. scaled depth for axisymmetric calculations. Black circles indicate phase reversals. Right: Ms-Log(Yield) vs. scaled depth for North Korean, Degelen, Balapan and Climax Stock (NTS) hard rock explosions. Data is from Patton (2016).

The effects of the free surface and topography are summarized in Figure 40. As noted before, long period surface wave generation is controlled by the subsurface horizontal displacement. A subsurface explosion, or an explosion near the base of the mountain, causes an outward horizontal displacement, generating a surface wave, however as the explosion moves up into the mountain, the explosion moves the side of the mountain, with a reduction in subsurface displacement. The explosion causes substantial nonlinear deformation between the explosion and the free surface. In a flat structure, this nonlinear deformation causes an inward motion, reducing the surface wave amplitude. That is, as nonlinear deformation moves the material above the explosion upward, material moves in from the sides. In a medium with strong topography, however, the nonlinear deformation occurs inside the mountain, concentrated near the surface. Horizontal stresses are reduced by the sides of the mountain, so there is little if any inward motion, and motion in either direction has little effect on the surface waves because the motion affects the sides of the mountain instead of subsurface displacement.

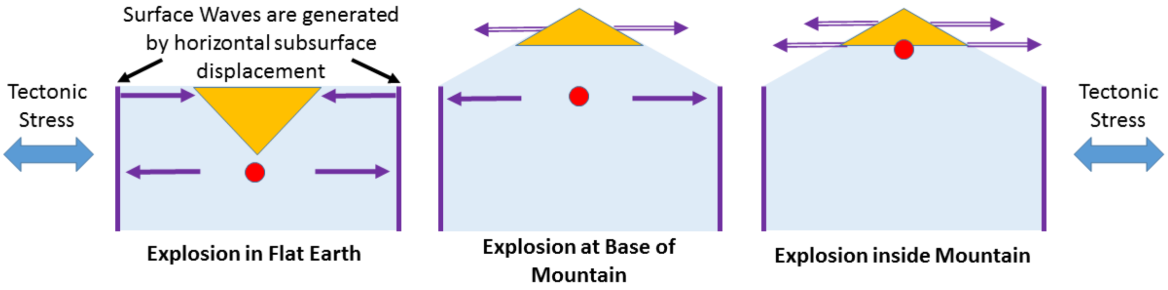

Figure 40. Long period surface wave amplitudes depend on the subsurface horizontal displacement: the solid vertical lines on the sides of each figure. In a flat earth, the explosion (red circle) generates an outward displacement on this surface, but the nonlinear free surface effects (gold region) generate an inward motion, reducing the surface wave from the explosion. When the explosion is at the base of the mountain, it still causes a horizontal displacement in the earth, but the nonlinear free surface effects just move the sides of the mountain and have little effect on surface wave generation. When the explosion is inside the mountain, it moves the sides of the mountain instead of the subsurface, so surface wave generation is reduced.

4.4.6 Far-field body wave depth dependence with topography

P-wave amplitudes low-pass filtered at 5 Hz are shown in Figure 41. These are measured from downgoing P-waves leaving the source at a 20 degree takeoff angle from vertical into an infinite medium with the same material properties as the source region, at a distance of 2924 (1000/sin(20)) km. This allows us to see a clean P-wave signal that includes all surface reflections but is undisturbed by the structure along the propagation path. There is much less variability and depth dependence in the P-wave than in the surface wave, however there are high amplitude P-waves in the direction to the north of the test site. This is a focusing effect caused by the slope above the explosion (Figure 42).

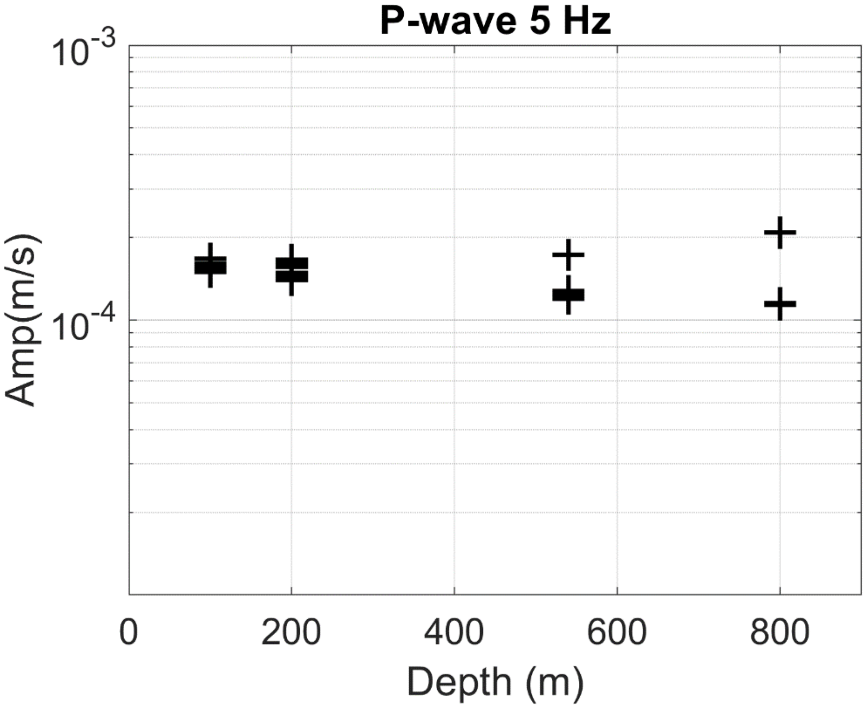

Figure 41. P-wave amplitudes calculated from the four CRAM3D calculations at depths from 100-800 meters, all low-pass filtered at 5 Hz. The high amplitudes at 540 and 800 meters depth correspond to directions of pP focusing.

As noted earlier, there is also some yield dependence to the pP phase because of the stronger nonlinear interaction with the free surface for larger events. Figure 42 shows P-waves calculated for a range of azimuths with a take-off angle of 20 degrees. Because of focusing by the mountain, the pP phase is larger than the direct P phase in certain directions (90 degrees is north, where the reflection is largest). Again the pP phase is reduced for the 2017 calculation relative to 2016.

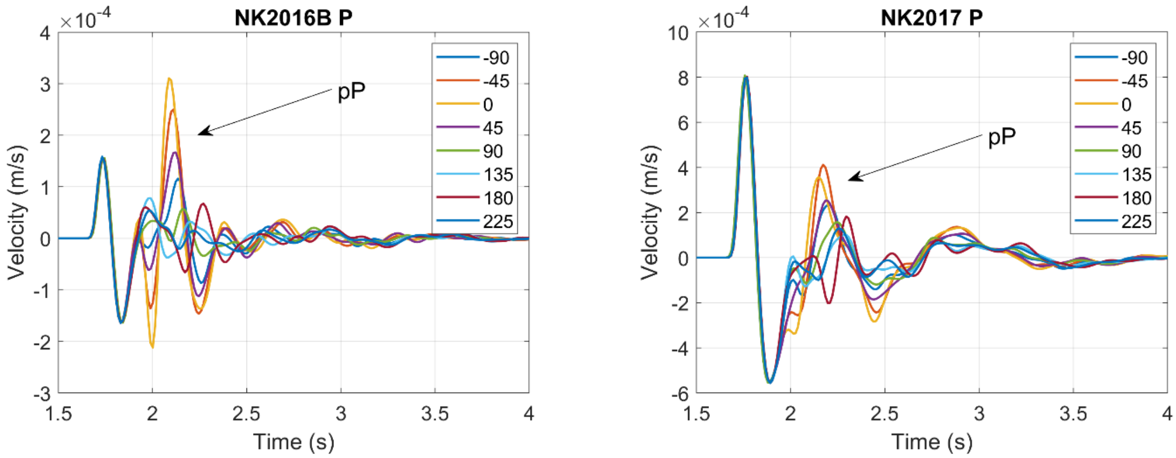

Figure 42. P-waves calculated for a range of azimuths and a takeoff angle of 20 degrees. Left: NK2016B calculation; Right: NK2017 calculation. Lowpass filtered at 5 Hz. Azimuth is clockwise from north, zero is north.

4.4.7 Regional and local waveforms

Full waveform seismograms were calculated from all cram3D calculations for azimuths from zero to 360 degrees at 45 degree intervals and at distances of 10, 25, 50, 100, 250, 500 and 1000 km. Examples are shown in Figure 43 at 10 km and Figure 44 at 1000 km.

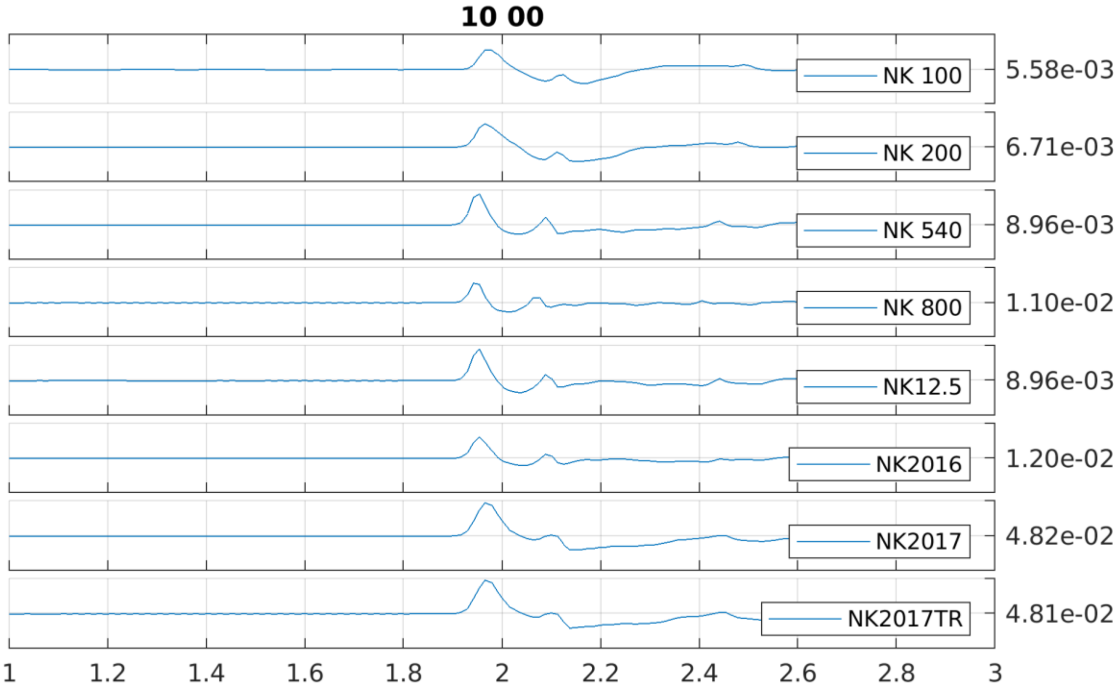

Figure 43. Waveforms 1 to 3 seconds after the explosions for all 8 calculations at 10 km distance. Scale gives the peak amplitude in meters.

There are small differences in the waveforms from all of the calculations at each distance. The full set of pictures is given in Appendix A. The most obvious difference is between the largest calculations (2017 and 2017TR) and the smaller calculations at 1000 km as shown in Figure 44. Much of the high frequency energy is reduced relative to the lower frequency energy. This is most likely a corner frequency effect, with the corner frequency of the explosion source function reduced for the largest events. This can be seen more clearly in Figure 45, which shows the spectra calculated from the waveform segments in Figure 44, which clearly shows the reduction in high frequency energy for the 2017 event. There is also an increase in the 2017 spectra just below 1 Hz which is most likely due to spall.

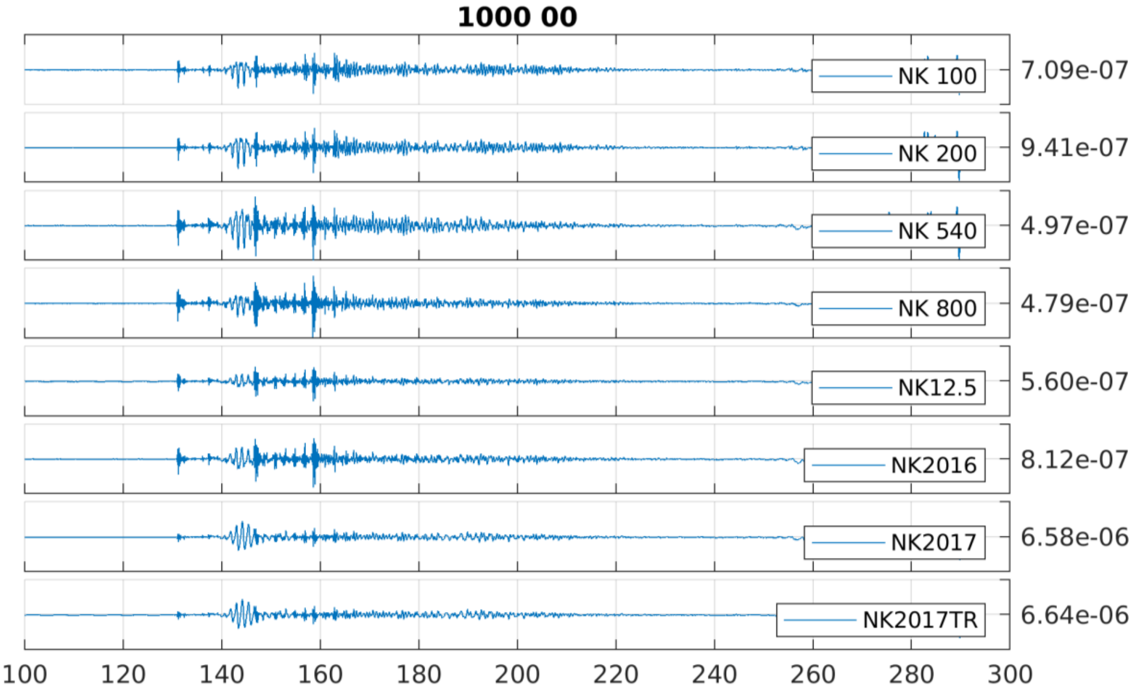

Figure 44. Waveforms 100 to 300 seconds after the explosions for all 8 calculations at 1000 km distance.

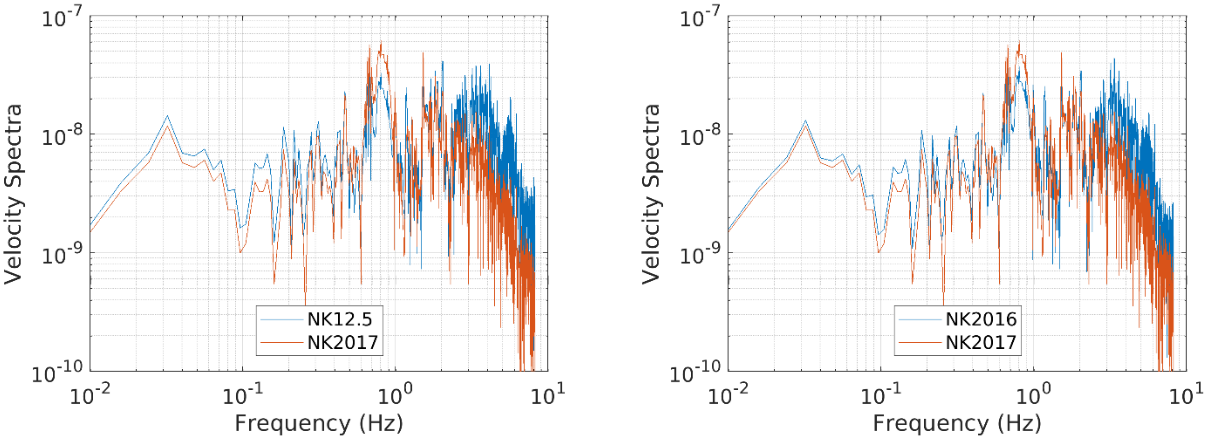

Figure 45. Comparison of velocity spectra at 1000 km from the NK2017 calculation with the NK12.5 (2016A) calculation (left) and the NK2016B calculation (right).

4.5 Surface wave generation

It was mentioned earlier that long period surface waves are generated almost entirely by the static horizontal displacement after the explosion. In this section, we look at this effect in more detail. The representation theorem used to calculate the waveforms is repeated below. The first term in this integral corresponds to surface waves generated by stresses on the monitoring surface, and the second to surface waves generated by displacements on the monitoring surface. The relative sizes of these two terms at 20 seconds is illustrated in Figure 46. The second (displacement) term dominates in all cases. The stress term is only significant for the shallowest explosion inside the mountain (NK_100).

$$u_i(X) = \int_{S_M} \left\{ G_j^i(\xi; X) * T_j^M(\xi) - u_j^M(\xi) * S_{jk}^i(\xi; X) n_k \right\} dA$$

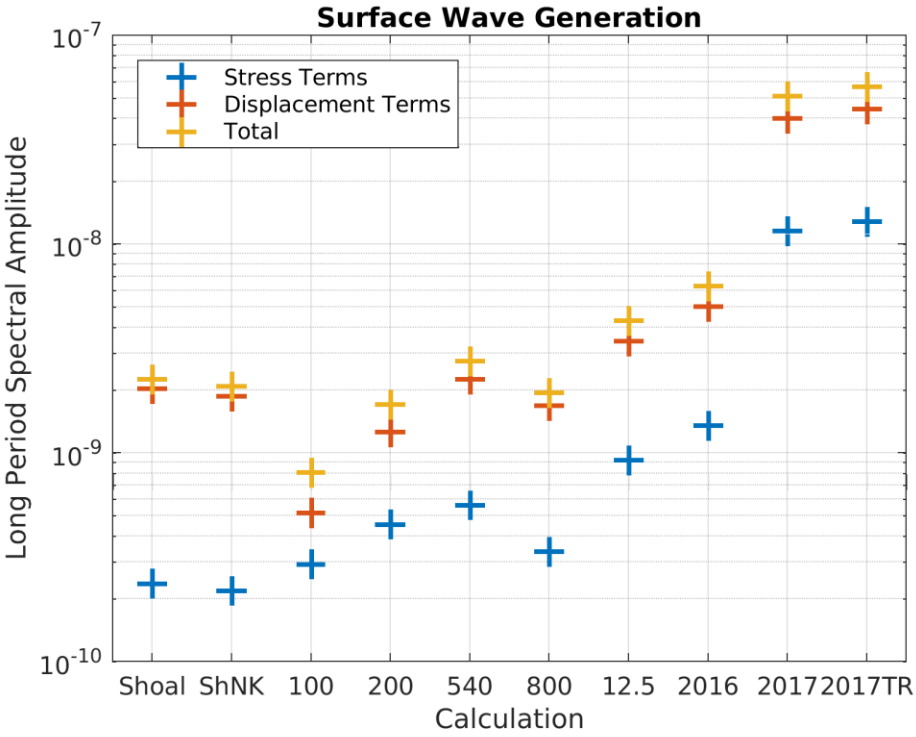

Figure 46. Relative sizes of stress and displacement terms in the representation theorem calculation at 20 seconds for surface waves for all of the calculations. Sh and ShNK refer to the flat Shoal calculation and the Shoal calculation embedded in the North Korean structure.

Figure 47 shows the importance of the displacements normal to the sides of the monitoring surface. The figure shows the ratio of the second (displacement) term in the representation theorem integrated only over the sides to the total displacement. This shows that the long period surface waves are almost entirely generated by the horizontal displacement. This is illustrated with the Shoal calculation in Figure 48.

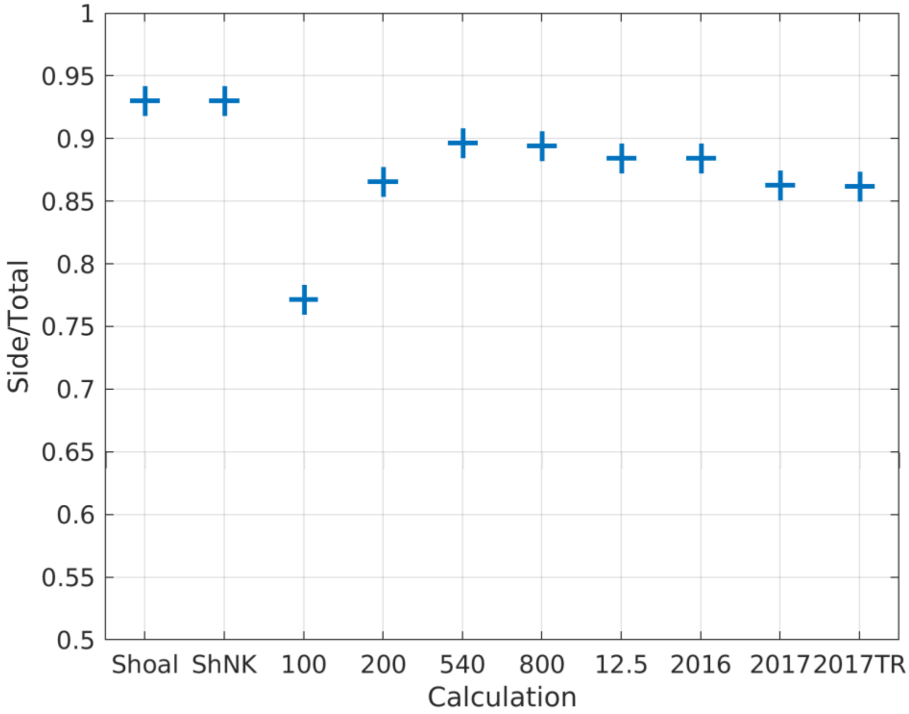

Figure 47. Ratio of the amplitude of the second (displacement) term in the representation theorem integrated over the sides to the total displacement. Long period surface waves are generated primarily by the static horizontal displacement.

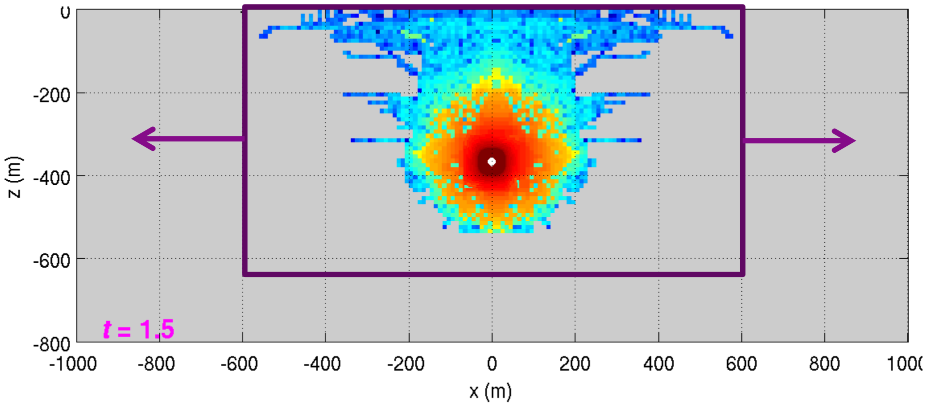

Figure 48. Illustration using the Shoal calculation. The horizontal displacement on the sides of the monitoring surface generates almost all of the long period surface waves.

Figure 49 shows the displacements on two of the monitoring surfaces (except Shoal, which is symmetric) for each of the North Korea calculations. The displacements are concentrated near the surface for all of the calculations. The deepest calculation at 800 meters has more displacement at depth, but of lower magnitude. Figure 50 shows the geometry of the North Korean calculations identifying the sides shown in Figure 49 and the location of the monitoring surface.

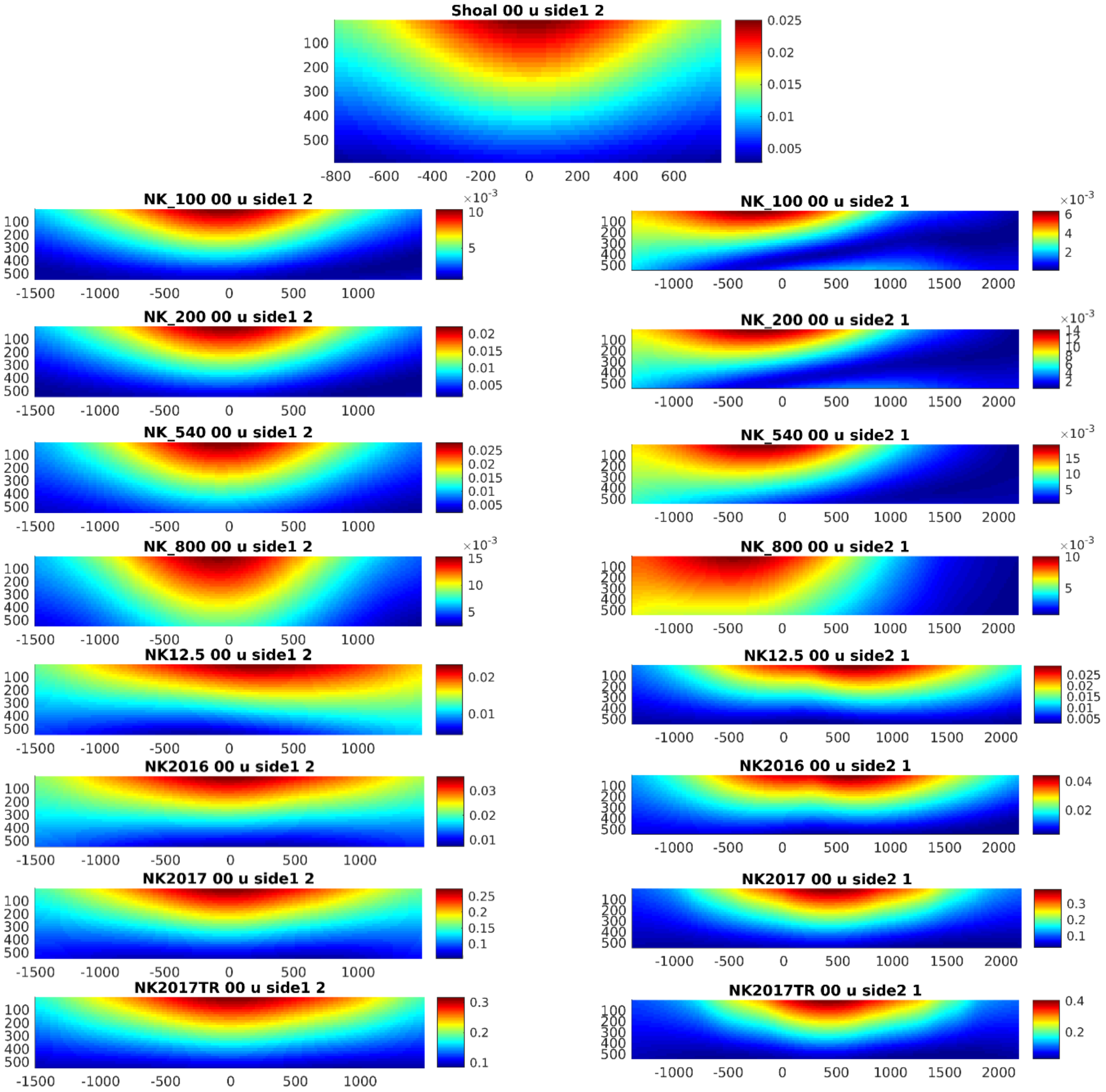

Figure 49. Displacement (meters) normal to the monitoring surface. Top: Shoal. Left: Displacement on south face of monitoring surface for North Korean calculations. Right: Displacement on east face of monitoring surface for the North Korean calculations. (See Figure 50).

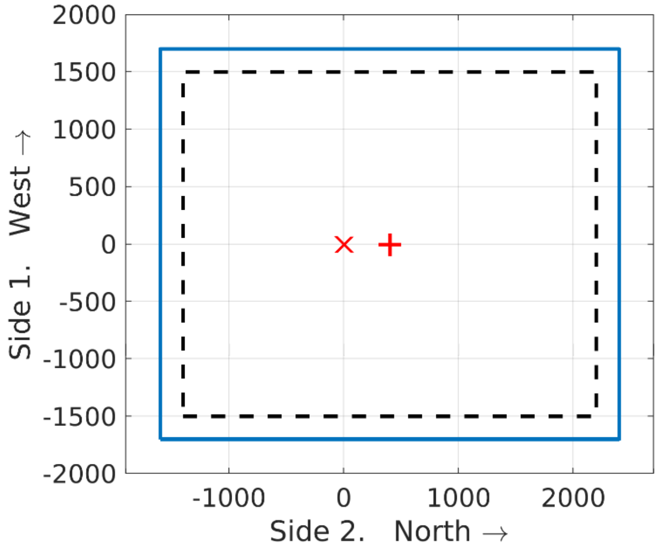

Figure 50. Surface view of grid used in the North Korea calculations showing calculation boundary (solid) and monitoring surface (dashed). The x marks the location of the NK_100 to NK_800 calculations, and the + marks the location of the 2016 and 2017 calculations.

5. Conclusions

We have used three-dimensional nonlinear calculations of explosions at the North Korean test site, together with the representation theorem, to determine the effect of topography and depth on local and regional phases, as well as long period surface waves and far-field body waves. We completed five three-dimensional nonlinear finite difference calculations using the topography of the North Korean test site at the estimated location and depth of the September 2017 nuclear test, with yields of 12.5, 20 and 180 kilotons, plus two additional calculations at 180 kilotons that includes tensile and compressive tectonic stresses.

We calculate large displacements of 2-4 meters on the mountain surfaces near the 2017 explosion, but very little displacement on the surface directly above the explosion which is very close to the mountain peak. This is most likely due to the topography with gravity increasing displacement on downhill slopes, and is consistent with observations of surface motion for this event.

We find that the topography increases the amplitude of the surface reflected pP phase for all events at this test site, however the effect is reduced for the 2017 explosion because of strong nonlinear interaction with the free surface (Figure 51).

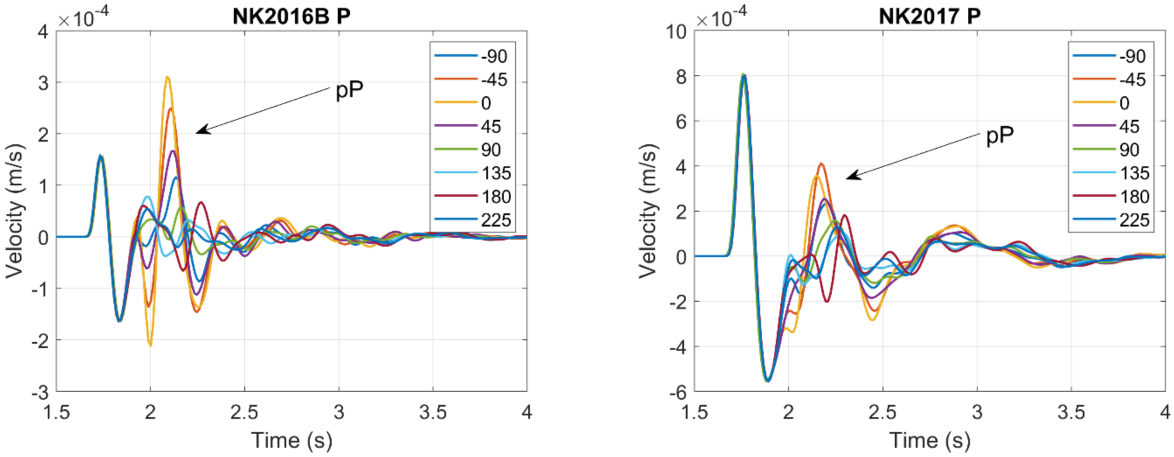

Figure 51. P-waves calculated for a range of azimuths and a takeoff angle of 20 degrees. Left: NK2016B calculation; Right: NK2017 calculation. Lowpass filtered at 5 Hz. Azimuth is clockwise from north, zero is north.

The North Korean explosions appear to be anomalous in generating much larger surface waves than are expected based on surface waves observed from buried explosions in other areas. However, surface waves derived from the calculations are very consistent with the observed surface waves (Figure 52. See also the waveform comparison in Figure 23). This is really quite remarkable considering how large the surface waves are compared to the global surface wave data set from other explosions. Calculations show that explosions at the base of a mountain have amplified surface waves, which explains part of the anomaly. The mountain reduces horizontal stress, which has an effect similar to tensile tectonic stress, so added tensile stress causes only a small additional amplification. Similarly, compressive tectonic stress causes only a small reduction in surface wave amplitudes.

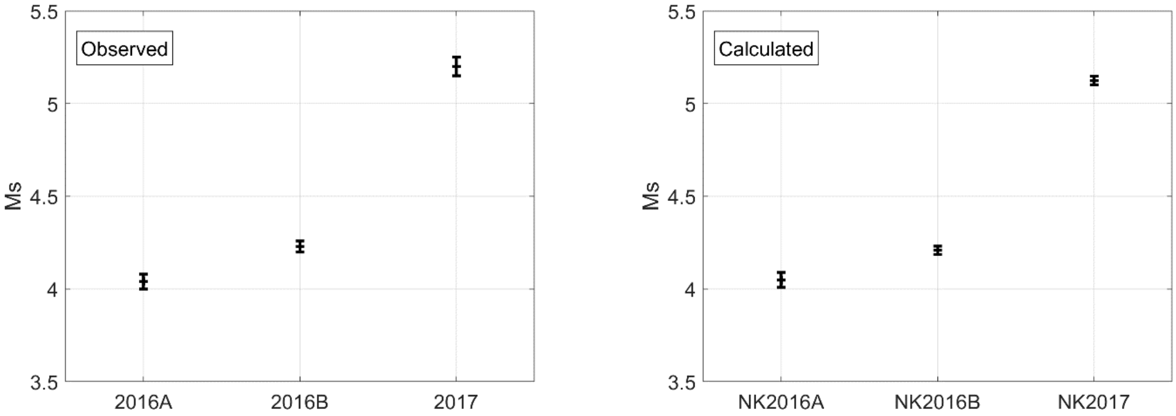

Figure 52. Left: Ms and standard deviation measured from the observed surface waves at the five closest stations for the 2016 and 2017 explosions. Right: Ms and standard deviation measured from the calculated surface waves at the five closest stations for the 2016 and 2017 explosions.

In addition to the effect of topography, the remaining surface wave anomaly appears to be due to bias in the global data set caused by surface wave reduction due to the free surface interaction and compressive tectonic release. Figure 53 shows a comparison of scaled Ms vs. scaled yield for a series of axisymmetric calculations and Ms vs. scaled yield for four hard rock sites. Data from the Balapan site is a good match to calculations with compressive tectonic release. Ms is decreased both by the compressive stress and the free surface interaction. Degelen similarly shows low values at shallow depths, but more of a range, with the largest scaled Ms approaching that of the North Korean events. This is most likely due to the effects of topography at the Degelen test site, which is in a larger, broader mountain than North Korea, so it appears that the Degelen Ms values range from the low values expected for an explosion in a flat-layered structure to the high values expected in a region with strong topography.

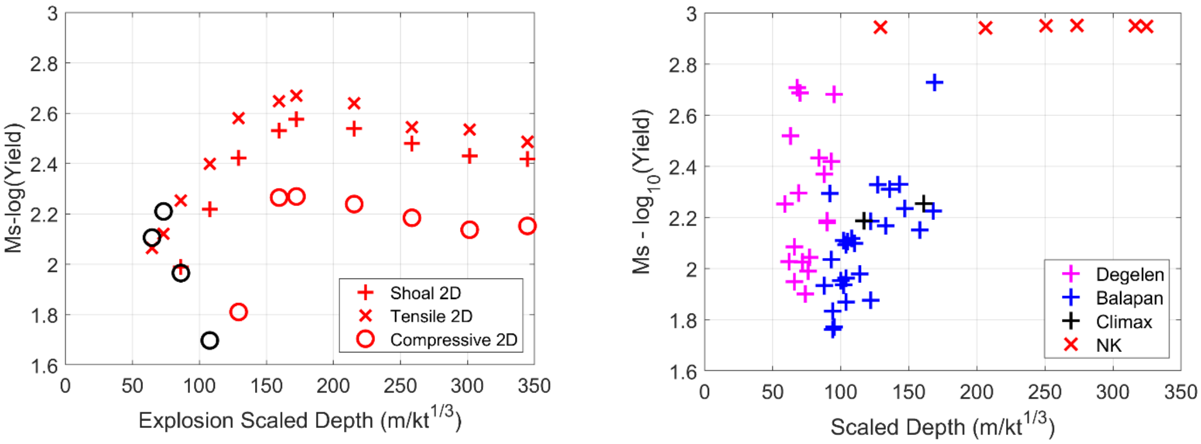

Figure 53. Left: Ms-Log(Yield) vs. scaled depth for axisymmetric calculations. Black circles indicate phase reversals. Right: Ms-Log(Yield) vs. scaled depth for North Korean, Degelen, Balapan and Climax Stock (NTS) hard rock explosions. Data is from Patton (2016).

6. References

Apsel, R. J. and J. E. Luco (1983), On the Green's Functions for a layered half-space, Part II, Bull. Seismol. Soc. Am. 73, 931–951.

Bache, T. C. and D. G. Harkrider (1976). The body waves due to a general seismic source in a layered earth model, Bull. Seismol. Soc. Am. 66, 1805–1819.

Bache, T. C., S. M. Day, and H. J. Swanger (1982), Rayleigh wave synthetic seismograms from multi-dimensional simulations of underground explosions," Bull. Seismol. Soc. Am. 72, 15–28.

Bonner, J. L., D. R. Russell, D. G. Harkrider, D. T. Reiter, and R. B. Herrmann (2006), "Development of a time-domain, variable period surface-wave magnitude measurement procedure for application at regional and teleseismic distances, part II: application and M_s-m_b performance," *Bull. Seism. Soc. Am.*, **96**, 678-696, doi: 10.1785/0120050056.

Gibbons, S. J., F. Pabian, S.P. Näsholm, T. Kværna, S. Mykkeltveit (2017). Accurate relative location estimates for the North Korean nuclear tests using empirical slowness corrections, Geophysical Journal International, Volume 208, Issue 1, Pages 101–117, January.

Luco, J. E. and R. J. Apsel (1983). On the Green's Functions for a layered half-space, Part I," Bull. Seismol. Soc. Am. 73, 909–929.

Murphy, J. R., J. L. Stevens, B. C. Kohl and T. J. Bennett (2013), "Advanced seismic analyses of the source characteristics of the 2006 and 2009 North Korean nuclear tests," *Bull. Seism. Soc. Am.*, **103**, No. 3, 1640–1661, doi: 10.1785/0120120194.

NASA/METI/AIST/Japan Spacesystems, and U.S./Japan ASTER Science Team (2009). ASTER Global Digital Elevation Model [Data set]. NASA EOSDIS Land Processes DAAC. doi: 10.5067/ASTER/ASTGTM.002. (https://lpdaac.usgs.gov), accessed May 11, 2015, at http://dx.doi.org/10.5067/ASTER/ASTGTM.002.

Pabian, F. V. (2017), "Detected Surface Effects of the September 3, 2017 Declared Nuclear Test," Abstract (S34C-01) presented at 2017 AGU Fall Meeting, New Orleans, LA, 11-15 Dec.

Patton, H. J. and S. R. Taylor (2008), "Effects of shock-induced tensile failure on mb-Ms discrimination: contrasts between historic nuclear explosions and the North Korean test of 9 October 2006," *Geophys Res. Lett.*, **35**, L14301, doi: 10.1029/2008GL034211.

Patton, H. J., and S. R. Taylor (2011). "The apparent explosion moment: Inferences of volumetric moment due to source medium damage by underground explosions, *J. Geophys. Res.*, **116**, no. B03310, doi:10.1029/2010JB007937.

Patton, H. J. (2016), "A physical basis for Ms-yield scaling in hard rock and implications for late-time damage of the source medium," *Geophys. J. Int.*, **206**, 191-204, doi: 10.1093/gji/ggw140.

Russell, D. R. (2006), “Development of a time-domain, variable period surface-wave magnitude measurement procedure for application at regional and teleseismic distances, part I: theory,” *Bull. Seism. Soc. Am.*, **96**, 665-677, doi: 10.1785/0120050055.

Stevens, J. L. (1986), "Estimation of scalar moments from explosion-generated surface waves," *Bull. Seism. Soc. Am.*, v. **76**, pp. 123-151.

Stevens, J. L., K. L. McLaughlin, B. Shkoller, and S. M. Day (1993), "2-D axisymmetric calculations of surface waves generated by an explosion in an island, mountain, and sedimentary basin," *Geophysical Journal International*, v. **114**, pp. 548-560. doi: 10.1111/j.1365-246X.1993.tb06986.x

Stevens, J. L. and K. L. McLaughlin (2001), “Optimization of surface wave identification and measurement,” *Pure and Applied Geophysics*, V. **158**, no. 7, pp 1547-1582, doi:10.1007/PL00001234.

Stevens, J. L. and J. R. Murphy (2001), “Yield Estimation from surface wave amplitudes,” *Pure and Applied Geophysics*, **158**, 2227-2251.

Stevens, J. L., D. A. Adams, G. E. Baker, M. G. Eneva and H. Xu (2005), "Improved Surface Wave Dispersion Models, Amplitude Measurements and Azimuth Estimates," SAIC Final Report submitted to AFRL under contract DTRA01-01-C-0082, March.

Stevens, J. L., H. Xu, J. W. Given and G. Eli Baker (2008), “Development of surface wave dispersion and attenuation maps and improved methods for measuring surface waves,” SAIC final report submitted to Air Force Research Laboratory, May.

Stevens, Jeffry L., Heming Xu, Michael O’Brien, Walter Nagy and Norton Rimer (2011), “Wave Propagation from Complex 3D Sources Using the Representation Theorem,” SAIC final report SAIC-11/3003 to Air Force Research Laboratory, AFRL-RV-HA-TR-2011-1019, March.

Stevens, J. L. and T. W. Thompson (2015), “3D Numerical Modeling of Tectonic Strain Release from Explosions,” *Bull. Seism. Soc. Am.*, **105**, 612-621, doi: 10.1785/0120140125.

Stevens, J., L., M. O’Brien, H. Xu and N. Rimer (2017), “User Manual for the CRAM3D Finite Element Code, Version 3.0” Technical Report to Air Force Research Laboratory, Leidos-17/3004, May.

Stevens, J. L., M. O’Brien and T. W. Thompson (2017a), “Decomposition of the Seismic Source Using Numerical Simulations and Observations of Nuclear Explosions,” Leidos final technical report Leidos-17/3002 to Air Force Research Laboratory, May.

Wang, T., M. Nikkhoo, M. Motagh, S. Wei, S. Barbot and R. Burgmann (2017), September 3rd, 2017 underground nuclear test in North Korea: Results from satellite radar imagery and dislocation modeling, Abstract (S34C-02) presented at 2017 AGU Fall Meeting, New Orleans, LA, 11-15 Dec.

Zhang, M. and L. Wen (2013), “High-precision location and yield of North Korea’s 2013 nuclear test,” Geophysical Research Letters, 40, 1–6, doi:10.1002/grl.50607.

Appendix A. Waveform plots for all calculations

In this appendix, we show all of the waveform plots from all of the calculations at distances from 10 to 1000 km and at azimuths in increments of 45 degrees. The header on each figure shows the distance in km and azimuth in degrees, the legend shows the calculation, and the number at the right is the peak amplitude in m/s. All plots use a fixed group velocity window of 10 km/s to 3.45 km/s, which cuts off the large surface wave which would otherwise dominate each plot.

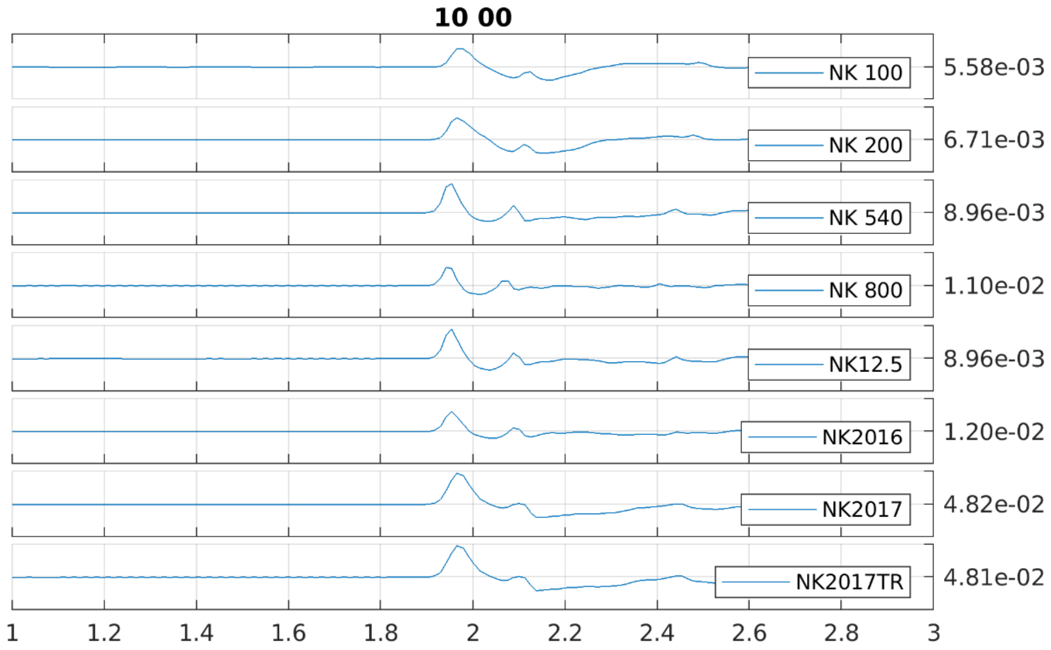

10 00

NK 100
5.58e-03
NK 200
6.71e-03
NK 540
8.96e-03
NK 800
1.10e-02
NK12.5
8.96e-03
NK2016
1.20e-02
NK2017
4.82e-02
NK2017TR
4.81e-02
1
1.2
1.4
1.6
1.8
2
2.2
2.4
2.6
2.8
3

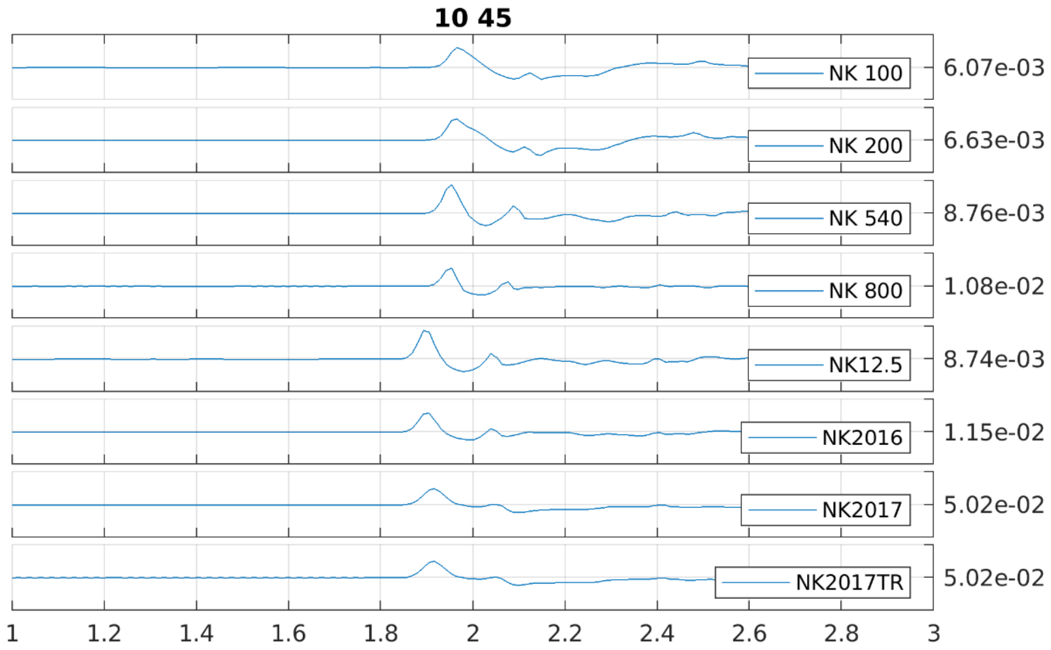

10 45

NK 100
6.07e-03
NK 200
6.63e-03
NK 540
8.76e-03
NK 800
1.08e-02
NK12.5
8.74e-03
NK2016
1.15e-02
NK2017
5.02e-02
NK2017TR
5.02e-02
1
1.2
1.4
1.6
1.8
2
2.2
2.4
2.6
2.8
3

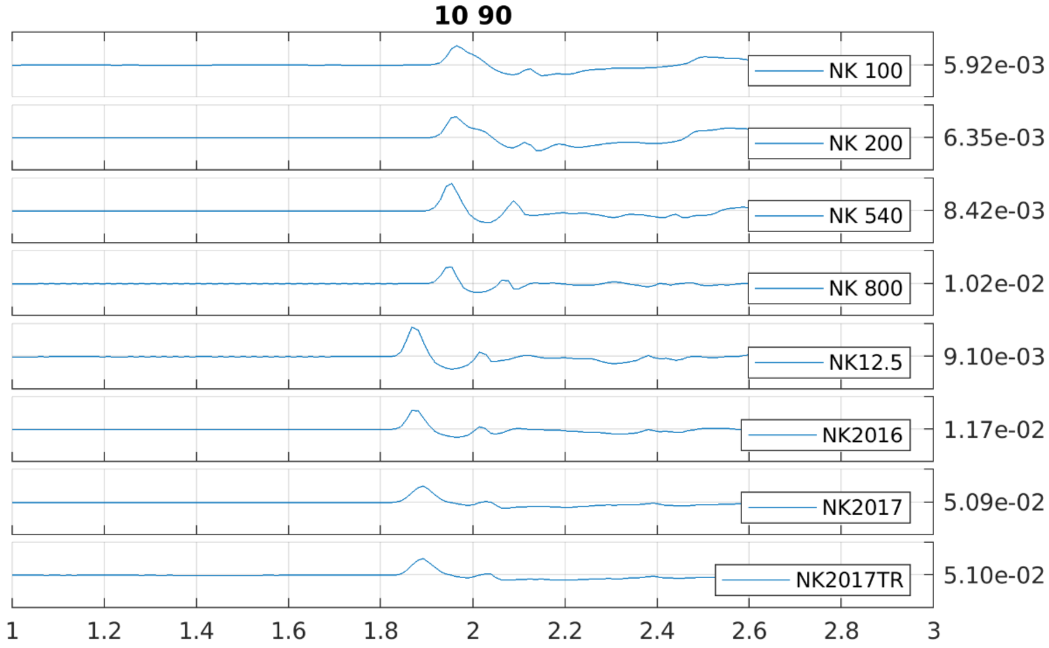
10 90
NK 100
5.92e-03
NK 200
6.35e-03
NK 540
8.42e-03
NK 800
1.02e-02
NK12.5
9.10e-03
NK2016
1.17e-02
NK2017
5.09e-02
NK2017TR
5.10e-02
1
1.2
1.4
1.6
1.8
2
2.2
2.4
2.6
2.8
3

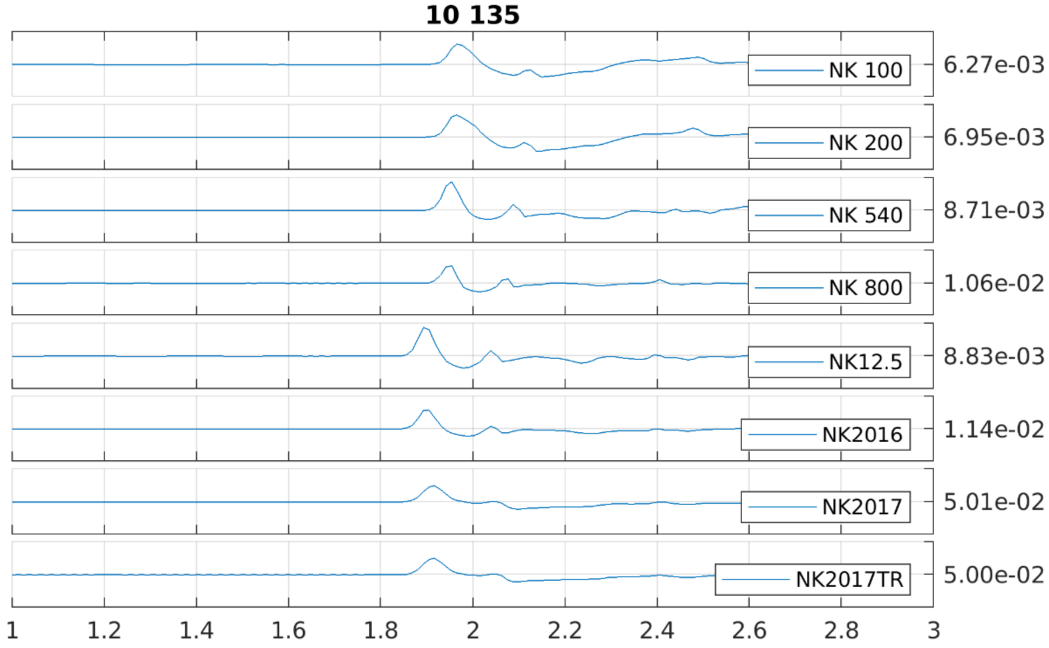
10 135
NK 100
6.27e-03
NK 200
6.95e-03
NK 540
8.71e-03
NK 800
1.06e-02
NK12.5
8.83e-03
NK2016
1.14e-02
NK2017
5.01e-02
NK2017TR
5.00e-02
1
1.2
1.4
1.6
1.8
2
2.2
2.4
2.6
2.8
3

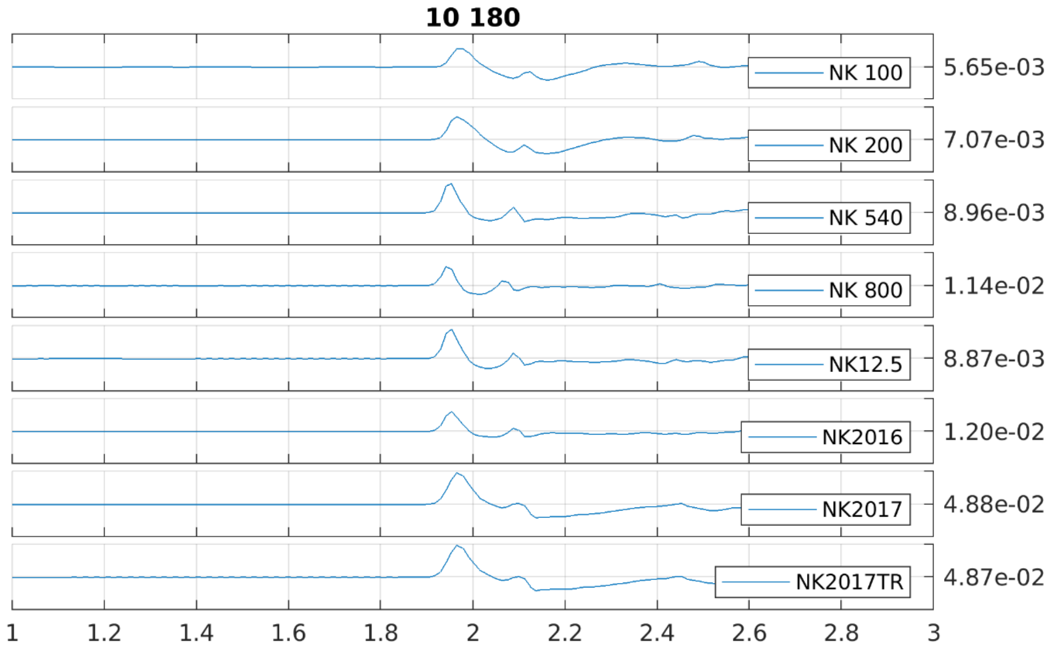
10 180
NK 100
5.65e-03
NK 200
7.07e-03
NK 540
8.96e-03
NK 800
1.14e-02
NK12.5
8.87e-03
NK2016
1.20e-02
NK2017
4.88e-02
NK2017TR
4.87e-02
1
1.2
1.4
1.6
1.8
2
2.2
2.4
2.6
2.8
3

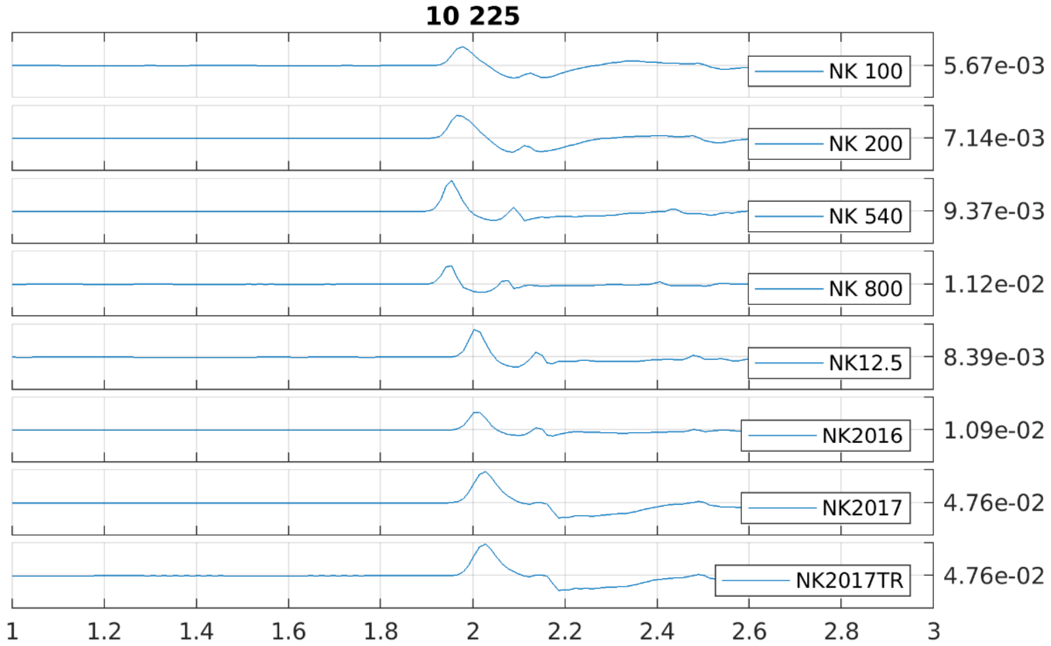
10 225
NK 100
5.67e-03
NK 200
7.14e-03
NK 540
9.37e-03
NK 800
1.12e-02
NK12.5
8.39e-03
NK2016
1.09e-02
NK2017
4.76e-02
NK2017TR
4.76e-02
1
1.2
1.4
1.6
1.8
2
2.2
2.4
2.6
2.8
3

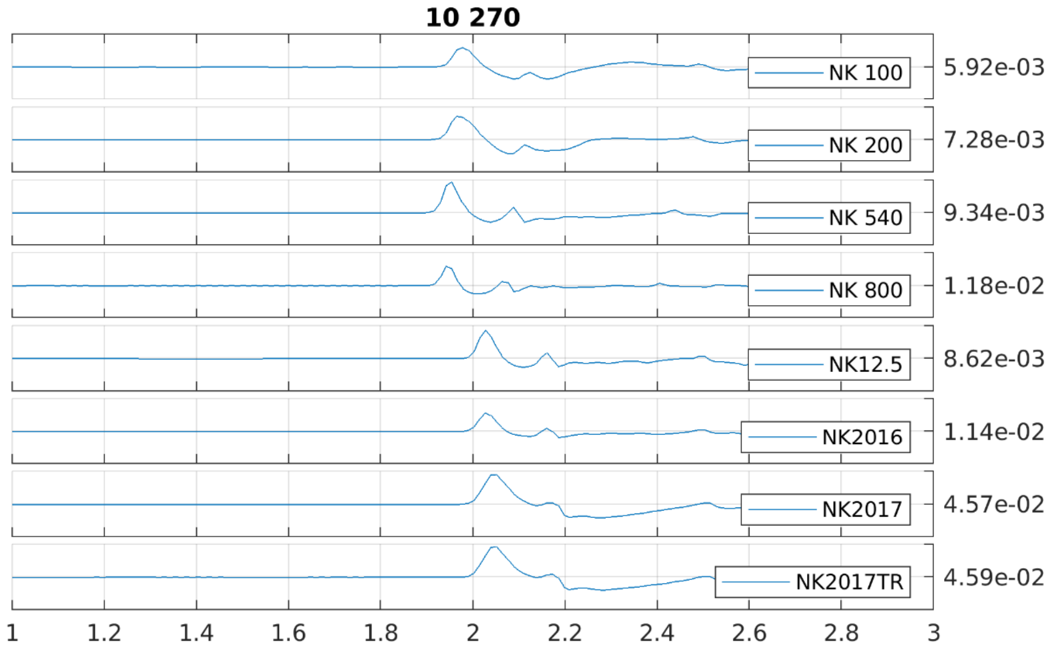
10 270
NK 100
5.92e-03
NK 200
7.28e-03
NK 540
9.34e-03
NK 800
1.18e-02
NK12.5
8.62e-03
NK2016
1.14e-02
NK2017
4.57e-02
NK2017TR
4.59e-02
1
1.2
1.4
1.6
1.8
2
2.2
2.4
2.6
2.8
3

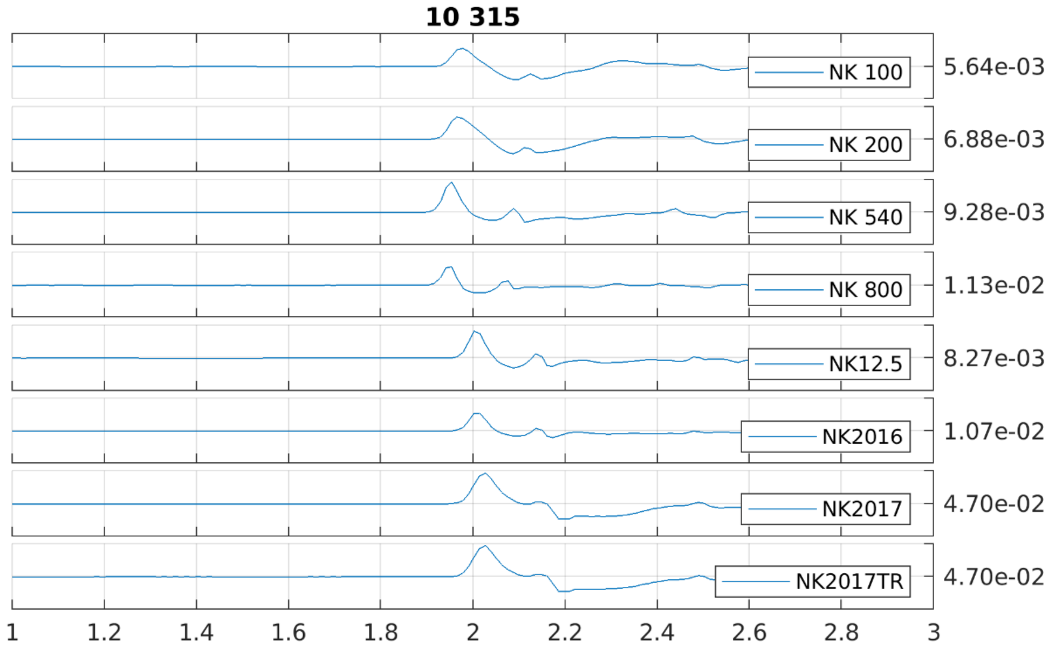
10 315
NK 100
5.64e-03
NK 200
6.88e-03
NK 540
9.28e-03
NK 800
1.13e-02
NK12.5
8.27e-03
NK2016
1.07e-02
NK2017
4.70e-02
NK2017TR
4.70e-02
1
1.2
1.4
1.6
1.8
2
2.2
2.4
2.6
2.8
3

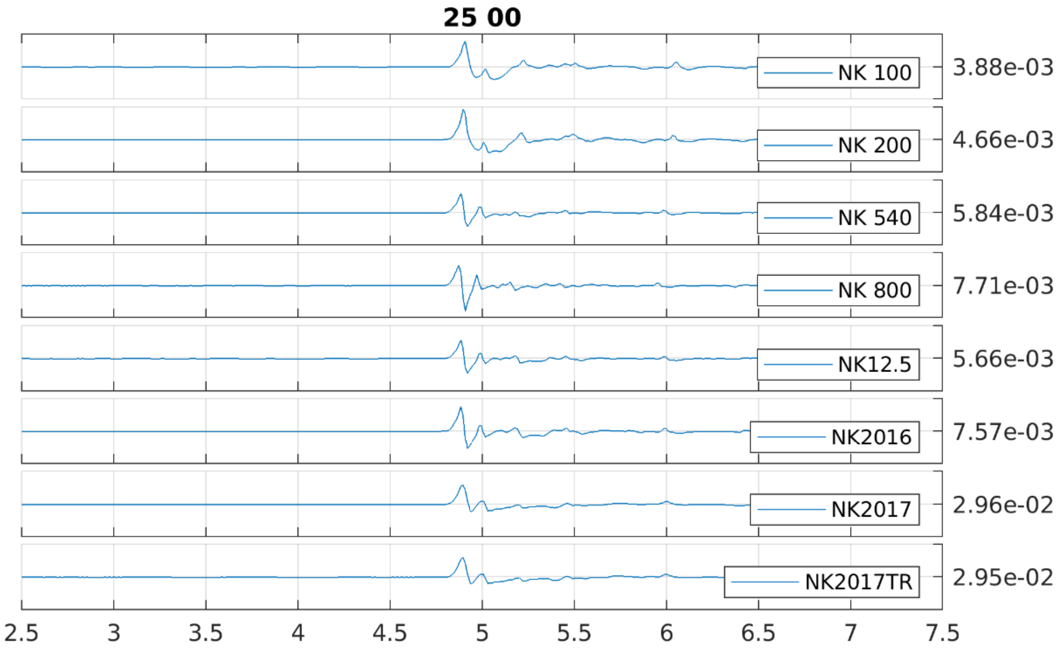
25 00
NK 100
3.88e-03
NK 200
4.66e-03
NK 540
5.84e-03
NK 800
7.71e-03
NK12.5
5.66e-03
NK2016
7.57e-03
NK2017
2.96e-02
NK2017TR
2.95e-02
2.5
3
3.5
4
4.5
5
5.5
6
6.5
7
7.5

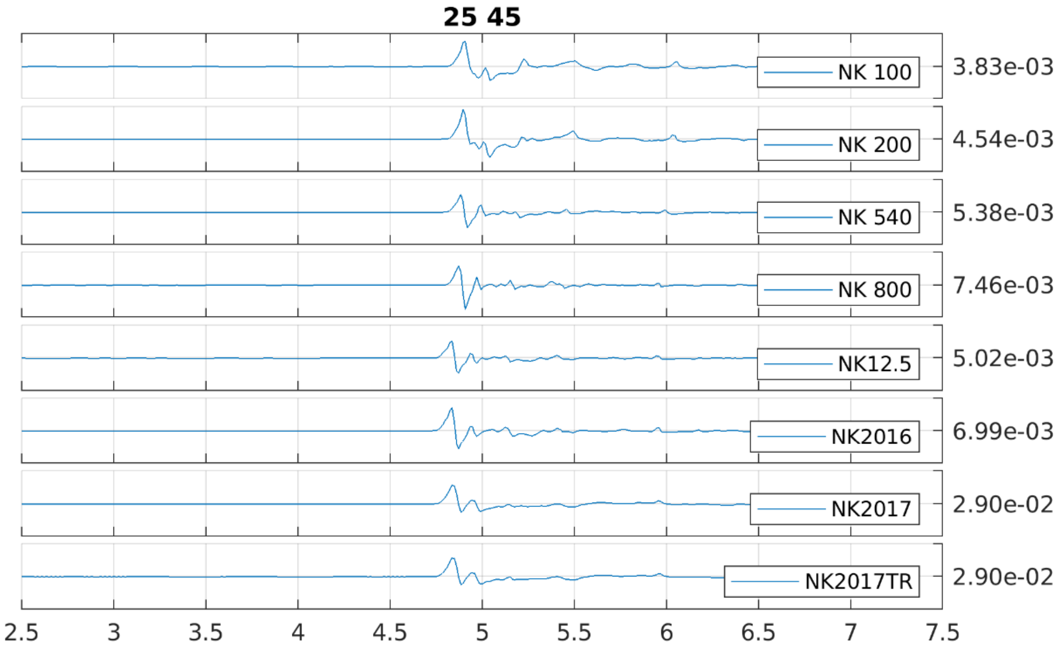
25 45
NK 100
3.83e-03
NK 200
4.54e-03
NK 540
5.38e-03
NK 800
7.46e-03
NK12.5
5.02e-03
NK2016
6.99e-03
NK2017
2.90e-02
NK2017TR
2.90e-02
2.5
3
3.5
4
4.5
5
5.5
6
6.5
7
7.5

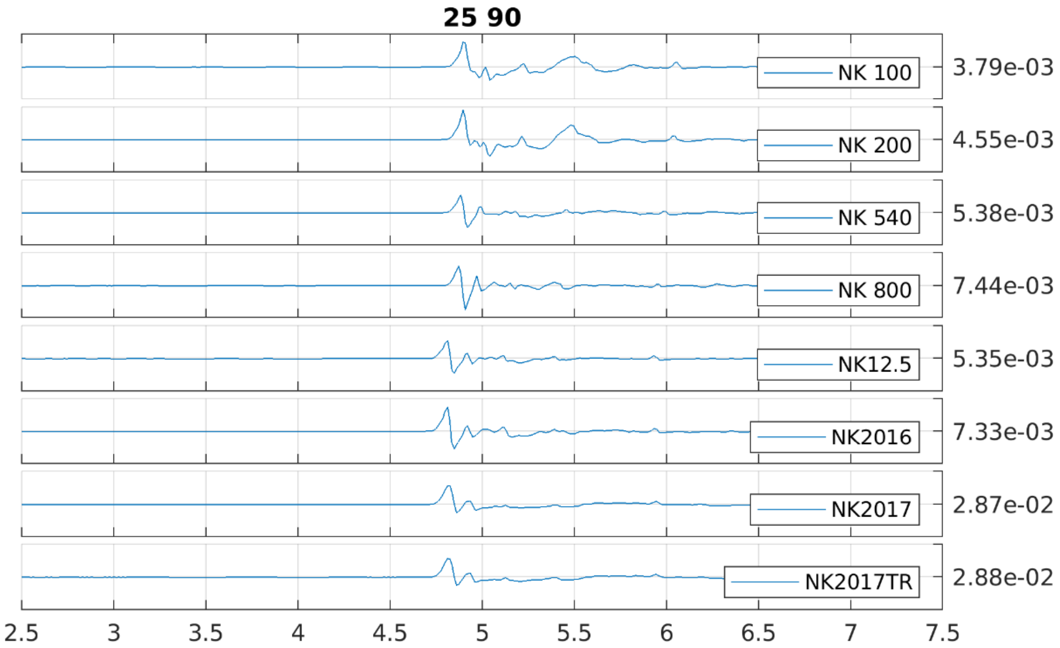
25 90
NK 100
3.79e-03
NK 200
4.55e-03
NK 540
5.38e-03
NK 800
7.44e-03
NK12.5
5.35e-03
NK2016
7.33e-03
NK2017
2.87e-02
NK2017TR
2.88e-02
2.5
3
3.5
4
4.5
5
5.5
6
6.5
7
7.5

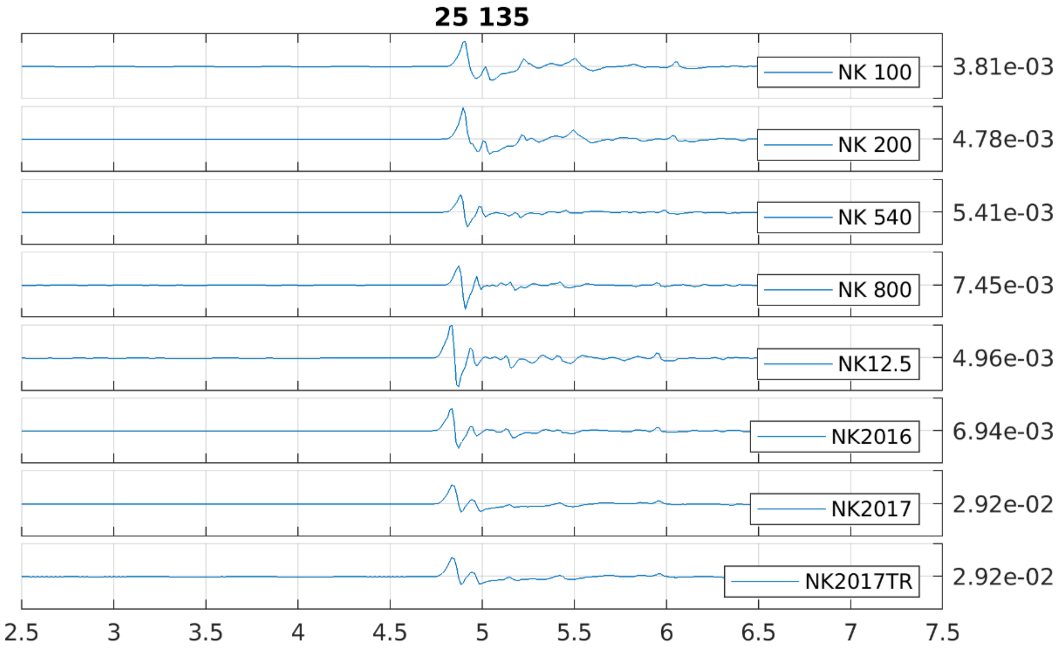
25 135
NK 100
3.81e-03
NK 200
4.78e-03
NK 540
5.41e-03
NK 800
7.45e-03
NK12.5
4.96e-03
NK2016
6.94e-03
NK2017
2.92e-02
NK2017TR
2.92e-02
2.5
3
3.5
4
4.5
5
5.5
6
6.5
7
7.5

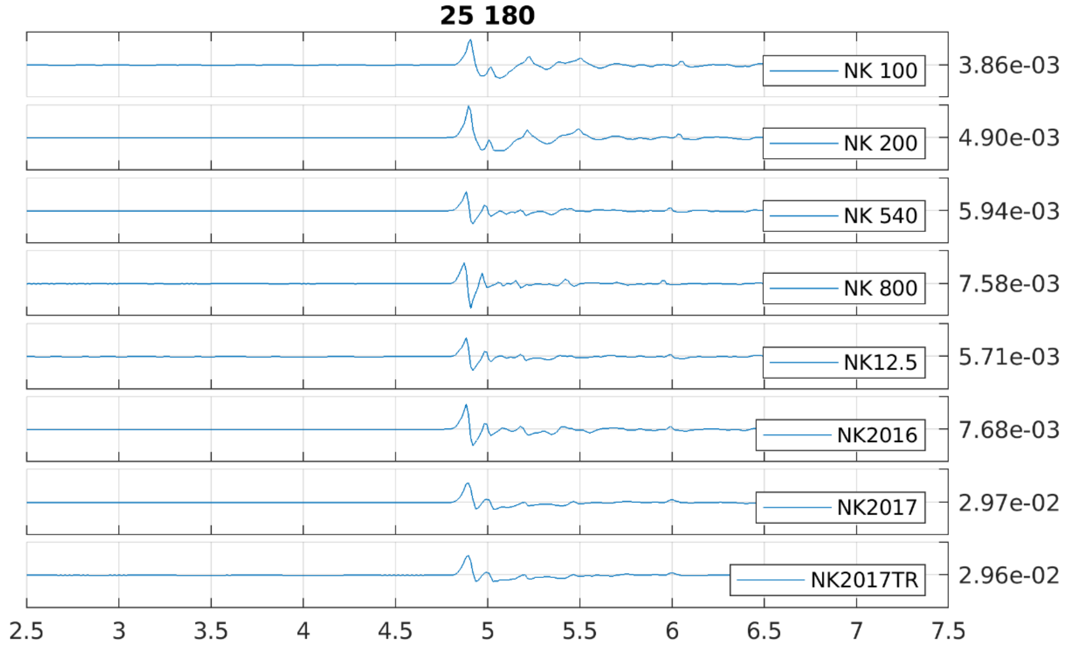
25 180
NK 100
3.86e-03
NK 200
4.90e-03
NK 540
5.94e-03
NK 800
7.58e-03
NK12.5
5.71e-03
NK2016
7.68e-03
NK2017
2.97e-02
NK2017TR
2.96e-02
2.5
3
3.5
4
4.5
5
5.5
6
6.5
7
7.5

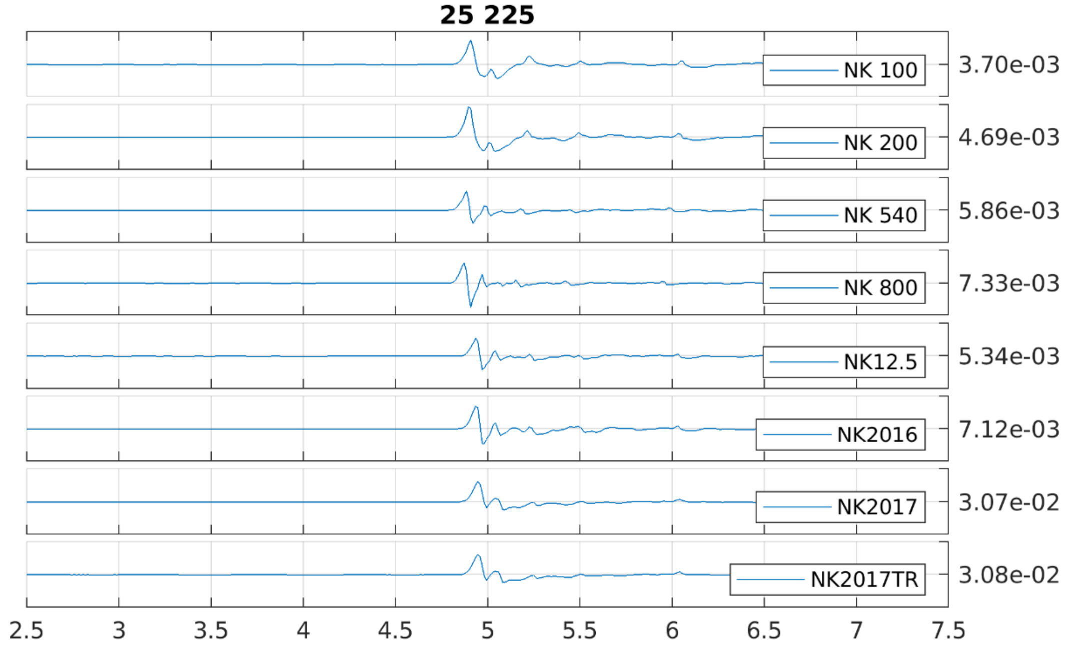
25 225
NK 100
3.70e-03
NK 200
4.69e-03
NK 540
5.86e-03
NK 800
7.33e-03
NK12.5
5.34e-03
NK2016
7.12e-03
NK2017
3.07e-02
NK2017TR
3.08e-02
2.5
3
3.5
4
4.5
5
5.5
6
6.5
7
7.5

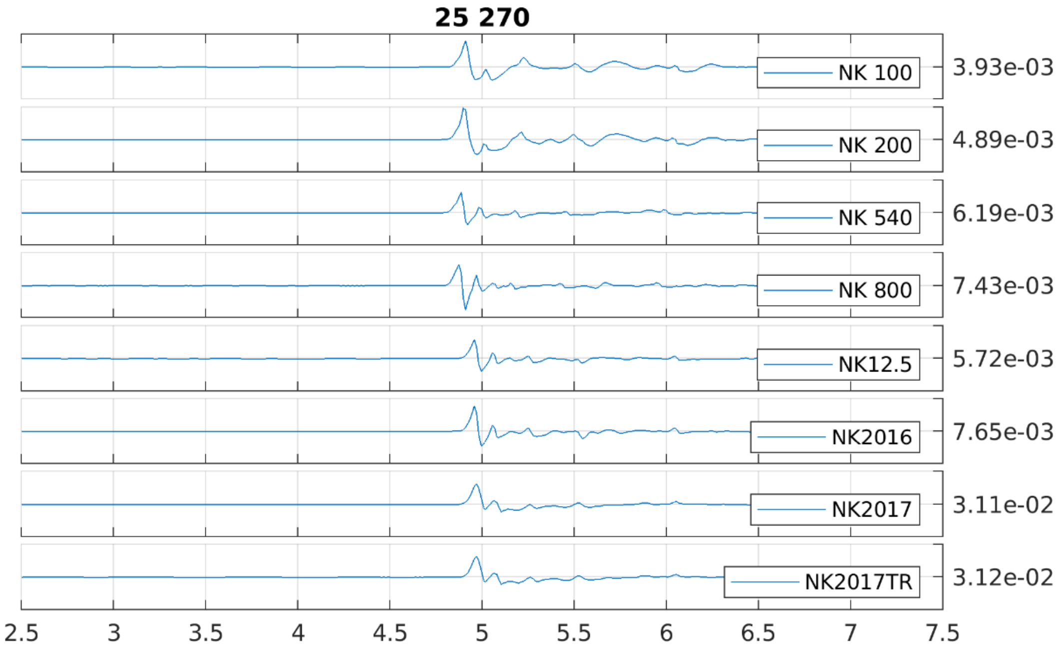
25 270
NK 100
3.93e-03
NK 200
4.89e-03
NK 540
6.19e-03
NK 800
7.43e-03
NK12.5
5.72e-03
NK2016
7.65e-03
NK2017
3.11e-02
NK2017TR
3.12e-02
2.5
3
3.5
4
4.5
5
5.5
6
6.5
7
7.5

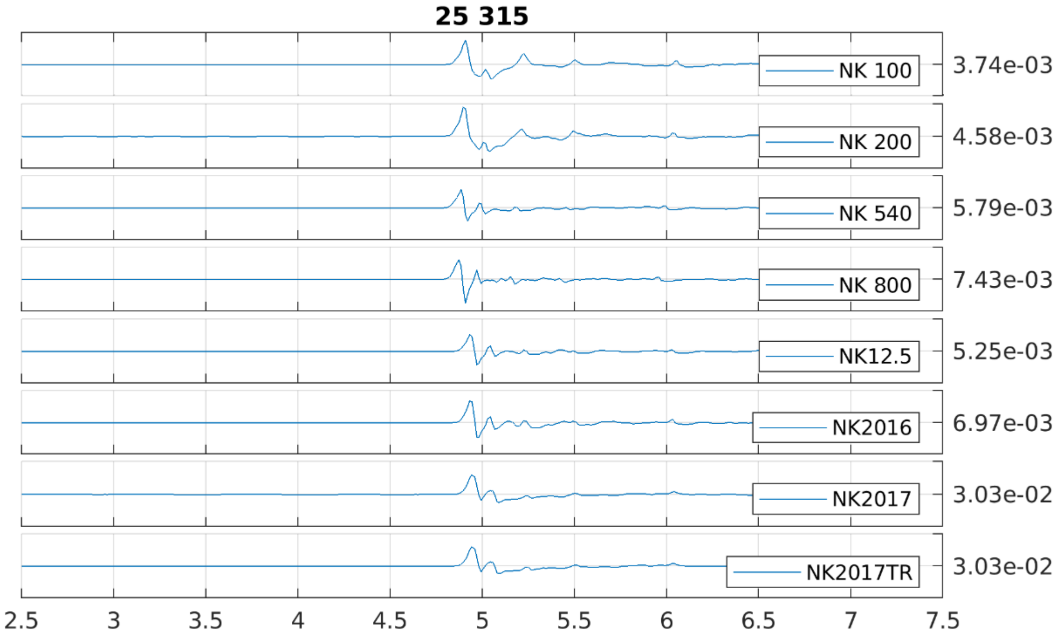
25 315
NK 100
3.74e-03
NK 200
4.58e-03
NK 540
5.79e-03
NK 800
7.43e-03
NK12.5
5.25e-03
NK2016
6.97e-03
NK2017
3.03e-02
NK2017TR
3.03e-02
2.5
3
3.5
4
4.5
5
5.5
6
6.5
7
7.5

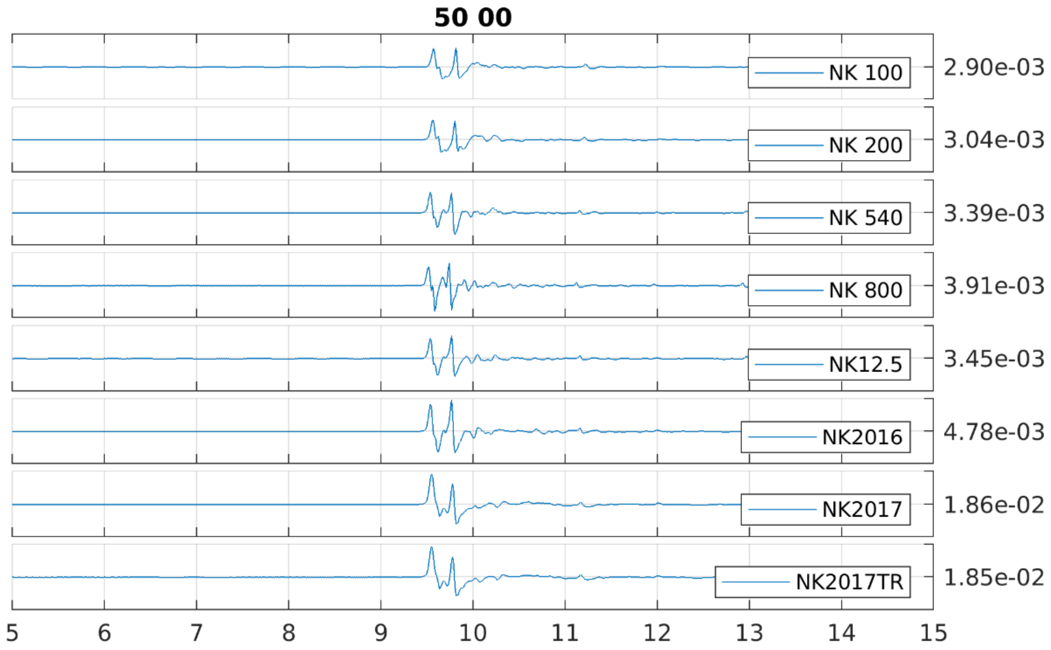
50 00
NK 100
2.90e-03
NK 200
3.04e-03
NK 540
3.39e-03
NK 800
3.91e-03
NK12.5
3.45e-03
NK2016
4.78e-03
NK2017
1.86e-02
NK2017TR
1.85e-02
5
6
7
8
9
10
11
12
13
14
15

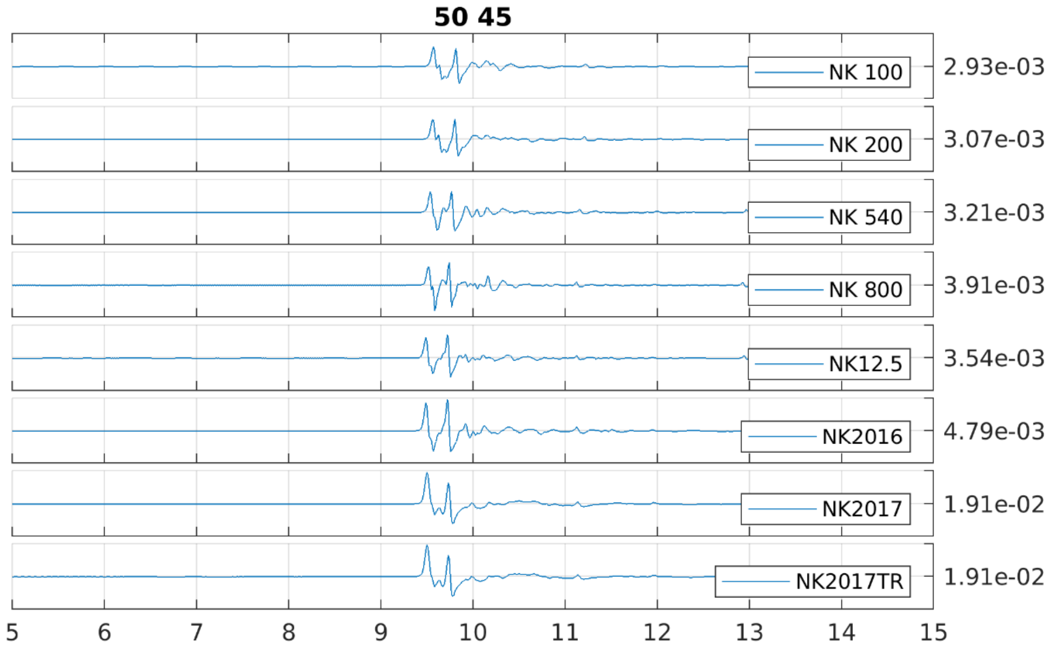
50 45
NK 100
2.93e-03
NK 200
3.07e-03
NK 540
3.21e-03
NK 800
3.91e-03
NK12.5
3.54e-03
NK2016
4.79e-03
NK2017
1.91e-02
NK2017TR
1.91e-02
5
6
7
8
9
10
11
12
13
14
15

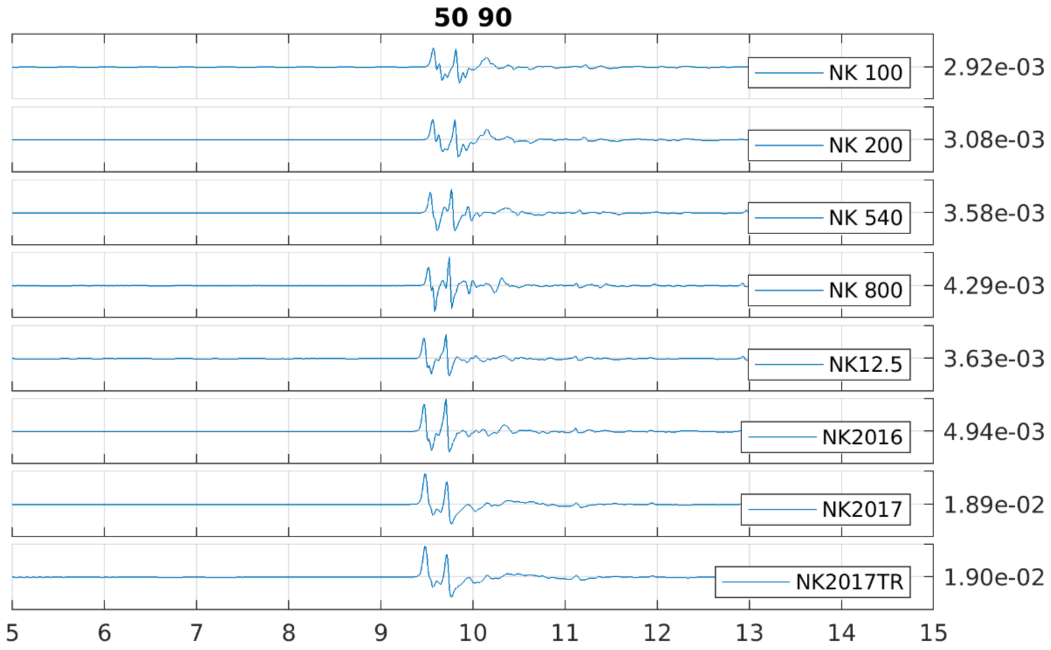
50 90

NK 100
2.92e-03
NK 200
3.08e-03
NK 540
3.58e-03
NK 800
4.29e-03
NK12.5
3.63e-03
NK2016
4.94e-03
NK2017
1.89e-02
NK2017TR
1.90e-02
5
6
7
8
9
10
11
12
13
14
15

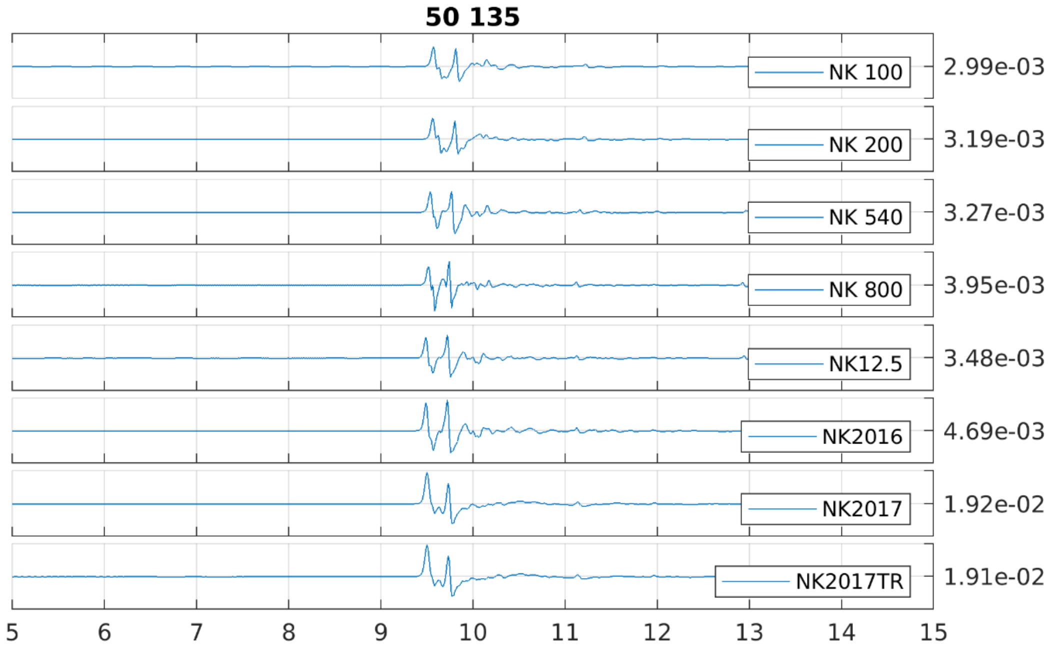
50 135

NK 100
2.99e-03
NK 200
3.19e-03
NK 540
3.27e-03
NK 800
3.95e-03
NK12.5
3.48e-03
NK2016
4.69e-03
NK2017
1.92e-02
NK2017TR
1.91e-02
5
6
7
8
9
10
11
12
13
14
15

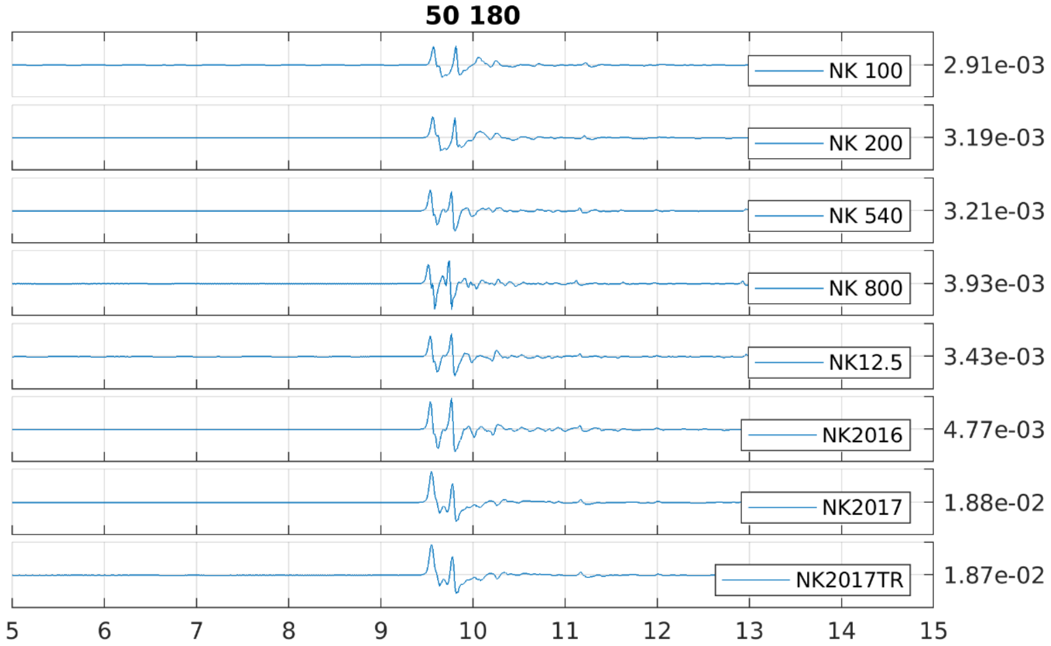
50 180

NK 100
2.91e-03
NK 200
3.19e-03
NK 540
3.21e-03
NK 800
3.93e-03
NK12.5
3.43e-03
NK2016
4.77e-03
NK2017
1.88e-02
NK2017TR
1.87e-02
5
6
7
8
9
10
11
12
13
14
15

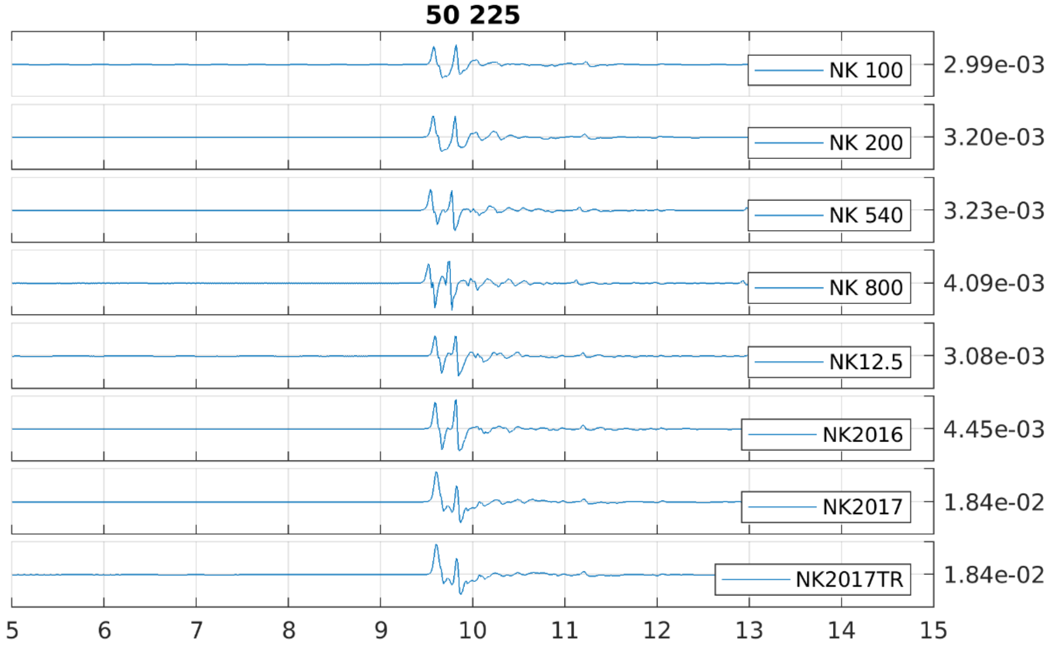
50 225

NK 100
2.99e-03
NK 200
3.20e-03
NK 540
3.23e-03
NK 800
4.09e-03
NK12.5
3.08e-03
NK2016
4.45e-03
NK2017
1.84e-02
NK2017TR
1.84e-02
5
6
7
8
9
10
11
12
13
14
15

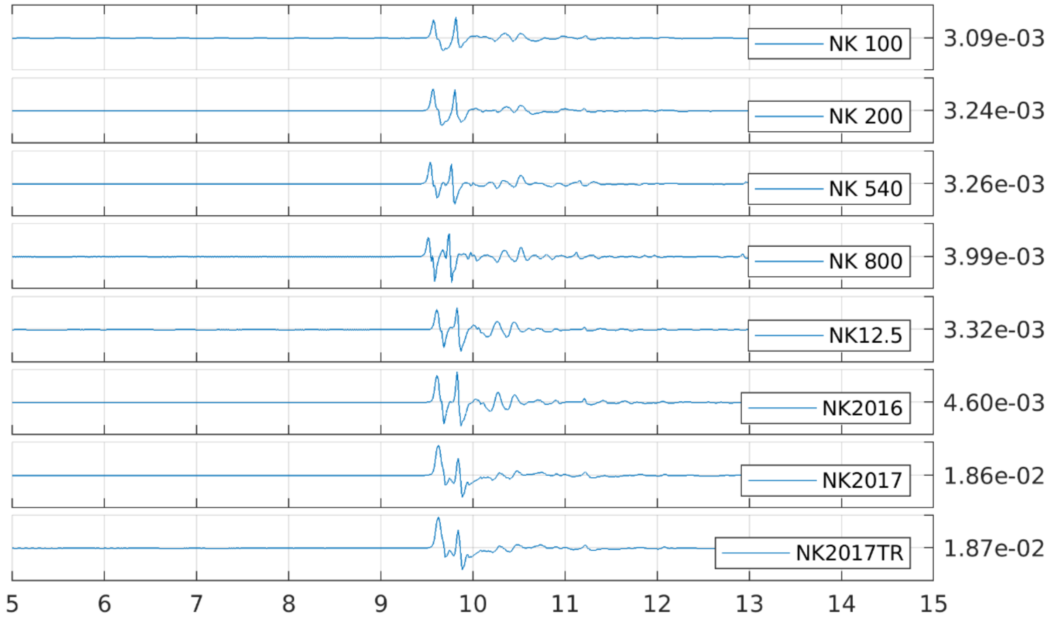
50 270
NK 100
3.09e-03
NK 200
3.24e-03
NK 540
3.26e-03
NK 800
3.99e-03
NK12.5
3.32e-03
NK2016
4.60e-03
NK2017
1.86e-02
NK2017TR
1.87e-02
5
6
7
8
9
10
11
12
13
14
15

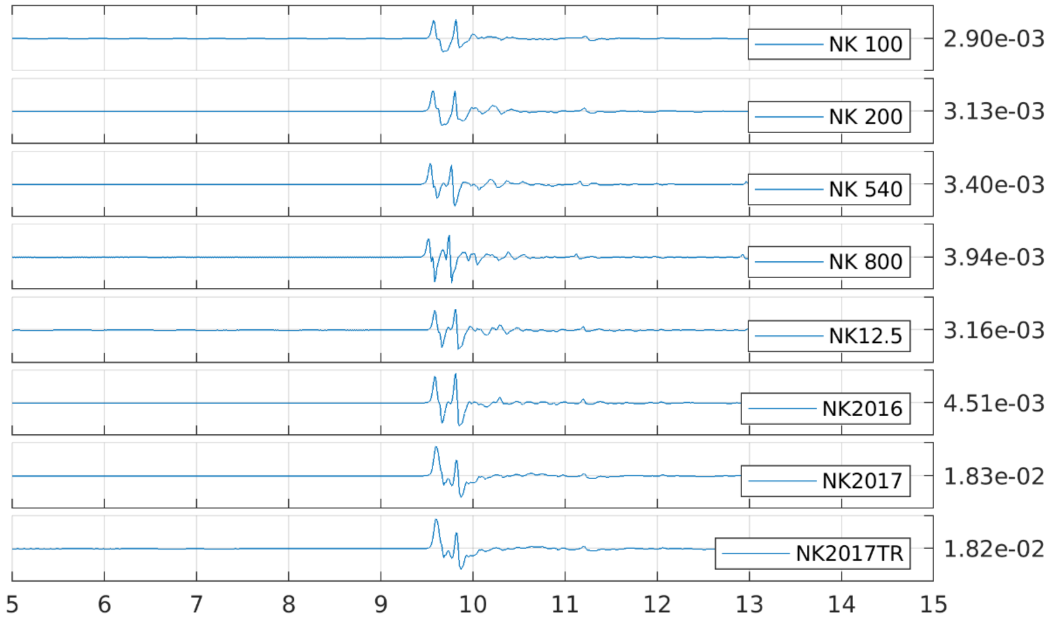
50 315
NK 100
2.90e-03
NK 200
3.13e-03
NK 540
3.40e-03
NK 800
3.94e-03
NK12.5
3.16e-03
NK2016
4.51e-03
NK2017
1.83e-02
NK2017TR
1.82e-02
5
6
7
8
9
10
11
12
13
14
15

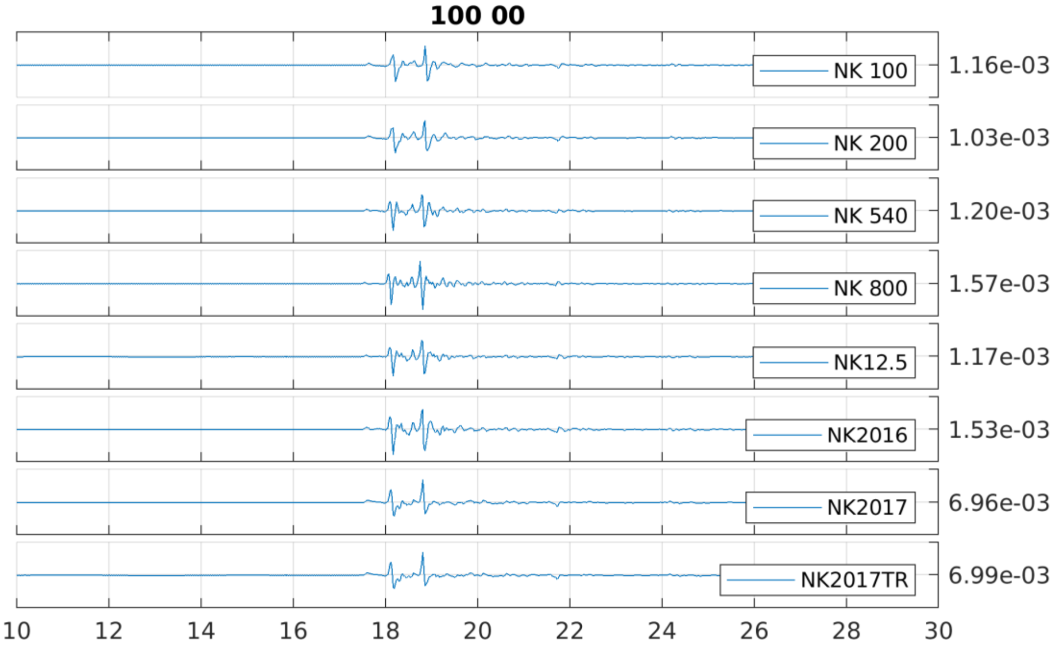
100 00
NK 100
1.16e-03
NK 200
1.03e-03
NK 540
1.20e-03
NK 800
1.57e-03
NK12.5
1.17e-03
NK2016
1.53e-03
NK2017
6.96e-03
NK2017TR
6.99e-03
10
12
14
16
18
20
22
24
26
28
30

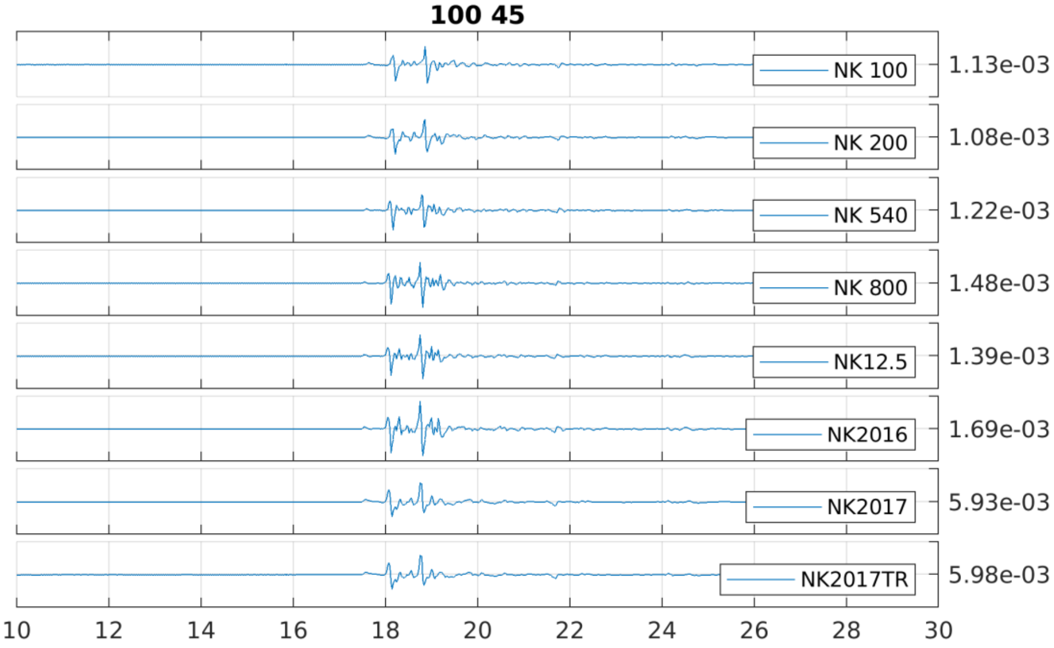
100 45
NK 100
1.13e-03
NK 200
1.08e-03
NK 540
1.22e-03
NK 800
1.48e-03
NK12.5
1.39e-03
NK2016
1.69e-03
NK2017
5.93e-03
NK2017TR
5.98e-03
10
12
14
16
18
20
22
24
26
28
30

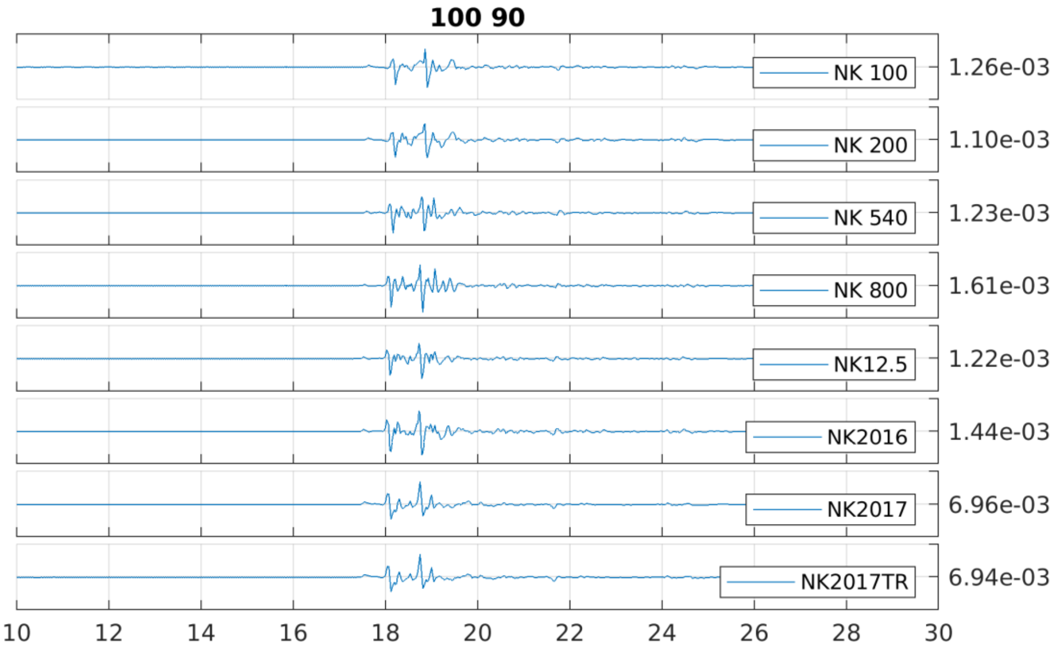
100 90
NK 100
1.26e-03
NK 200
1.10e-03
NK 540
1.23e-03
NK 800
1.61e-03
NK12.5
1.22e-03
NK2016
1.44e-03
NK2017
6.96e-03
NK2017TR
6.94e-03
10
12
14
16
18
20
22
24
26
28
30

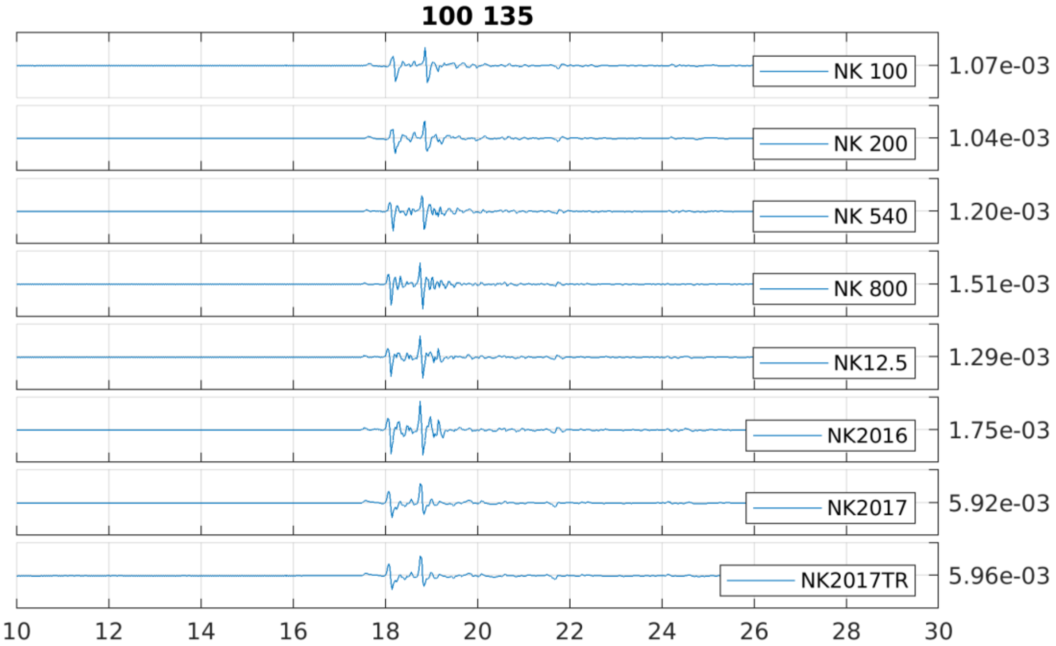
100 135
NK 100
1.07e-03
NK 200
1.04e-03
NK 540
1.20e-03
NK 800
1.51e-03
NK12.5
1.29e-03
NK2016
1.75e-03
NK2017
5.92e-03
NK2017TR
5.96e-03
10
12
14
16
18
20
22
24
26
28
30

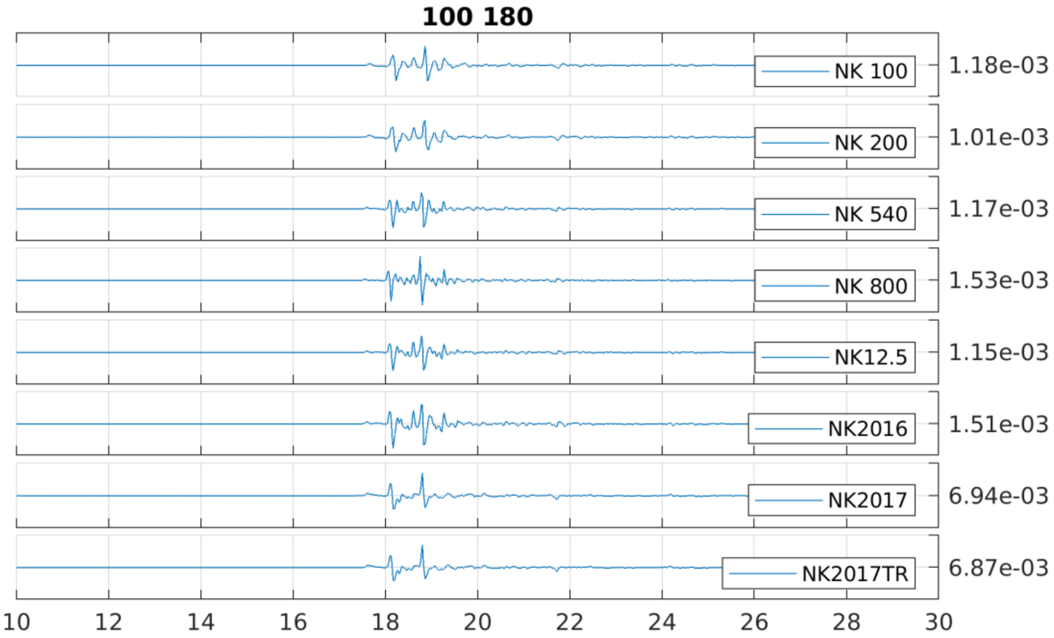
100 180
NK 100
1.18e-03
NK 200
1.01e-03
NK 540
1.17e-03
NK 800
1.53e-03
NK12.5
1.15e-03
NK2016
1.51e-03
NK2017
6.94e-03
NK2017TR
6.87e-03
10
12
14
16
18
20
22
24
26
28
30

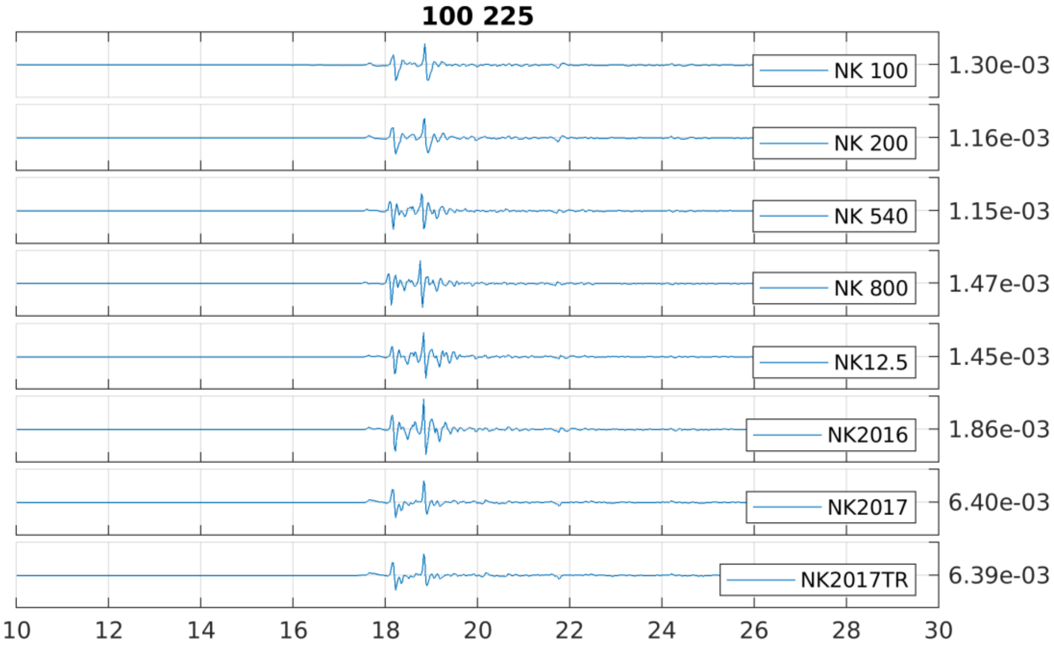
100 225
NK 100
1.30e-03
NK 200
1.16e-03
NK 540
1.15e-03
NK 800
1.47e-03
NK12.5
1.45e-03
NK2016
1.86e-03
NK2017
6.40e-03
NK2017TR
6.39e-03
10
12
14
16
18
20
22
24
26
28
30

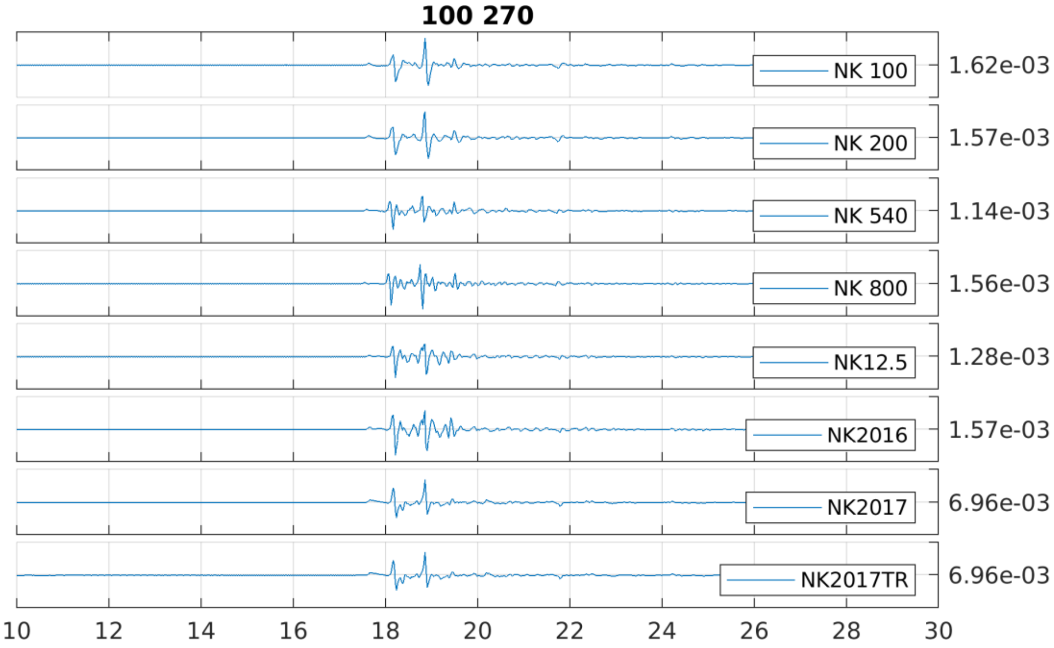
100 270
NK 100
1.62e-03
NK 200
1.57e-03
NK 540
1.14e-03
NK 800
1.56e-03
NK12.5
1.28e-03
NK2016
1.57e-03
NK2017
6.96e-03
NK2017TR
6.96e-03
10
12
14
16
18
20
22
24
26
28
30

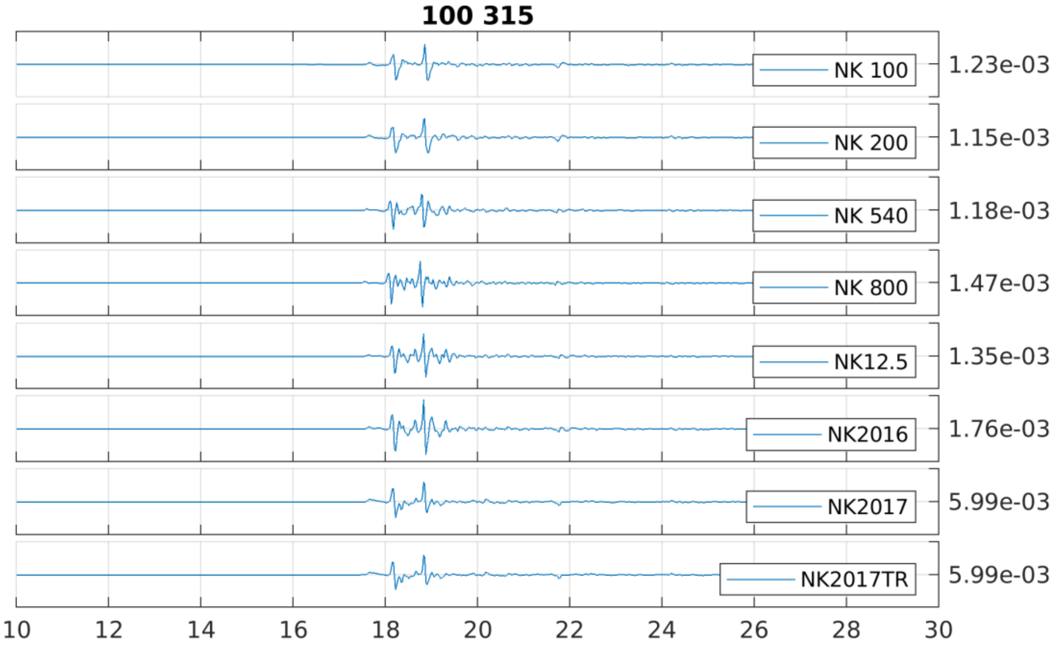
100 315
NK 100
1.23e-03
NK 200
1.15e-03
NK 540
1.18e-03
NK 800
1.47e-03
NK12.5
1.35e-03
NK2016
1.76e-03
NK2017
5.99e-03
NK2017TR
5.99e-03
10
12
14
16
18
20
22
24
26
28
30

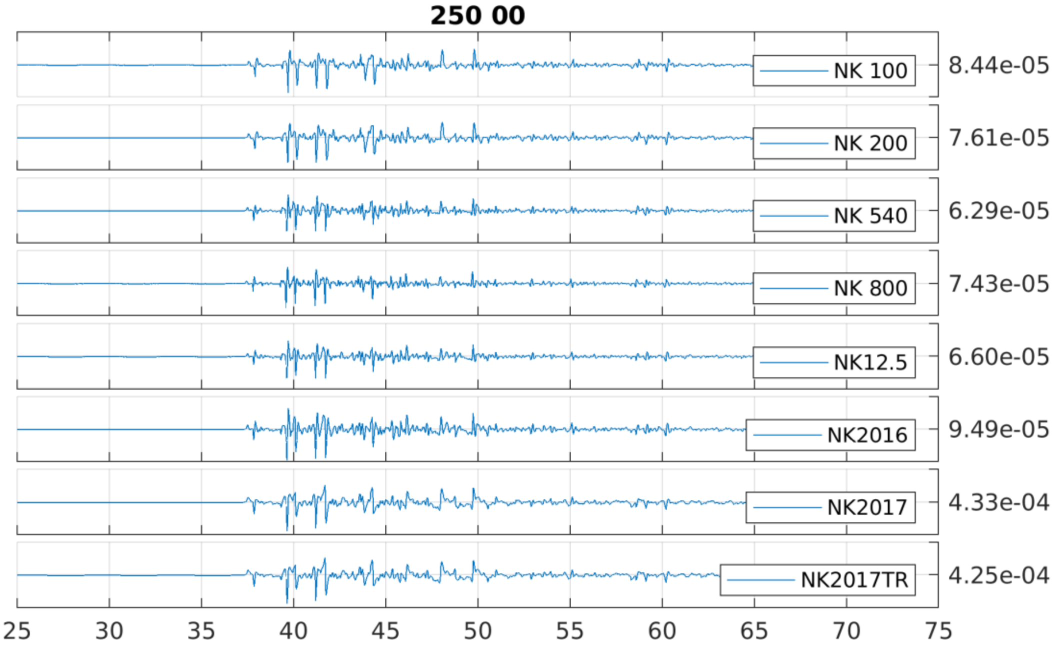
250 00
NK 100
8.44e-05
NK 200
7.61e-05
NK 540
6.29e-05
NK 800
7.43e-05
NK12.5
6.60e-05
NK2016
9.49e-05
NK2017
4.33e-04
NK2017TR
4.25e-04
25
30
35
40
45
50
55
60
65
70
75

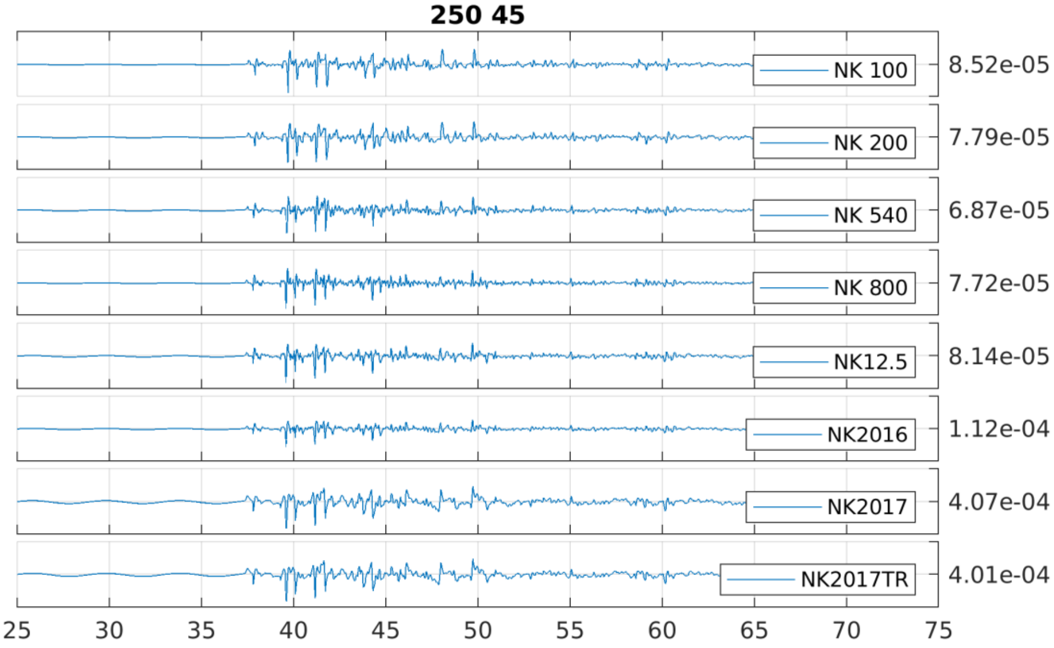
250 45
NK 100
8.52e-05
NK 200
7.79e-05
NK 540
6.87e-05
NK 800
7.72e-05
NK12.5
8.14e-05
NK2016
1.12e-04
NK2017
4.07e-04
NK2017TR
4.01e-04
25
30
35
40
45
50
55
60
65
70
75

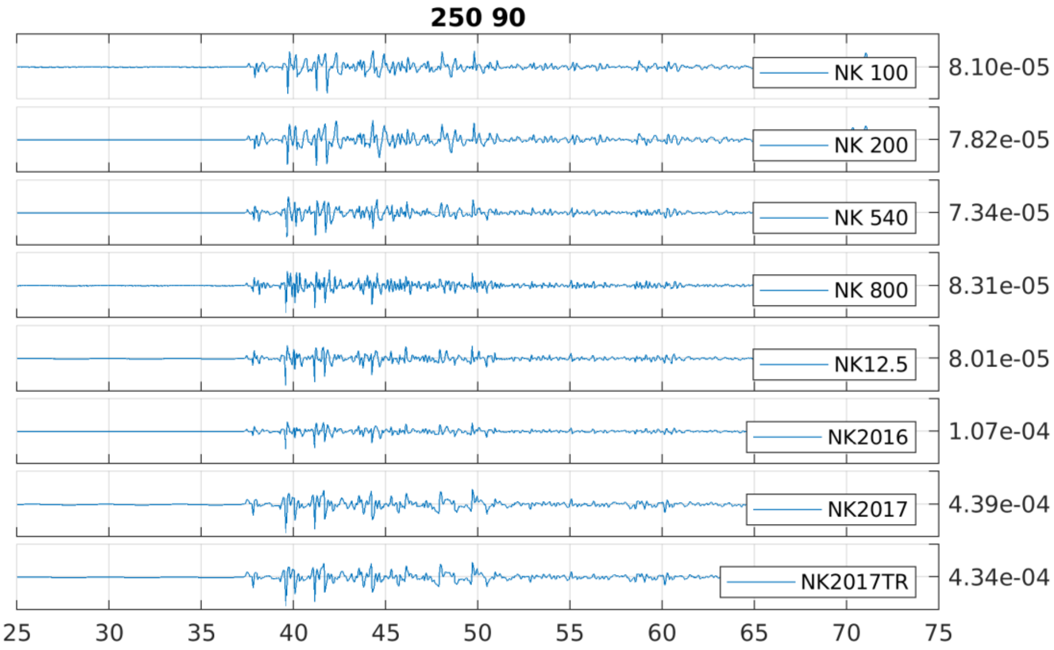
250 90
NK 100
8.10e-05
NK 200
7.82e-05
NK 540
7.34e-05
NK 800
8.31e-05
NK12.5
8.01e-05
NK2016
1.07e-04
NK2017
4.39e-04
NK2017TR
4.34e-04
25
30
35
40
45
50
55
60
65
70
75

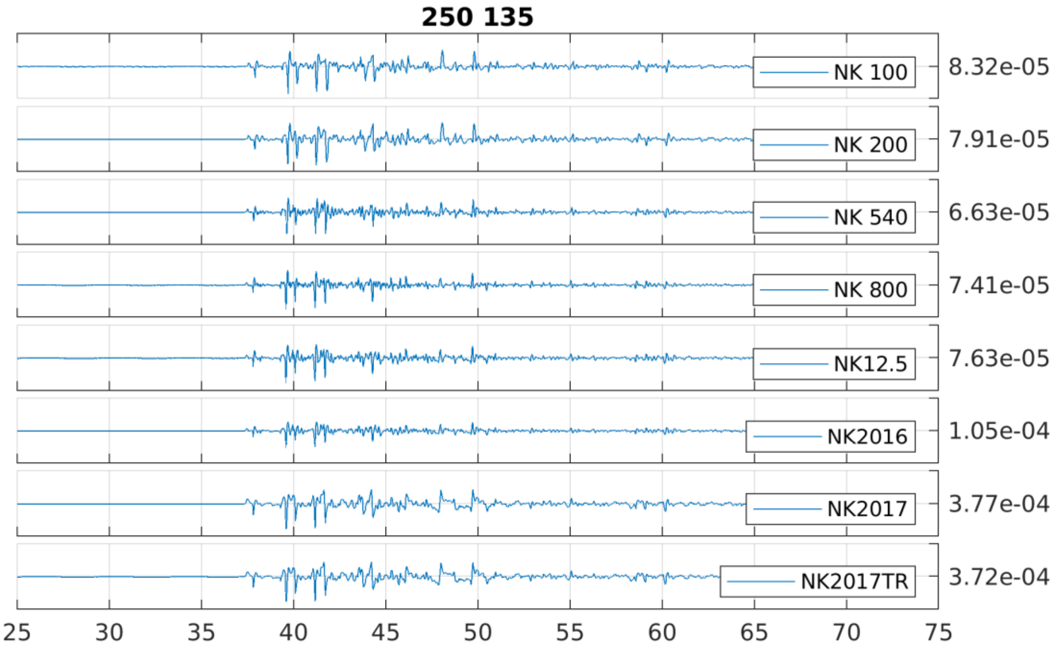
250 135
NK 100
8.32e-05
NK 200
7.91e-05
NK 540
6.63e-05
NK 800
7.41e-05
NK12.5
7.63e-05
NK2016
1.05e-04
NK2017
3.77e-04
NK2017TR
3.72e-04
25
30
35
40
45
50
55
60
65
70
75

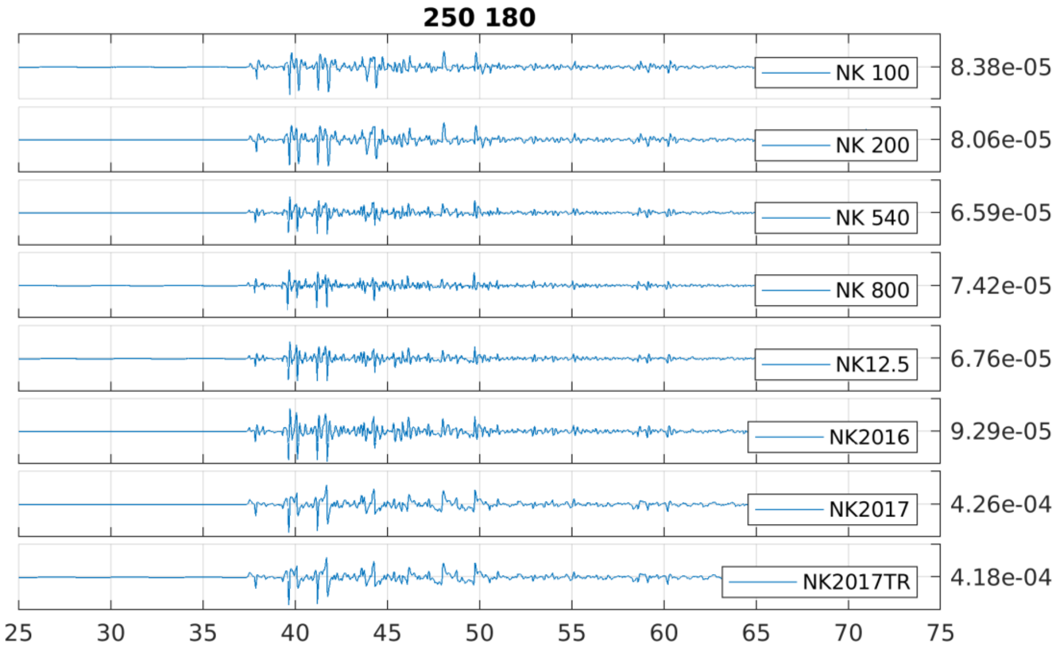
250 180
NK 100
8.38e-05
NK 200
8.06e-05
NK 540
6.59e-05
NK 800
7.42e-05
NK12.5
6.76e-05
NK2016
9.29e-05
NK2017
4.26e-04
NK2017TR
4.18e-04
25
30
35
40
45
50
55
60
65
70
75

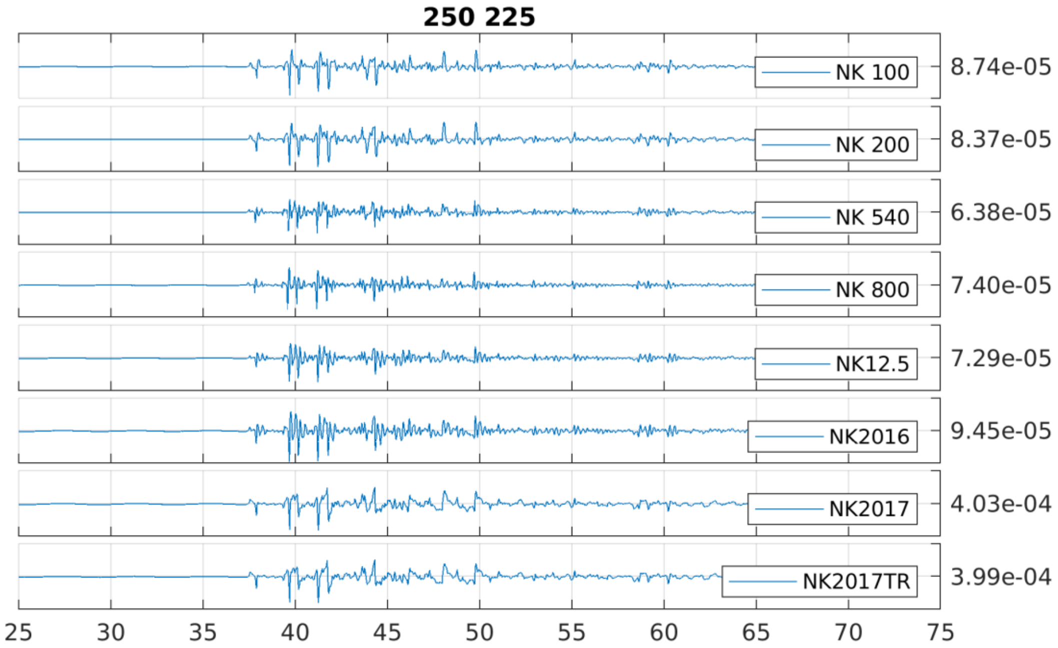
250 225
NK 100
8.74e-05
NK 200
8.37e-05
NK 540
6.38e-05
NK 800
7.40e-05
NK12.5
7.29e-05
NK2016
9.45e-05
NK2017
4.03e-04
NK2017TR
3.99e-04
25
30
35
40
45
50
55
60
65
70
75

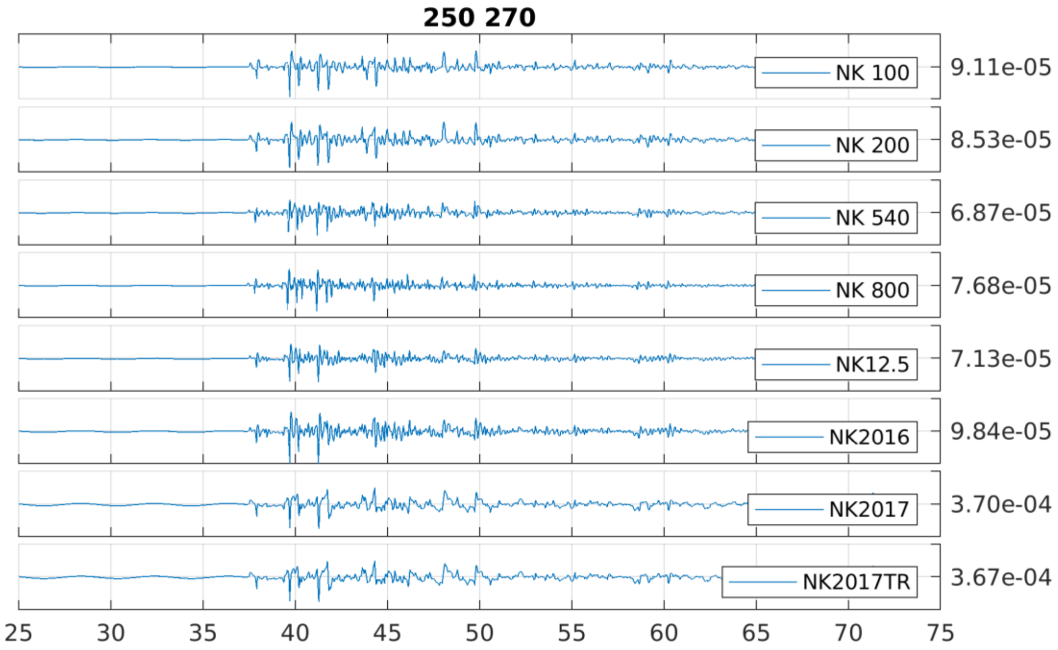
250 270
NK 100
9.11e-05
NK 200
8.53e-05
NK 540
6.87e-05
NK 800
7.68e-05
NK12.5
7.13e-05
NK2016
9.84e-05
NK2017
3.70e-04
NK2017TR
3.67e-04
25
30
35
40
45
50
55
60
65
70
75

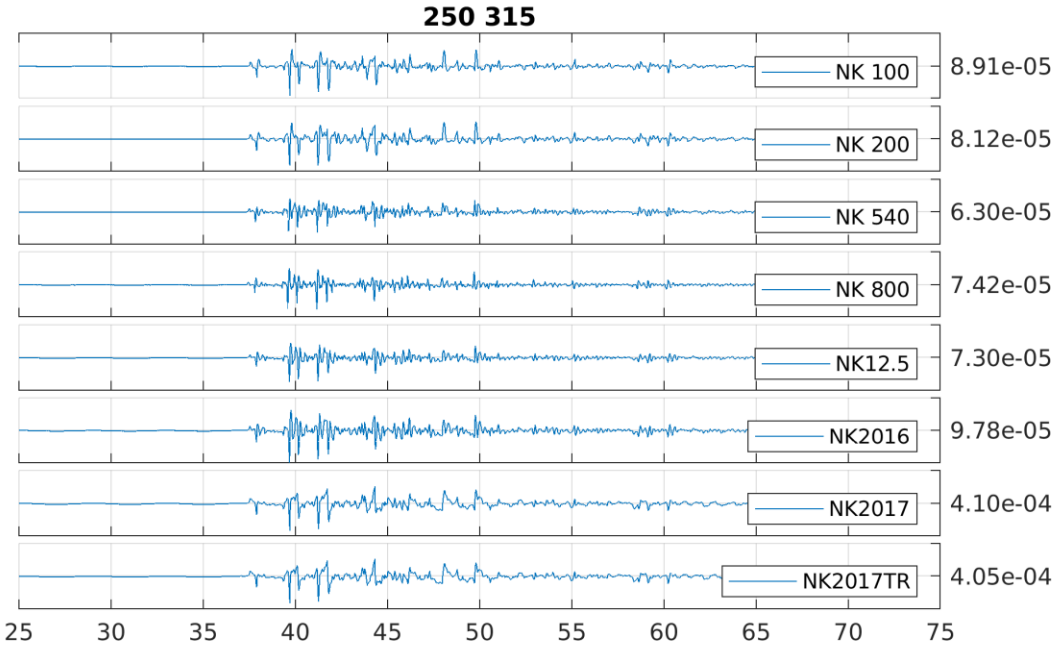
250 315
NK 100
8.91e-05
NK 200
8.12e-05
NK 540
6.30e-05
NK 800
7.42e-05
NK12.5
7.30e-05
NK2016
9.78e-05
NK2017
4.10e-04
NK2017TR
4.05e-04
25
30
35
40
45
50
55
60
65
70
75

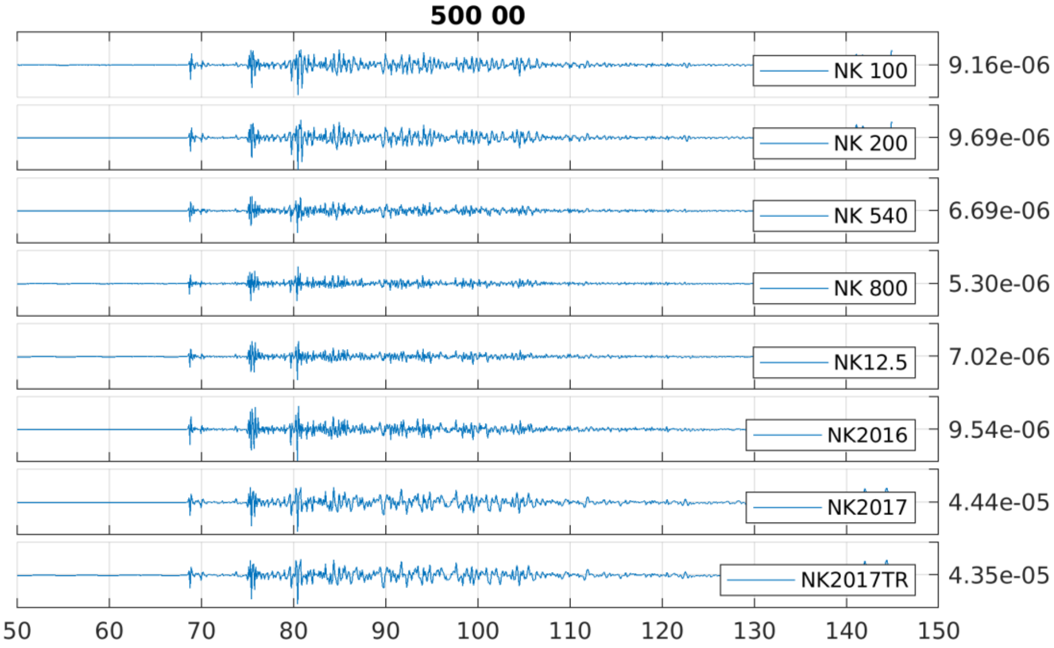
500 00
NK 100
NK 200
NK 540
NK 800
NK12.5
NK2016
NK2017
NK2017TR
9.16e-06
9.69e-06
6.69e-06
5.30e-06
7.02e-06
9.54e-06
4.44e-05
4.35e-05
50
60
70
80
90
100
110
120
130
140
150

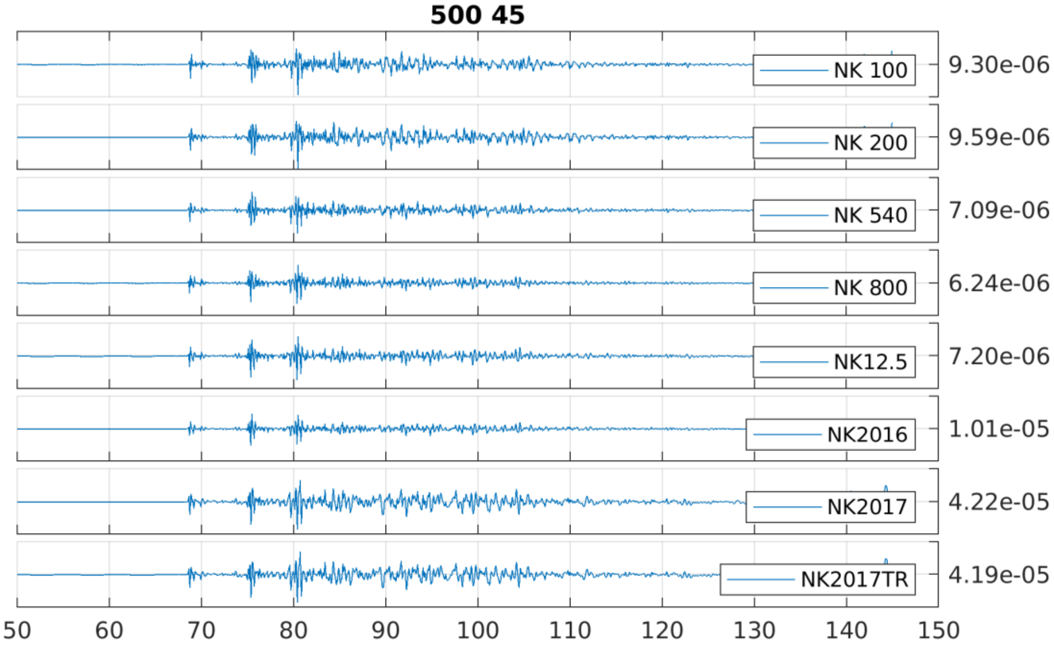
500 45
NK 100
NK 200
NK 540
NK 800
NK12.5
NK2016
NK2017
NK2017TR
9.30e-06
9.59e-06
7.09e-06
6.24e-06
7.20e-06
1.01e-05
4.22e-05
4.19e-05
50
60
70
80
90
100
110
120
130
140
150

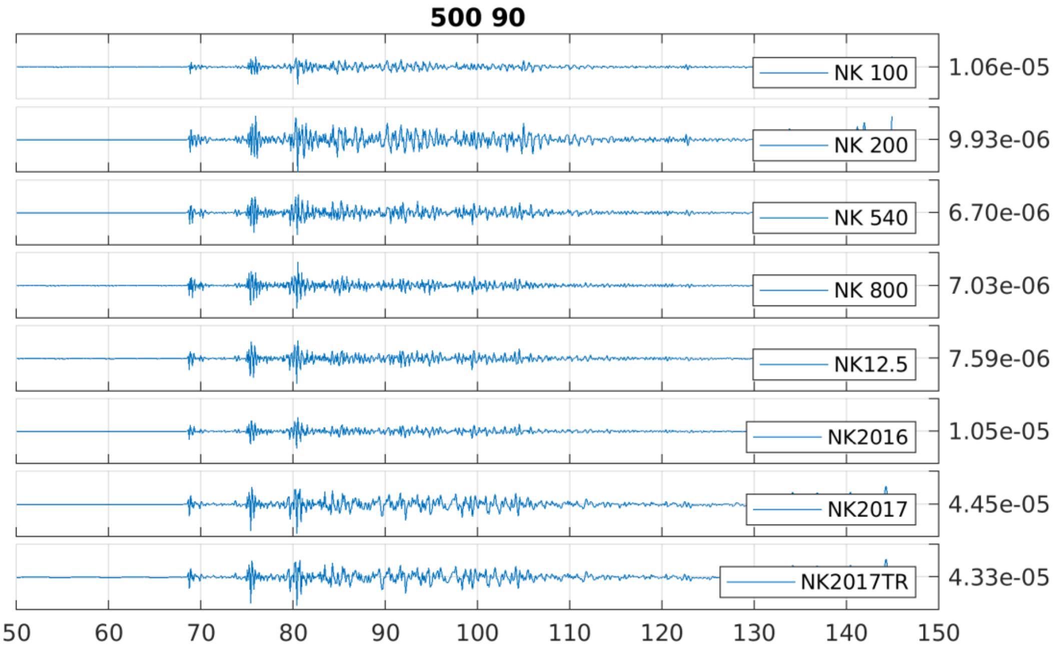
500 90
NK 100
1.06e-05
NK 200
9.93e-06
NK 540
6.70e-06
NK 800
7.03e-06
NK12.5
7.59e-06
NK2016
1.05e-05
NK2017
4.45e-05
NK2017TR
4.33e-05
50
60
70
80
90
100
110
120
130
140
150

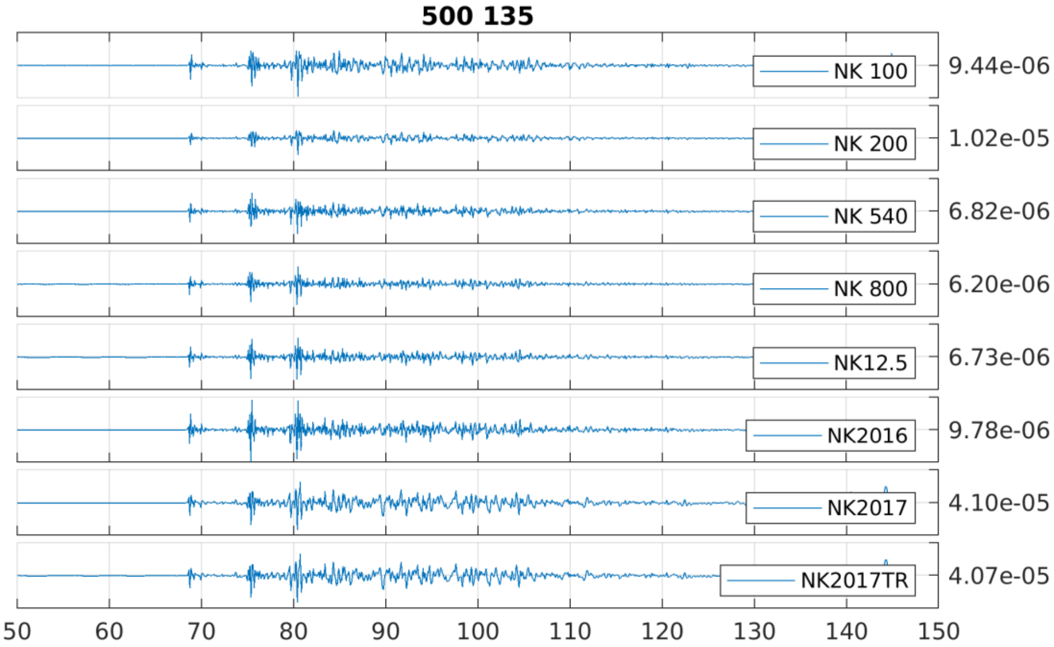
500 135
NK 100
9.44e-06
NK 200
1.02e-05
NK 540
6.82e-06
NK 800
6.20e-06
NK12.5
6.73e-06
NK2016
9.78e-06
NK2017
4.10e-05
NK2017TR
4.07e-05
50
60
70
80
90
100
110
120
130
140
150

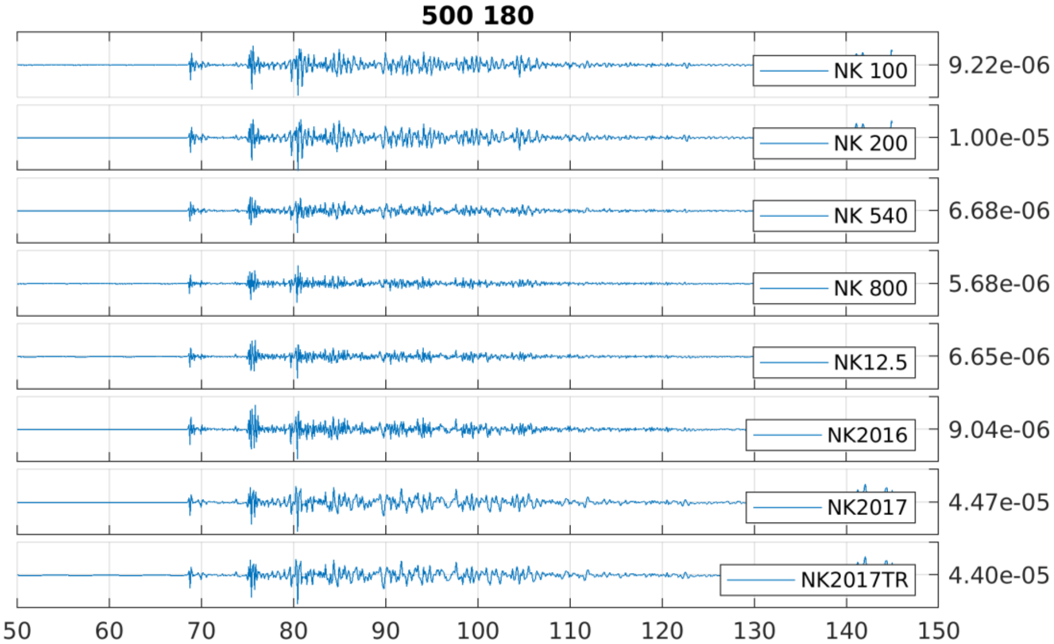
500 180
NK 100
9.22e-06
NK 200
1.00e-05
NK 540
6.68e-06
NK 800
5.68e-06
NK12.5
6.65e-06
NK2016
9.04e-06
NK2017
4.47e-05
NK2017TR
4.40e-05
50
60
70
80
90
100
110
120
130
140
150

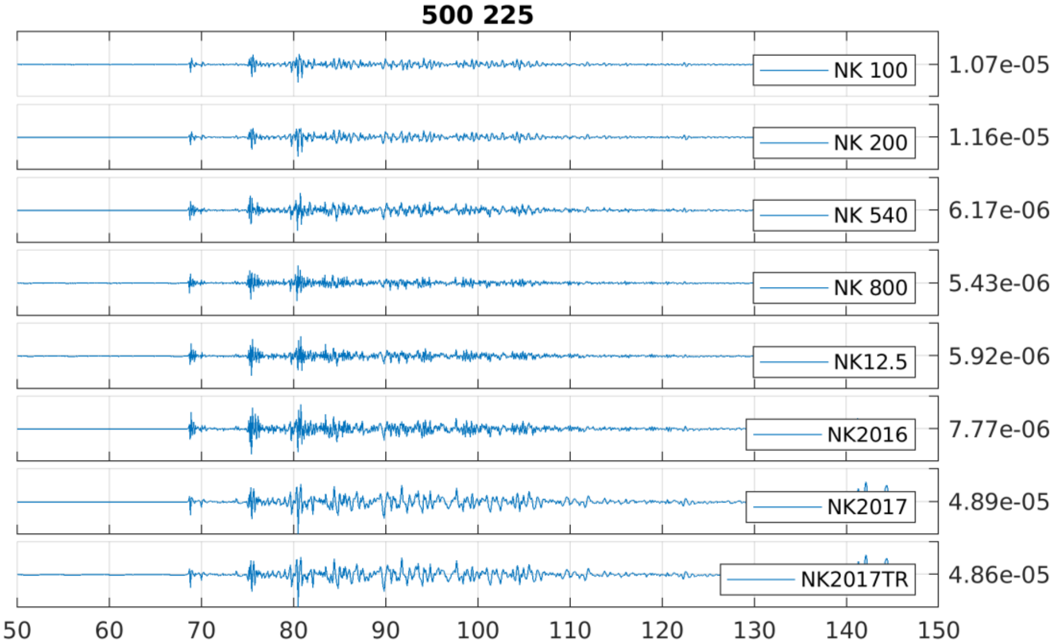
500 225
NK 100
1.07e-05
NK 200
1.16e-05
NK 540
6.17e-06
NK 800
5.43e-06
NK12.5
5.92e-06
NK2016
7.77e-06
NK2017
4.89e-05
NK2017TR
4.86e-05
50
60
70
80
90
100
110
120
130
140
150

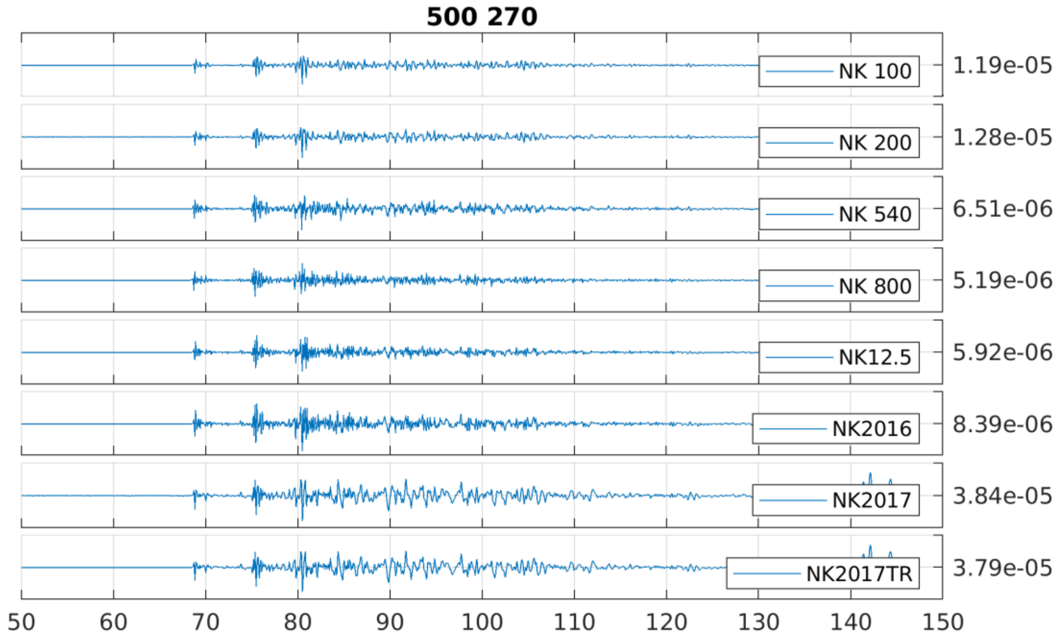
500 270
NK 100
1.19e-05
NK 200
1.28e-05
NK 540
6.51e-06
NK 800
5.19e-06
NK12.5
5.92e-06
NK2016
8.39e-06
NK2017
3.84e-05
NK2017TR
3.79e-05
50
60
70
80
90
100
110
120
130
140
150

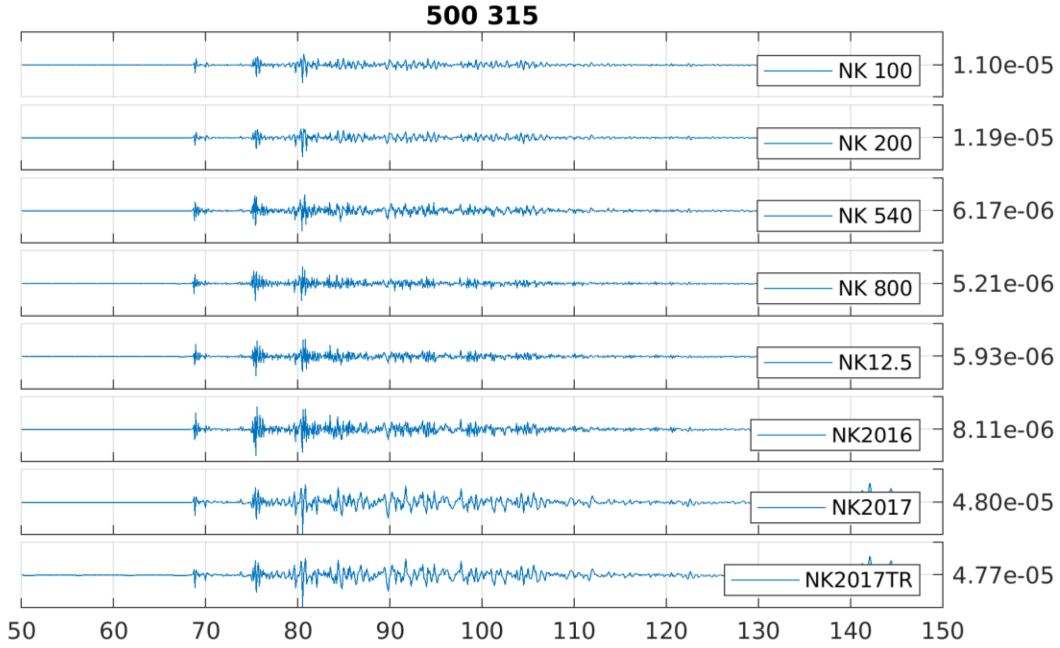
500 315
NK 100
1.10e-05
NK 200
1.19e-05
NK 540
6.17e-06
NK 800
5.21e-06
NK12.5
5.93e-06
NK2016
8.11e-06
NK2017
4.80e-05
NK2017TR
4.77e-05
50
60
70
80
90
100
110
120
130
140
150

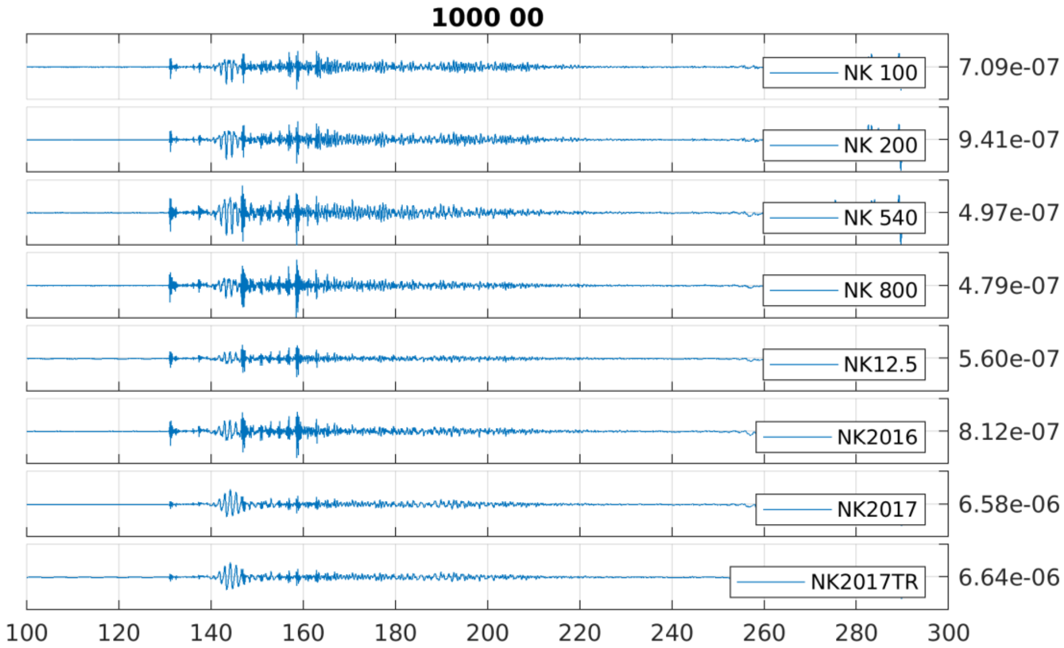
1000 00
NK 100
7.09e-07
NK 200
9.41e-07
NK 540
4.97e-07
NK 800
4.79e-07
NK12.5
5.60e-07
NK2016
8.12e-07
NK2017
6.58e-06
NK2017TR
6.64e-06
100
120
140
160
180
200
220
240
260
280
300

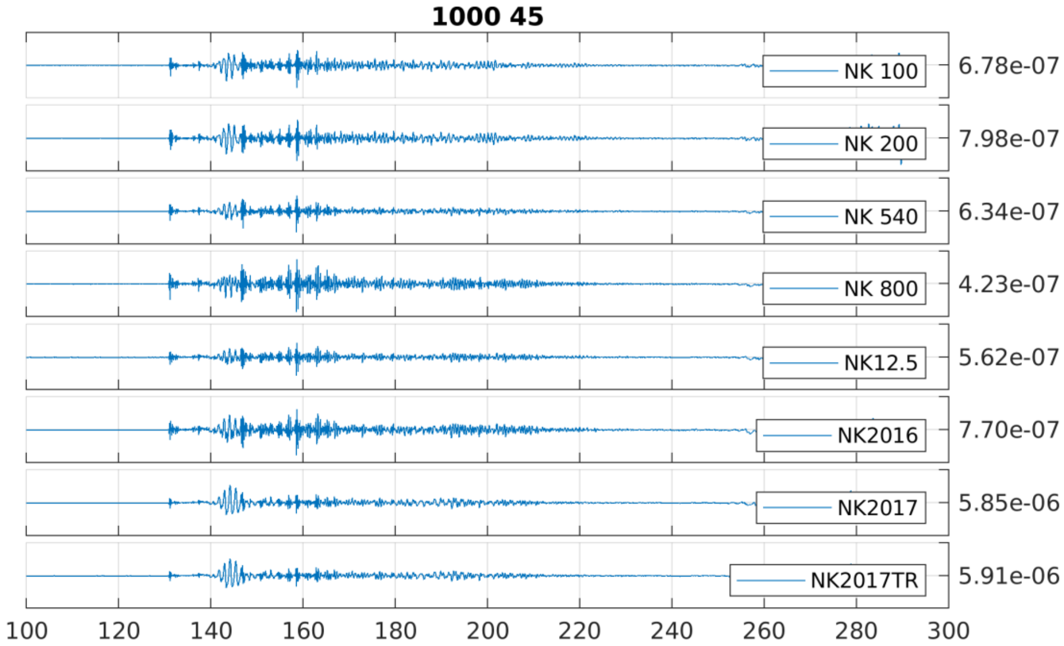
1000 45
NK 100
6.78e-07
NK 200
7.98e-07
NK 540
6.34e-07
NK 800
4.23e-07
NK12.5
5.62e-07
NK2016
7.70e-07
NK2017
5.85e-06
NK2017TR
5.91e-06
100
120
140
160
180
200
220
240
260
280
300

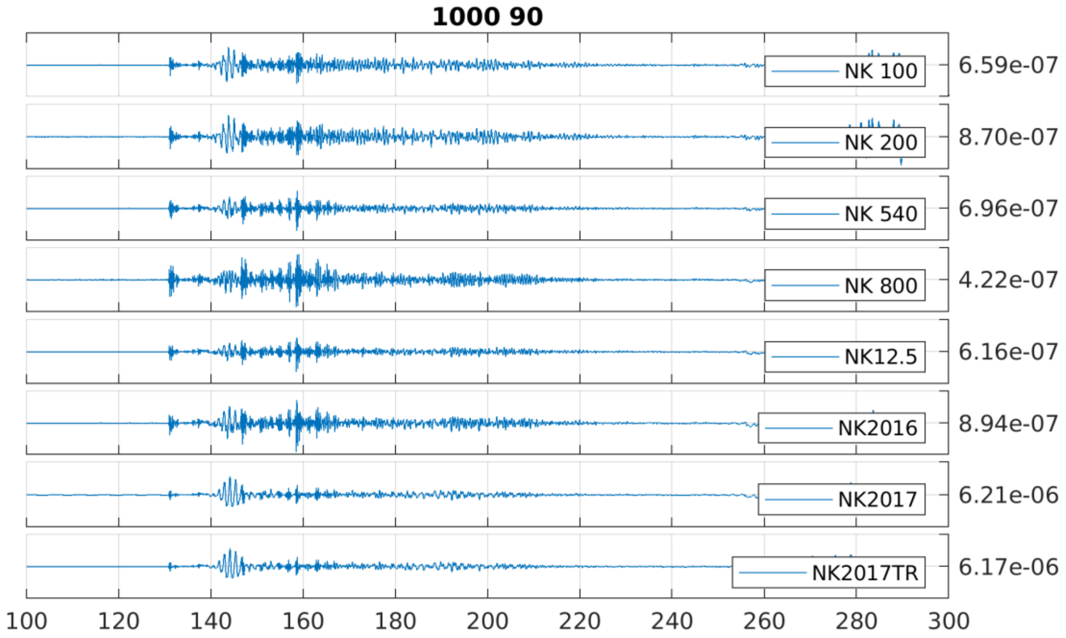
1000 90
NK 100
6.59e-07
NK 200
8.70e-07
NK 540
6.96e-07
NK 800
4.22e-07
NK12.5
6.16e-07
NK2016
8.94e-07
NK2017
6.21e-06
NK2017TR
6.17e-06
100
120
140
160
180
200
220
240
260
280
300

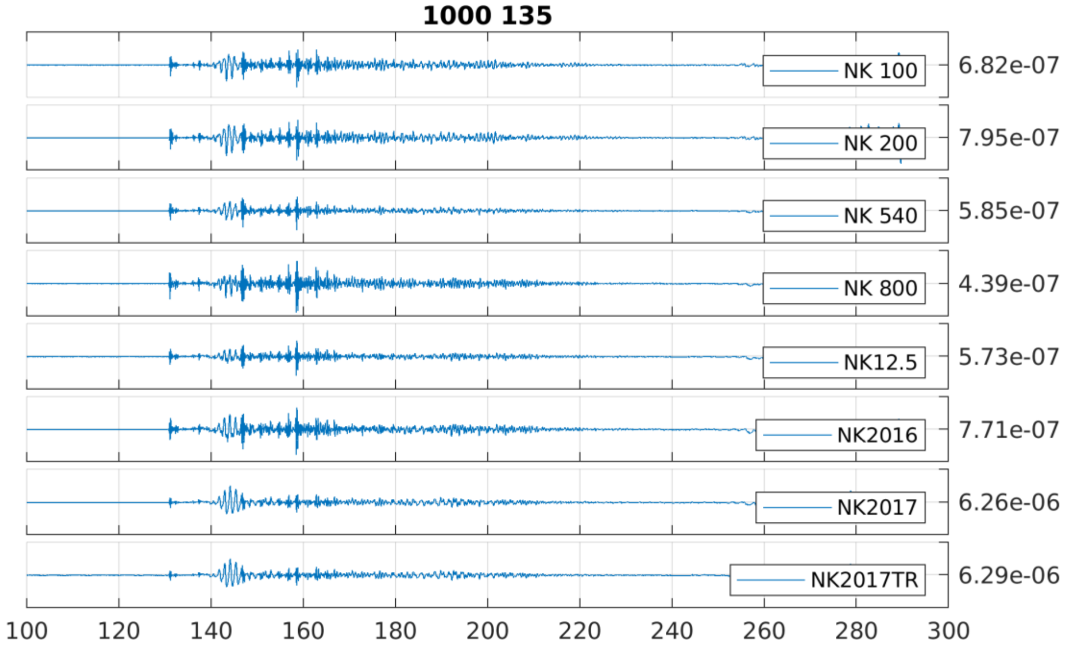
1000 135
NK 100
6.82e-07
NK 200
7.95e-07
NK 540
5.85e-07
NK 800
4.39e-07
NK12.5
5.73e-07
NK2016
7.71e-07
NK2017
6.26e-06
NK2017TR
6.29e-06
100
120
140
160
180
200
220
240
260
280
300

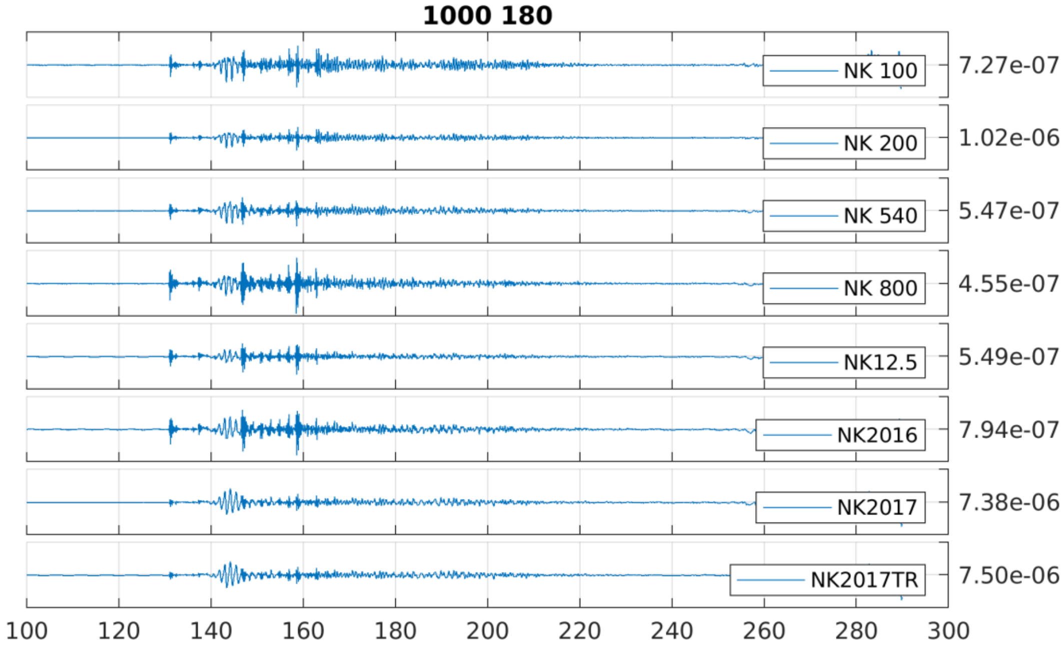
1000 180
NK 100
NK 200
NK 540
NK 800
NK12.5
NK2016
NK2017
NK2017TR
7.27e-07
1.02e-06
5.47e-07
4.55e-07
5.49e-07
7.94e-07
7.38e-06
7.50e-06
100
120
140
160
180
200
220
240
260
280
300

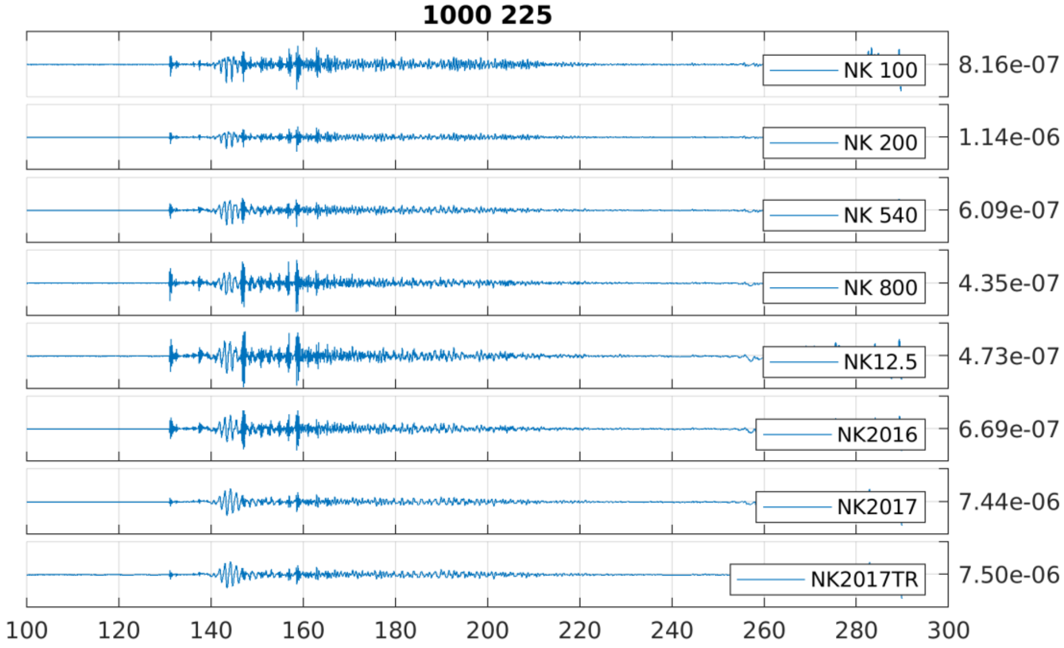
1000 225
NK 100
NK 200
NK 540
NK 800
NK12.5
NK2016
NK2017
NK2017TR
8.16e-07
1.14e-06
6.09e-07
4.35e-07
4.73e-07
6.69e-07
7.44e-06
7.50e-06
100
120
140
160
180
200
220
240
260
280
300

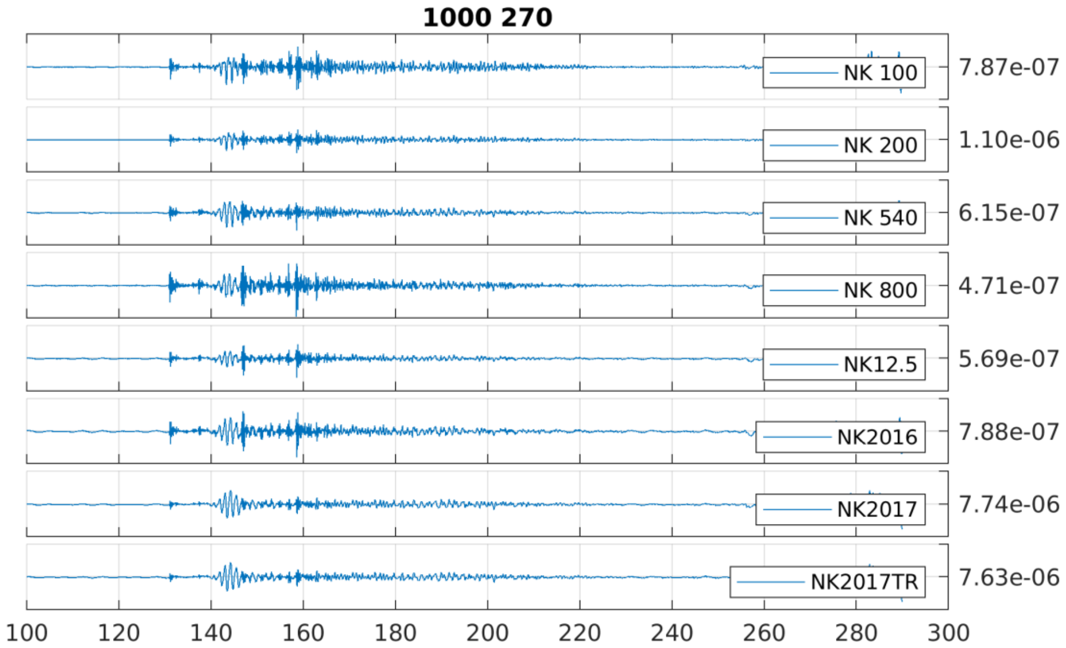

1000 270
NK 100
7.87e-07
NK 200
1.10e-06
NK 540
6.15e-07
NK 800
4.71e-07
NK12.5
5.69e-07
NK2016
7.88e-07
NK2017
7.74e-06
NK2017TR
7.63e-06
100
120
140
160
180
200
220
240
260
280
300

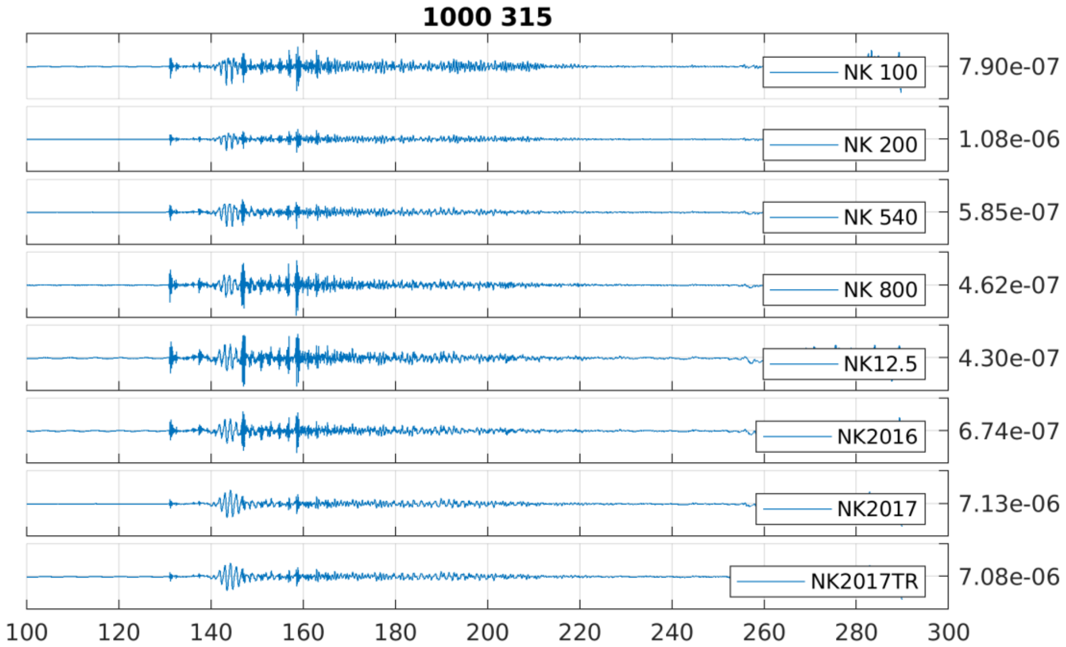

1000 315
NK 100
7.90e-07
NK 200
1.08e-06
NK 540
5.85e-07
NK 800
4.62e-07
NK12.5
4.30e-07
NK2016
6.74e-07
NK2017
7.13e-06
NK2017TR
7.08e-06
100
120
140
160
180
200
220
240
260
280
300

List of Symbols, Abbreviations, and Acronyms

AFRL	Air Force Research Laboratory
DOS	Department of State
DPRK	Democratic People's Republic of Korea
GSN	Global Seismographic Network
TOA	Take-off Angle